Universität Stuttgart
Geodätisches Institut

Analysis of Earthquake Signals by Spaceborne Gravimetry

Masterarbeit im Studiengang
GEOENGINE
an der Universität Stuttgart

Zhou CAO
aus Wuhan

Stuttgart, December 2011

Betreuer: Prof. Dr.-Ing. Nico Sneeuw
Universität Stuttgart

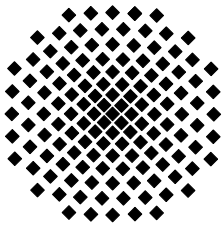

Universität Stuttgart

master thesis

Zhou CAO

Analysis of Earthquake Signals by Spaceborne Gravimetry

Tutor: Prof. Dr.-Ing. Nico Sneeuw
Examiner: Prof. Dr.-Ing. Nico Sneeuw

Mourn the victims of the earthquakes all over the world.

R. I. P.

Erklärung der Urheberschaft

Ich erkläre hiermit an Eides statt, dass ich die vorliegende Arbe ohne Hilfe Dritter und ohne Benutzung anderer als der angegebenen Hilfsmittel angefertigt habe; die aus fremden Quellen direkt oder indirekt übernommenen Gedanken sind als solche kenntlich gemacht. Die Arbeit wurde bisher in gleicher oder ähnlicher Form in keiner anderen Prüfungsbehörde vorgelegt und auch noch nicht veröffentlicht.

Ort, Datum Unterschrift

Zhou CAO

Acknowledgment

First I want to express my gratitude to Prof. Nico Sneeuw for offering this topic for my master's thesis and his patience in guiding me! With his continuous encouragement, I can set up my confidence again. Thanks to Mr. Balaji Devaraju for his help on my data! Dr. Matthias Weigelt helped me a lot and offered me his program. Without Mr. Matthias Roth's LaTeX template and help I was not able to write my thesis in LaTeX. I want to express my special thanks to Mr. Anjelous Mawa Lagu who helped me improve my English writing of the thesis and Prof. Erik W. Grafarend who helped me in the final correction of the Abstract.

Thanks to Dr. Andreas Hoechner from GFZ, Dr. Isabelle Panet from IGN, Dr. Fred Pollitz from USGS, Dr. Jianli Chen from CSR and Dr. Wenke Sun and Dr. Wuxing Wang from Chinese Academic of Science for answering my questions! Thanks to the "Goddard Earth Sciences Data and Information Services Center" (http://grace.jpl.nasa.gov) for the GLDAS model and C_{20} data from SLR and CSR for GRACE data!

While writing the thesis, I've been in my hometown — Wuhan for one month. Being with my family and relatives was great for me after two years abroad. My sister and our dog Pipi always accompanied me while I was at home. I love them!

My mother, the greatest mother ever who is still working for me, I cannot thank her enough.

Life is not so easy especially when you are living without your family around. But friends instead play a very important role in life. My friends from the Diploma program Geodäsie und Geoinformatik and Master programs GEOENGINE and MIP gave me great release whenever I played games with them. Thanks for the invention of the card game — Sanguosha. I want to convey my thanks to some of the doctor students in Stuttgart University as well. Furthermore, my sincere thanks to Scalabrinian Secular Missionary for their wonderful programs for the young people. Thanks to Rösler's family from Flintbek for keeping correspondence with me until now and Mr. and Mrs. Rotter's help in Stuttgart.

Last but not least, thank you to all the people who had helped and encouraged me, Prof. Yibin Yao from School of Geodesy and Geomatics of Wuhan University, Mrs. Duan Chen in the International office of Wuhan University and Dr. Jianqing Cai in Geodätisches Institut of Stuttgart University.

Life just begins and to my new beginning somewhere on the earth!

Thanks to life itself!

Abstract

The Gravity Recovery And Climate Experiment (GRACE) mission was launched on Mar. 17, 2002 and has provided the scientists with the gravity data for nearly ten years. The time variable gravity field provided by the GRACE has improved our knowledge of the earth in many fields such as hydrology, oceanography and glaciology.

But compared to those "hot" fields, the publications of GRACE in seismology is considerably less. However, GRACE can provide scientists with an independent observation of the earthquake process. Coincidentally, some of the largest earthquakes are within GRACE's life span — Sumatra-Andaman Earthquake (Indonesia) 2004, Maule Earthquake (Chile) 2010 and Tōhoku Earthquake (Japan) 2011. Furthermore, a smaller earthquake — Sichuan Earthquake (China) 2008 has also been examined to test whether the GRACE can detect earthquakes smaller than $M_w = 8.0$. Different from the traditional methods of the earthquake researches, the gravity method has its advantages: 1. Massive: global scale; 2. Insight: gravity changes can reveal the underground mass changes which do not cause so much motion on the earth surface; 3. Convenient: superior to the traditional methods, the spaceborne gravimetry can get the data from the ocean and glacier parts.

The conditions of the data are different among these four earthquakes. The procedures to eliminate the GRACE observation errors and unwanted geophysical data are necessary. First, the C_{20} term should be replaced by the Satellite Laser Ranging (SLR) data. Second, the hydrology signal especially in the regions of Chile and Sichuan should be eliminated by the Global Land Data Assimilation System (GLDAS) model. Third, Fan filter or Gauss filter 350 km should be applied.

Time series analysis by the two-phase changepoint detection and hypothesis testing are applied for each earthquake which is a point-wise analysis. Least squares adjustment is performed on each point to display the coseismic and postseismic signals. Meanwhile, the surface analysis is done by the Empirical Orthogonal Functions (EOF) as it has a flexible base which can suit the data automatically.

Although the observation errors have been removed as much as possible, the limited spatial and time resolutions of the GRACE satellite and to retrieve relatively weak earthquake signal among the strong hydrological signals are still problems in the analysis.

GRACE can detect some of the large earthquakes, but it depends on the earthquake type, area and the length of the time-series before and after the earthquake. Both coseismic signal and postseismic signal are detected in Sumatra-Andaman Earthquake. Meanwhile, there is no significant coseismic signal in the time series of Sichuan Earthquake, but the EOF detects suspicious earthquake signal in mode 2 with the magnitude less than 1 μGal. For Maule Earthquake, only the coseismic signal is detected. Due to the limited dataset, the detection of the coseismic signal is successful but the postseismic signal is not long enough to be detected in Tōhoku Earthquake. However, the different filters will affect the magnitude of the gravity change, so

the real gravity changes of those four areas are still under debate. Last, EOF can be used for the separation of the earthquake signals.

Compared to other geodetic technics the gravity method can detect the signals underground and in the ocean areas. The coseismic and postseismic signals detected by GRACE show underground processes of the earthquakes which can help scientists better understand the earthquake mechanism and will contribute to the earthquake prediction in the future.

Key Words : GRACE, Earthquake, Gravity, EOF, Geodesy, Seismology.

Contents

List of Figures

List of Tables

List of Abbreviations

ACC	Accelerometer 9
CHAMP	CHAllenging Mini-Satellite Payload for Geosciences and Application 2, 5–7, 11
CNES	Centre National d'Etudes Spatiales (National Center for Space Studies, France) 11–13, 90
CSR	Center for Space Research (University of Texas at Austin) IX, XLVIII, 7, 11–13, 24, 25, 32, 47, 52, 90
CWT	Continuous Wavelet Transform 13
DEOS	Delft Institute of Earth Observation and Space System (Delft University of Technology) 11, 90
DLR	Deutsches Zentrum für Luft- und Raumfahrt e.V. (German Aerospace Center) 7
EOF	Empirical Orthogonal Functions XI, XII, XXXVII, XLVIII, 3, 12, 13, 33, 45, 57, 65, 66, 76, 85, 86, 89–91
ESA	European Space Agency 6
EWH	Equivalent Water Height XIII, XLVIII, 20, 22
GFZ	Deutsches GeoForschungsZentrum (German Research Centre for Geosciences) IX, 5, 7, 8, 11, 24, 25, 90
GLDAS	Global Land Data Assimilation System IX, XI, XV–XVIII, XLV, XLVIII, 18, 33–35, 47–50, 60, 61, 63–66, 68, 70, 72, 74–79, 81, 83, 89
GOCE	Gravity Field and Steady-State Ocean Circulation Explorer 2, 5, 6
GPS	Global Positioning System 5, 8, 9, 11–13, 24, 72, 91
GRACE	Gravity Recovery And Climate Experiment IX, XI, XII, XV–XVIII, XLI, XLIII–XLVI, XLVIII, 2, 3, 5–13, 18, 23–27, 32, 34, 35, 38, 43, 47–56, 58, 60–70, 72–81, 83–87, 89–91
GRGS	Le Groupe de Recherche de Géodésie Spatiale (Space Geodesy Research Group, France) 13
GSFC	Goddard Space Flight Center 11, 24, 25, 33, 90
GSHA	Global Spherical Harmonic Analysis 15, 16
GSHC	Global Spherical Harmonic Computation 15
GSHS	Global Spherical Harmonic Synthesis 15, 16
HL-SST	High to Low Satellite-to-Satellite Tracking 5

IAG International Association of Geodesy 1
IGN Institut Géographique National (National Geographic Institute, France) IX
InSAR Interferometric Synthetic Aperture Radar 91
IPU Instrument Processing Unit 9
ITG Institut für Theoretische Geodäsie (Universität Bonn) 11, 90

JPL Jet Propulsion Laboratory, U.S XLVIII, 7, 11, 33, 47

KBR K-Band Ranging system 8, 9, 11

LAGEOS Laser GEOdynamics Satellite 11
LL-SST Low to Low Satellite-to-Satellite Tracking 5
LSM Land Surface Model 33

NASA National Aeronautics and Space Administration, U.S 7, 33
NCEP National Centers for Environmental Prediction, U.S 33
NOAA National Oceanic and Atmospheric Administration, U.S 33

PC Principle Components XLVIII, 45, 57, 65, 66, 76, 85, 89, 90
PCA Principal Component Analysis 45
POD Precision Orbit Determination 9
PREM Preliminary Reference Earth Model 21

RF Radio Frequency 9
RMS Root Mean Square XXIII, 24

SCA Star Camera Assembly 9
SLR Satellite Laser Ranging IX, XI, XV, XLVIII, 5, 11, 24–26, 48
SNR Signal-to-Noise Ratio XL, 27, 32
SPU Signal Processing Unit 8, 9
SSL Space Systems/Loral 7
SST Satellite-to-Satellite Tracking 5, 8
SVD Singular Value Decomposition XXXVII, XXXVIII, 45

USGS United States Geological Survey IX, 2, 49, 56, 59, 71, 82
USO Ultra-Stable Oscillator 8

List of Symbols

α	Damping factor of a filter
β	Multiplier to the Stokes coefficient of a filter
χ^2	χ^2 distribution
Δ	Laplace operator
γ	Normal gravity (scalar) (unit: $\mathrm{m/s^2}$ or Gal)
$\boldsymbol{\gamma}$	Normal gravity (vector) (unit: $\mathrm{m/s^2}$ or Gal)
Γ	Eigenfunction
λ, ξ	Longitude in spherical coordinate (unit: degree ($^\circ$))
μ	Linear dashpot constant (unit: $\mathrm{N \cdot s/m}$)
∇	Gradient operator
Φ	Integrated area (unit: $\mathrm{m^2}$)
ρ	Density (unit: $\mathrm{kg/m^3}$)
τ	Maxwell viscoelastic relaxation time (unit: s)
Ω	Rotation rate of the earth (unit: degree ($^\circ$/s))
θ, ϕ	Co-latitude in spherical coordinate (unit: degree ($^\circ$))
σ	Root Mean Square (RMS)
Λ_l	Eigenvalue depending on degree l
δ_{lm}	Kronecker delta function
a	Average cap of Gauss filter (unit: m)
Δg	Gravity anomaly (scalar) (unit: $\mathrm{m/s^2}$ or Gal)
$\mathbf{\Delta g}$	Gravity anomaly (vector) (unit: $\mathrm{m/s^2}$ or Gal)
E	Energy (unit: J)
$\mathbf{E}$	Expectation
$\mathcal{F}$	F distribution
$G(\bullet)$	Normalized weighting function of a filter
g	Corresponding function in spectrum domain of the normalized weighting function of a filter
$\mathbf{g}$	Gravity (vector) (unit: $\mathrm{m/s^2}$ or Gal)
k	Linear spring constant (unit: N/m)
L	Maximum degree
l	Degree of the spherical harmonics
m	Order of the spherical harmonics
N	Geoid height (unit: m)
R	Radius of the earth (unit: m)
r	Radius in spherical coordinate (unit: m)
T	Anomalous potential (unit: J)
U	Normal gravity potential (unit: J)
V	Gravity potential (unit: J)
W	Gravity potential on the geoid (unit: J)

GM	Constant of the earth (unit: m^3/s^2)
k_l	Love number of degree
M_w	The moment magnitude scale measuring the size of earthquakes in terms of the energy released
$c_{X,Y}$	Correlation of X and Y
C_{lm}	Non-normalized Stokes coefficient (cos) of degree l and order m
$\tilde{C}_{lm}$	Normalized Stokes coefficient (cos) of degree l and order m
P_{lm}	Non-normalized Legendre polynomials of degree l and order m
$\tilde{P}_{lm}$	Normalized Legendre polynomials of degree l and order m
S_{lm}	Non-normalized Stokes coefficient (sin) of degree l and order m
$\tilde{S}_{lm}$	Normalized Stokes coefficient (sin) of degree l and order m
Y_{lm}	Non-normalized surface spherical harmonic function of degree l and order m
$\tilde{Y}_{lm}$	Normalized surface spherical harmonic function of degree l and order m
$F(\bullet), H(\bullet)$	Function in spatial domain.
f, h	Corresponding function in spectrum domain

Chapter 1

Introduction

1.1 Geodesy, Physical Geodesy and Seismology

Geodesy (from Greek "$\gamma\varepsilon\omega\delta\alpha\iota\sigma\acute{\iota}\alpha$" - geodaisia means "division of the Earth") is the science of studying the shape, size and gravity field of the Earth.[1] It is one of the branches of the earth sciences. The geodesists set up global and national control networks by using space and terrestrial techniques in order to study some of the geodynamical topics such as crustal motion, tides, and polar motion, which need fixed geo-datums and the corresponding coordinate system (Helmert, 1880). In German speaking world geodesy is divided into two subdisciplines: "Erdmessung" or "höhere Geodäsie" which means the "Higher Geodesy" and focuses on the earth measurement in the global scale and the "Ingenieurgeodäsie" which means "Practical Geodesy" or "Engineering Geodesy" and emphasizes on the specific regions of the earth and includes surveying.

Physical geodesy belongs to the "Erdmessung" or "höhere Geodäsie" and concerns with determining the physical shape of the earth while geodesy studies the geometrical shape as well (Sneeuw, 2006). The physical shape of the earth is the *geoid* defined as one of the equipotential surface of the earth's gravity field.

Seismology in a broad sense is the branch of science concerned with earthquakes and related phenomena.[2] The main method most seismologists are using is the body waves and the surface waves.

With extremely fast development of the space techniques and the satellite geodesy methods, the satellites provide us with very valuable data on global scale. In recent decades the earth related researches are using more and more data from the gravity satellites or altimetry satellites which are traditionally considered to be served for the geodetic science, such as oceanography, hydrology and glaciology. Some of the excellent works proved the combination of seismology and physical geodesy is helpful to detect some of the earth inner processes.

1.2 Purpose of the Research

Earthquake is one of the most devastating disasters that human beings have to face.

[1] International Association of Geodesy (IAG), 2011: http://www.iag-aig.org/index.php?tpl=intro&id_c=72&id_t=357
[2] Oxford Dictionary, 2011: http://oxforddictionaries.com/definition/seismology?q=seismology

Table 1.1: *Significant Earthquakes Damages in the Recent Years*[a]

Date	Location	Fatalities	Magnitude [b]
Jan. 26, 2001	Gujarat, India	20,085	7.6
Dec. 26, 2003	Southeastern Iran	31,000	6.6
Dec. 26, 2004	Off west coast northern Sumatra,Indonesia	227,898	9.1
Oct. 8, 2005	Pakistan	86,000	7.6
May. 26, 2006	Java, Indonesia	5,749	6.3
May. 12, 2008	Eastern Sichuan, China	87,587	7.9
Jan. 12, 2010	Near Port-au-Prince, Haiti	222,570	7.0
Feb. 27, 2010	Off the coast of central Chile	525 [c]	8.8
Mar. 11, 2011	Pacific Ocean, East of Oshika Peninsula, Japan	15,822 [d]	8.9-9.1

[a]Data mainly from: http://www.eoearth.org/article/Earthquake
[b]Data from United States Geological Survey (USGS) 2010
[c]Data from: http://www.interior.gob.cl/filesapp/listado_fallecidos_desaparecidos_27Feb.pdf
[d]Data from Japanese National Police Agency (10.12.2011)

Figures of death to us might be only numbers but for the families who lost their relatives in the earthquakes, one or more means their whole lives changed. If we can know more about the earthquake mechanism, we can better protect ourselves from earthquakes.

There are many different prospects of doing research on earthquake and the final goal all the researchers want to achieve is the prediction of the earthquakes. However, due to the complexity of the earth's structure and motions, before we could predict the earthquakes, there are many related topics of the earthquake that we need to seek for convincing answers. The satellite missions offer us a great opportunity to observe the earth from the special eyes in the sky which have global views.

Papers on the application of the gravity method in geodesy emerge only in the recent ten years, because of the launching of the global satellites CHAMP, GRACE and GOCE. And indeed the gravity method has its advantages compared to the other methods:

1. Massive: Global scale;

2. Insight: Gravity changes can reveal the underground mass changes which do not cause so much motion on the earth surface;

3. Convenient: Superior to the traditional methods, the spaceborne gravimetry can get the data from the ocean and glacier parts..

Meanwhile indeed part of the observed fluctuations are due to geodynamic causes, but as the gravity changes are dominated by the hydrology, ocean, atmosphere changes, the geodynamic signal are usually the smallest. In geoscience, there are many unknown topics, such as the mantle rheology, mantle water diffusion, postseismic gravity changes. The satellite gravimetry data can be an independent source for such researches. The model extracted from such model can help to constrain the seismological model as well.

Achievements in this thesis:

1. Modeling the earthquakes signals from GRACE;
2. Analysis the coseismic and postseismic signals signals from GRACE;
3. Compare some of the geophysical interpretations by different authors.

1.3 Outline of the Work

Chapter 2 Satellite Missions is the introduction of several satellite missions especially the GRACE mission and the application in the earthquake.

Chapter 3 Modeling of the Gravity Changes Due to Earthquakes is the part of the data processing and the modeling. It includes some mathematical basics of the spherical harmonics, filtering, Empirical Orthogonal Functions (EOF), error estimation and some necessary information about the different datasets.

Chapter 4 Data Analysis includes the analysis of the four different large earthquakes — Sumatra-Andaman Earthquake (Indonesia) 2004, Sichuan Earthquake (China) 2008, Maule Earthquake (Chile) 2010 and Tōhoku Earthquake (Japan) 2011. I will mainly focus on the co- and postseismic signal analysis of Sumatra-Andaman Earthquake.

Chapter 5 Conclusion and Recommendation provides a brief summary and results of the thesis and the outlook of the research in the future.

Chapter 2

Satellite Missions

2.1 Overview of Spaceborne Gravimetry Satellite Missions

Due to the space techniques and the innovative sensor technologies, especially accelerometers and gradiometers, and because of the development of Satellite-to-Satellite Tracking (SST) method, the satellite gravity missions CHAMP, GRACE and GOCE have caused dramatical improvements in Earth gravity field recovery.

The first gravity satellite is CHAllenging Mini-Satellite Payload for Geosciences and Application (CHAMP) see Fig. 2.1. CHAMP, which was designed as a geodesy satellite, is sponsored by Deutsches GeoForschungsZentrum (German Research Centre for Geosciences) (GFZ) and expected to work for five years. The orbit parameters of the satellite are: the inclination (87.3°) and the initial altitude (454 km). The satellite was launched on Jul. 15, 2000 and re-entered Earth's atmosphere on Sept. 20, 2010. There were many different sensors on board: dual-frequency Global Positioning System (GPS) receiver, three-axes accelerometer, magnetometer instrument package, digital ion drift meter and retroreflector array. On Sept. 19, 2010 after ten years, two months and four days (after 58277 orbits) the mission came to the end.

Figure 2.1: *CHAMP Satellite (http://www.hal.ca/height/introduction/index.htm)*

As CHAMP has achieved better results than those from SLR missions in the recovery of the earth gravity field, the mission Gravity Recovery And Climate Experiment (GRACE) followed with the intention to get even better results.

CHAMP uses the High to Low Satellite-to-Satellite Tracking (HL-SST), while except the HL-SST by the GPS on board the GRACE and following GOCE uses Low to Low Satellite-to-Satellite

Tracking (LL-SST) by K-band distance measurement as well. By using this technology, the accuracy of GRACE data is much better than CHAMP data. So much so, that temporal variations can be monitored. The details of the GRACE mission will be in Sec. 2.2.

Figure 2.2: *GOCE Mission (http://ilrs.gsfc.nasa.gov/satellite_missions/list_of_satellites/goce_general.html)*

After the GRACE mission came the Gravity Field and Steady-State Ocean Circulation Explorer (GOCE) mission by European Space Agency (ESA). The satellite was launched on Mar. 17, 2009 and the expected life is two years. The inclination of the satellite is 96.7° and the altitude is about 250 km. There are three scientific instruments on the GOCE satellite: gradiometer (three pairs of three axis, servo-controlled, capacitive accelerometers), 12-channel GPS receiver and laser retroreflector. With the help of the instruments and the low orbit, the main aim of the mission is first to determine a very high accuracy of the gravity anomalies which is about 1 mGal. The second goal is to determine the geoid with an accuracy of 1–2 cm. The final aim is to get a better than 100 km spatial resolution for the two aims mentioned above (Drinkwater et al., 2007). Such high resolution will enable us for the modeling of the structure of the Earth's crust and mantle (Ilk et al., 2005).

CHAMP, GRACE and GOCE, they perfectly complement each other. CHAMP as the first low Earth orbit satellite which collected continuously precise orbit data have brought a new level of gravity measurement accuracy and important experience for the following missions as well. The second mission GRACE achieves an extremely high accuracy for the long and medium wavelengths and furthermore it allows observing temporal gravity variations. Meanwhile GOCE, although it has lower accuracy for the lower part of the signal spectrum, will reach an extraordinary high spatial resolution for the earth static gravity field (Ilk et al., 2005) see Fig. 2.3. There are many different applications in the inter-discipline research areas by using the data of the three satellite missions. For GRACE, the application is mainly in the time variable gravity field, but for the GOCE, it is in the high resolution static field.

Since GRACE is more accurate than CHAMP and has been in the orbit for more than ten years which is much longer than GOCE, in my research the gravity field will be modeled by GRACE and in the following section the GRACE mission will be specified.

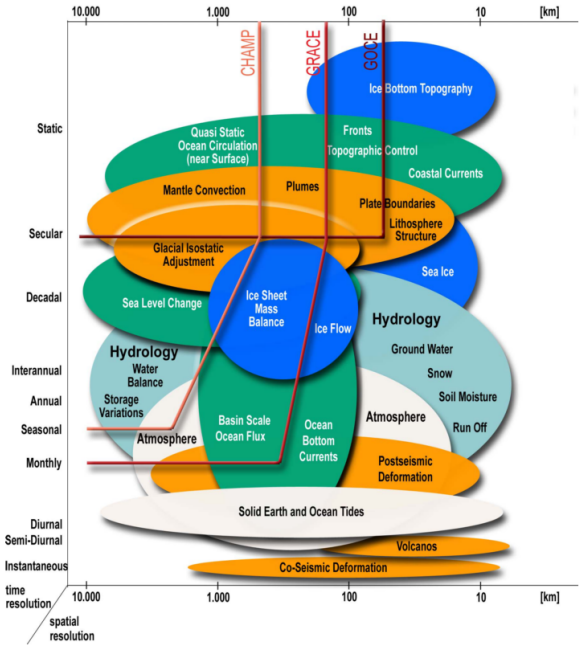

Figure 2.3: *Space & Time Resolutions of Three missions (Ilk et al., 2005)*

2.2 GRACE Satellite Mission

2.2.1 General Information

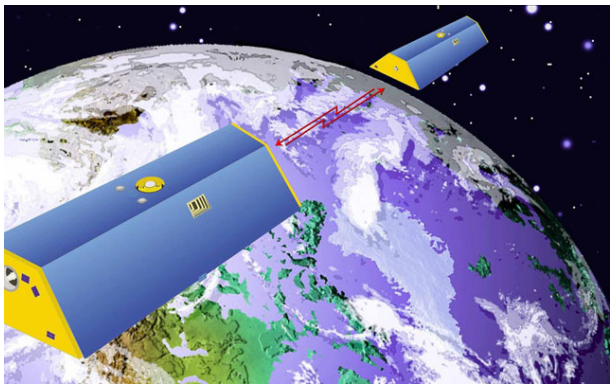

Figure 2.4: *GRACE Mission (http://grace.jpl.nasa.gov/multimediagallery/)*

GRACE mission is designed and operated by National Aeronautics and Space Administration, U.S (NASA), and Deutsches Zentrum für Luft- und Raumfahrt e.V. (German Aerospace Center) (DLR). The project management is by Jet Propulsion Laboratory, U.S (JPL). JPL, Center for Space Research (University of Texas at Austin) (CSR) and GFZ are responsible for the data processing, distribution and management.

The GRACE satellites were produced by Astrium GmbH under contract by JPL and Space Systems/Loral (SSL). The important sensors of the satellites directly inherited from the CHAMP

mission.[1] GRACE was launched on Mar. 17, 2002 from Plesetsk in Russia. GRACE mission consists of two identical spacecrafts which are 220 km apart from each other in an 89° inclination orbit 485 km above the Earth. The period of the satellite is 90 minutes. The expected life of the satellites was about five years. Although showing signs of aging, the satellites are still working up to date which is more than nine years already.

2.2.2 Instruments on Board

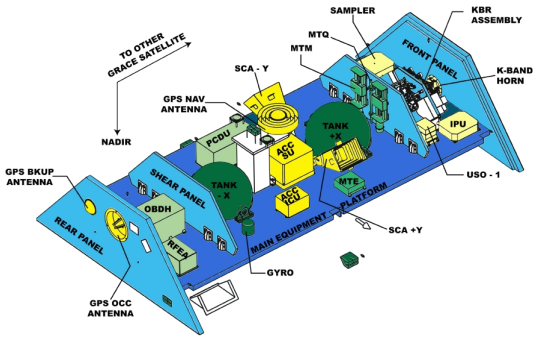

(a) Inner View

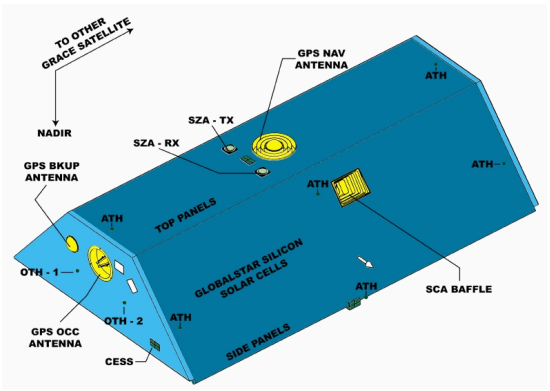

(b) Top View

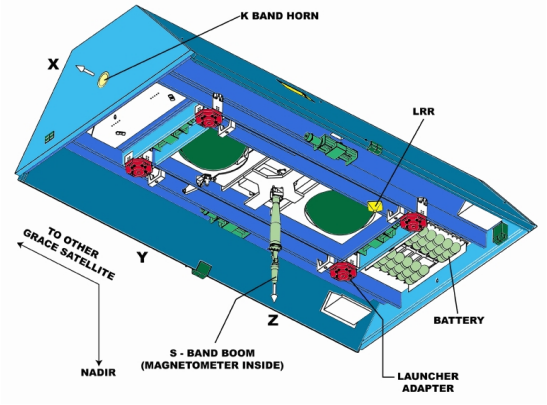

(c) Bottom View

Figure 2.5: *GRACE Satellite (Inner, Top and Bottom Views) (http://op.gfz-potsdam.de/grace/satellite/satellite.html)*

There are several instruments on the satellites (Dunn et al., 2002):

GPS: Give the usual precise orbit determination and time signals;

K-Band Ranging system (KBR): SST at K-band (24.5 GHz) and Ka-band (32.7 GHz);

Ultra-Stable Oscillator (USO): Provide clock signals for SPU and KBR;

[1] GFZ, 2011: http://www.gfz-potsdam.de/portal/gfz/Struktur/Departments/Department+1/sec12/projects/grace/grace_systems/satellites;jsessionid=184DB5407B81ABE361316426D144454F

Star Camera Assembly (SCA): Attitude observations for KBR pointing and satellite attitude control;

Instrument Processing Unit (IPU): GPS signal processing; produce output observables; perform GPS signal processing processes SCA images; collect housekeeping data; output timing signals; select KBR switches & cross-strapping;

Signal Processing Unit (SPU): Down convert Radio Frequency (RF) signals from the three GPS antennas (Precision Orbit Determination (POD), occultation and back-up) and the KBR; digitize data for IPU;

Accelerometer (ACC): Provide measurements to remove non-gravitational forces.

The basic measurement of the GRACE satellite is the distance between the two satellites by GPS and K-band microwave ranging system.

2.2.3 Gravity Recovering Approaches and Datasets

POD plays a key role in the gravity field recovery for two reasons (Liu, 2008):

1. to locate the data, such as the KBR observations;
2. to use the orbit perturbations as gravitational signal, as the orbit is mainly a result of the earth's gravitation.

Specifically for GRACE, KBR determines the range and the range rate. Meanwhile the orbits are tracked by GPS. Although GPS measurement can be used for the gravity field recovery alone, KBR is much more accurate. Generally there are five methods to recover the gravity field from the distance measurements by GPS and KBR mainly using the *energy conservation law* and *Newton's second law of motion* although energy conservation law derives from Newton's second law of motion. In the following context only the most important formulae of each approach will be listed, more details can be seen in (Liu, 2008; Abart, 2005).

Numerical integration approach The observations of this method is the deviations of the orbit tracked by GPS and the prior gravity model such as EGM96 (*The Development of the Joint NASA GSFC and NIMA Geopotential Model EGM96*, 1998).
The linearized observation equation is:

$$\delta \mathbf{r} = A\delta x + \Phi_{\mathbf{r}}\delta \mathbf{r}_0 \tag{2.1}$$

where

$\delta \mathbf{r}$	residuals from GPS tracking data to prior model for each epoch
A	Design matrix
δx	unknown potential coefficients
$\Phi_{\mathbf{r}}$	state transition matrix
$\delta \mathbf{r}_0$	initial state vector

The numerical integration method can be divided into different types: theoretically such as using the variation equations (Abart, 2005) and mathematically there are three main categories: Runge-Kutta methods, multi-step methods and extrapolation methods.

Short arc approach This approach is based on Newton's equation of motion as a boundary value problem in the form of a Fredholm-type integral. More detail can be found in (Mayer-Gürr, 2006). For an orbit arc in the time interval $[t_P, t_Q]$, $t_P < t_Q$ and the corresponding boundaries are $r(t_P)$ and $r(t_Q)$. The interpolation of any time t with the time span $[t_P, t_Q]$ is:

$$\mathbf{r}(\nu) = (1-\nu)\,\mathbf{r}(t_P) + \nu\mathbf{r}(t_Q) - (t_Q - t_P)^2 \int_{\nu'=0}^{1} \mathcal{K}(\nu,\nu')\,\ddot{\mathbf{r}}(\nu')\;\mathrm{d}\nu' \tag{2.2}$$

where normalized time $\nu = \frac{t-t_P}{t_Q-t_P}$ and the kernel function is:

$$\mathcal{K}(\nu,\nu') = \begin{cases} \nu'(1-\nu) \text{ if } & \nu' \le \nu \\ \nu(1-\nu') \text{ if } & \nu' > \nu \end{cases} \tag{2.3}$$

For the twin satellites of GRACE, project the baseline (between satellite 1 and 2) into the line of sight direction:

$$\varrho(\nu) = \mathbf{e}_{\mathrm{AB}} \cdot (\mathbf{r}_2 - \mathbf{r}_1) \tag{2.4}$$

Energy balance approach By using the law of energy conservation, the relationship in inertial space between the potential V and satellite's motion is (Jekeli, 1999):

$$V = \underbrace{\frac{1}{2}|\dot{\mathbf{r}}|^2}_{E_{\mathrm{kin}}} - \underbrace{\sum_k \int_{t_0}^{t} \mathbf{F}_k \dot{\mathbf{r}}\,\mathrm{d}t}_{E_{\mathrm{ng}}} + \underbrace{\int_{t_0}^{t} \frac{\partial V}{\partial t}\,\mathrm{d}t}_{E_{\mathrm{rot}}} - E_0 \tag{2.5}$$

where

V	potential energy of the earth's gravitational field
E_{kin}	kinetic energy of the satellite
E_{ng}	work done by non-gravitational force (dissipative forces($\mathbf{F}_k$))
E_{rot}	time variation of the gravitational potential
E_0	energy constance of the system

To simplify the model, we assume that $\mathbf{F}_k = \mathbf{0}$ and a static gravitational field, Eq. (2.5) reduces to

$$V = \frac{1}{2}|\dot{\mathbf{r}}|^2 - E_0 \tag{2.6}$$

Acceleration approach This approach is based on Newton's law of motion:

$$\ddot{\mathbf{r}} = \nabla V \tag{2.7}$$

And for a precise orbit, the rough approximation is:

$$\bar{\ddot{\mathbf{r}}} = \frac{\mathbf{r}(t-\delta t) - 2\mathbf{r}(t) + \mathbf{r}(t+\delta t)}{(\delta t)^2} \tag{2.8}$$

The more detailed description can be found in (Reubelt et al., 2003)

Mascons approach This method is described in (Rowlands et al., 2005)

$$\left.\begin{matrix}\delta C_{lm}\\ \delta S_{lm}\end{matrix}\right\} = \frac{\left(1+k_l'\right) R^2 \rho\left(t\right)}{\left(2l+1\right) M} \int Y_{lm}\left(\Phi\right)\, \mathrm{d}\Phi \tag{2.9}$$

where

k_l' loading Love number of degree l
ρ surface density at epoch t

Despite the differences in the methods for the gravity field recover, the selection of different earth models such as the prior gravity model can also lead to changes in the datasets of GRACE. As a result, there are many versions of GRACE datasets: GFZ, CSR, JPL, GSFC, CNES, ITG and DEOS.

Table 2.1: *GRACE Datasets*

Dataset	$L_{\max}$	Interval	Recovery Approach	Raw Data
GFZ	120	monthly	Numerical integration	GPS & KBR
CSR	60	monthly	Numerical integration	GPS & KBR
JPL	120	monthly	Numerical integration	GPS and KBR
GSFC	60	monthly	Mascons	KBR
CNES	50	10-day	Numerical integration	GPS, KBR LAGEOS−1/2SLR
ITG	60	monthly	Short arc	GPS & KBR
DEOS	$50-120$	monthly	Acceleration	GPS & KBR

2.3 Application to Earthquake Monitoring

There are many applications of these satellite gravity missions. Fig. 2.6 shows the mass changes by the hydrological cycles such as ice mass changes, rainfall as well as the geophysical phenomenon: viscosity, mantle rheology.

The earthquake researches depending on the CHAMP mission was based on the magnetic measurement (Zakharenkova et al., 2008; Balasis and Mandea, 2007) and the Earth's inertial tensor change (Gross, 2003).

Sun and Okubo (1993) developed the conventional dislocation theory for spherical harmonics, which is the basis in this work for GRACE analysis of earthquake signals. They compared the analytical expressions of degree variances of the coseismic geoid and gravity changes for shear and tensile sources for three real earthquakes and the expected errors of GRACE. The result was that coseismic deformations for earthquakes with seismic magnitudes above $M_w = 7.5$ were expected to be detected by GRACE (Sun and Okubo, 2004).

Soon after the publication of the paper, the devastating Sumatra-Andaman Earthquake took place in Indonesia. Two years later the article published on *Science* magazine put the result of Sun's work into reality. Han et al. (2006) is the first paper of using GRACE data to detect

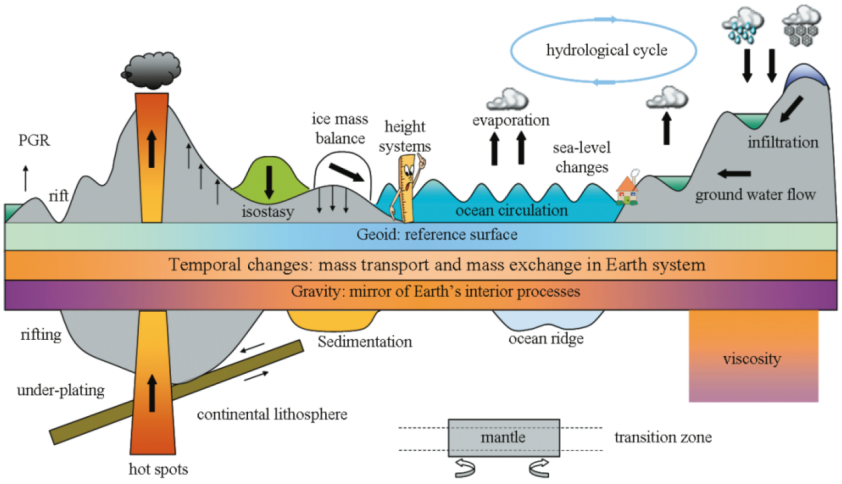

Figure 2.6: *Geophysical Phenomenon Related to the Earth Mass Changes (Ilk et al., 2005)*

a real earthquake and he got a conclusion that it was hard to get by the traditional geodetic methods or even the seismological methods. Han used his own method to process GRACE data and applied the Gauss filter for the gravity field. For the analysis of the earthquake signal, the method of the mean of GRACE gravity anomaly data was used and GRACE results was compared to a seismically derived dislocation model.

Due to Han's successful application of GRACE data to the earthquake analysis, in the following years, many geodesists were carrying out related work in the Sumatra Area. By the method of mean, Han could well display the coseismic signals. But due to the limitation of the time span after the earthquake the postseismic signals was not analyzed.

Ogawa and Heki (2007) is the first to derive the postseismic signal from the Sumatra earthquake. They used the CSR Level 2 release 1 data and Gauss filter for GRACE data. Different from Han et al. (2006), they modeled the annual, biannual signals and earthquake parameters as well. They found the significant postseismic signal in GRACE data after 2004 in the Sumatra area and it was the first detection of the postseismic gravity/geoid changes with satellite gravimetry. The mechanism of such signal was worth investigation. They analyzed many of the results in this area by GPS researches and it could not be explained by the afterslip model and the viscous relaxation of the mantle. So the third mechanism — water diffusion around the down-dip end of the fault raised. But they did not provide any modeling of the geoid variations caused by this process (Panet et al., 2010). Chen et al. (2007) used the CSR Level 2 release 4 data for the analysis and used the destriping filter which had less noise than the results from (Han et al., 2006) from the release 1 data.

Panet et al. (2007) applied wavelet analysis in the Sumatra area because it is better to separate the different components of the relaxation and to localize the coseismic gravity low in the Andaman. But for the mechanism of the postseismic signal, they concluded that it was due to the the response of a highly viscous material under the active Central Andaman Basin and partly related to the afterslip (Panet et al., 2007).

EOF analysis can also be utilized in earthquake research. However, we could not detect any event of M_w smaller than 8, because the signal of the earthquakes would be smaller than the noise level (de Viron et al., 2008). This conclusion was different from Sun and Okubo (2004)

which set the limit to $M_w = 7.5$. The dataset was Centre National d'Etudes Spatiales (National Center for Space Studies, France) (CNES) release 1 and they used the EOF decomposition, then looked for the jump in the time event and did the test. The explanation of the EOF results was hard to do because of the noise of GRACE data and the limited resolution (de Viron et al., 2008).

The spherical harmonic coefficient as well as the synthesized gravity field can also show the changes when the large earthquakes take place. Cannelli et al. (2008) used the statistical method to detect the changepoint in the spherical harmonic coefficient and found a statistically significant deviation of the low-degree J_l time series from their secular trend when fitting the GRACE time series by a bilinear function. Han and Ditmar (2007) used the localized spherical harmonics to detect the earthquake signals. The Sumatra-Andaman Earthquake significantly broke the time series of many of the global spherical harmonic coefficients below degree and order 55, which could be detected only after localizing the global coefficients at the right place. In the following year, Han used the Slepian basis function to detect the earthquake from GRACE data. The Slepian basis functions are particularly suitable for analyzing the regional mass variations associated with the large earthquakes because first they are concentrated in the region and secondly the mutually orthogonal and harmonic as well (Han et al., 2008).

de Linage et al. (2009) used both a spectral window with a cosine taper over degree 30–50 and Gauss filter to process Le Groupe de Recherche de Géodésie Spatiale (Space Geodesy Research Group, France) (GRGS) and CSR GRACE data and applied the least squares adjustment to model the earthquake signals and showed agreement with previous researches. However, the interpretation of the coseismic signal which was caused by the ocean mass lateral redistribution was different from Han et al. (2006). Meanwhile, the estimated postseismic relaxation was 0.7 year which was different from 0.6 year by Ogawa and Heki (2007).

In the previous papers, all the authors did not consider the Nias earthquake in 2005 in GRACE data. The reason was that the Nias earthquake was so close to the Sumatra earthquake that it was hard to separate them. Actually this was only a hypothesis and nobody proved it. Einarsson et al. (2010) used a statistic method to prove that it was not possible to separate the Sumatra earthquake from the Nias earthquake only by using GRACE data.

The most recent research was done by Panet et al. (2010), using GRGS/CNES data and Continuous Wavelet Transform (CWT) to analyze the Sumatra area and combining GPS and GRACE. They concluded that the postseismic signal was due to the upper mantle rheology and GRACE detected well the density variations resulting from large-scale deformation and provided a unique view of the mantle viscous response to the earthquakes. Using the GRACE Level 1 data to invest Sumatra-Andaman Earthquake and Maule Earthquake were also done by the (Han et al., 2010).

Except the focus on Sumatra-Andaman Earthquake (Indonesia) 2004, Maule Earthquake (Chile) 2010 and Tōhoku Earthquake (Japan) 2011 are also being investigated by Heki and Matsuo (2010*b*), Matsuo and Heki (2011) and Han et al. (2010) using GRACE data. Further research on the ocean height in Sumatra was done by Broerse et al. (2011).

Chapter 3

Modeling of the Gravity Changes Due to Earthquakes

3.1 Representation of the Gravity Field

Gravity field outside the earth is a *Laplace field*, which has no divergence ($\nabla \cdot \mathbf{g} = 0$) and is conservative ($\nabla \times \mathbf{g} = \mathbf{0}$). So the gravity potential ($\mathbf{g} = \nabla V$) fulfilled the Laplace equation which is the special form of the Possion's equation of which the right side is 0:

$$\Delta V = 0 \tag{3.1}$$

The solutions are called harmonic function (see Appendix. A). The potential of gravitation is a harmonic function outside the attracting masses but not inside the masses: there it satisfied the general form of Poisson's equation. Solutions of the Laplace equation of the gravitation field in Spherical Coordinates are called Spherical Harmonics:

$$V(r,\theta,\lambda) = \frac{GM}{R}\sum_{l=0}^{\infty}\left(\frac{R}{r}\right)^{l+1}\sum_{m=0}^{l}\tilde{P}_{lm}(\cos\theta)(\tilde{C}_{lm}\cos m\lambda + \tilde{S}_{lm}\sin m\lambda) \tag{3.2}$$

where

$V(r,\theta,\lambda)$	gravitational potential at the point with spherical coordinates (r,θ,λ)
GM	constant of the earth
R	radius of the earth
$\tilde{P}_{lm}$	Normalized Legend functions
$\tilde{S}_{lm}$, $\tilde{C}_{lm}$	Normalized Stokes Coefficients of the spherical harmonics

More generally, not only can the gravity field be expressed into the spherical harmonics but also an isotropic gravitational field $F(\theta,\lambda)$ on the sphere:

$$F(\theta,\lambda) = \sum_{l=0}^{\infty}\Lambda_l\sum_{m=0}^{l}\tilde{P}_{lm}(\cos\theta)(\tilde{C}_{lm}\cos m\lambda + \tilde{S}_{lm}\sin m\lambda) \tag{3.3}$$

where Λ_l is the eigenvalue of the field.

Similar to the Fourier transform the transformation between the $F(\theta,\lambda)$ and the coefficients $\tilde{C}_{lm}$, $\tilde{S}_{lm}$ can be implemented by Global Spherical Harmonic Computation (GSHC) (Sneeuw, 1994) which contains Global Spherical Harmonic Synthesis (GSHS) and Global Spherical Harmonic Analysis (GSHA).

3.1.1 Global Spherical Harmonic Synthesis (GSHS)

Continuous

$$\left.\begin{matrix} A_m(\theta) \\ B_m(\theta) \end{matrix}\right\} = \sum_{l=m}^{\infty} \tilde{P}_{lm}(\cos\theta) \left\{\begin{matrix} \tilde{C}_{lm} \\ \tilde{S}_{lm} \end{matrix}\right. \tag{3.4a}$$

$$F(\theta,\lambda) = \sum_{m=0}^{\infty} \left[A_m(\theta)\cos m\lambda + B_m(\theta)\sin m\lambda\right] \tag{3.4b}$$

Eq. (3.4b) is the 1-dimensional Fourier transform along the latitude circles. There are other methods for this transformation such as the 2-dimensional Fourier transform (Sneeuw and Bun, 1996). The continuous formulae are analytical, but for the practical consideration, the discrete formulae are more useful. The function on the sphere $F(\theta,\lambda)$ has to be properly sampled according to the discretization of the grid for example

$$\begin{aligned} \lambda_i &= \tfrac{2\pi}{2L} i = \tfrac{\pi}{L} i, \quad i = 0,1,\ldots,2L-1; \\ \theta_j &= \tfrac{\pi}{L} j, \qquad j = 0,1,\ldots,2L-1. \end{aligned}$$

Discrete

$$\left.\begin{matrix} A_m(\theta_i) \\ B_m(\theta_i) \end{matrix}\right\} = \sum_{l=m}^{L} \tilde{P}_{lm}(\cos\theta_i) \left\{\begin{matrix} \tilde{C}_{lm} \\ \tilde{S}_{lm} \end{matrix}\right. \tag{3.5a}$$

$$F(\theta_i,\lambda_j) = \sum_{m=0}^{L} \left[A_m(\theta_i)\cos m\lambda_j + B_m(\theta_i)\sin m\lambda_j\right] \tag{3.5b}$$

It is obviously that Eq. (3.5b) is nothing but a discrete Fourier series.

3.1.2 Global Spherical Harmonic Analysis (GSHA)

The general formulae for GSHA corresponding to Eq. (3.3) without dimension are:

$$\left.\begin{matrix} \tilde{C}_{lm} \\ \tilde{S}_{lm} \end{matrix}\right\} = \frac{1}{4\pi} \iint_{\Phi} F(\theta,\lambda)\, \tilde{P}_{lm}(\cos\theta) \left\{\begin{matrix} \cos m\lambda \\ \sin m\lambda \end{matrix}\right\} \mathrm{d}\Phi \tag{3.6}$$

Φ is the integral area which is a unit sphere ($0 \leqslant \lambda \leqslant 2\pi$, $0 \leqslant \theta \leqslant \pi$) and $\Phi = \sin\theta\, \mathrm{d}\theta\, \mathrm{d}\lambda$. The following discussion is the practical computation of the equation above.

Continuous

$$\left.\begin{matrix} A_m(\theta) \\ B_m(\theta) \end{matrix}\right\} = \frac{1}{(1+\delta_{m0})\,\pi} \int_0^{2\pi} F(\theta,\lambda) \left\{\begin{matrix} \cos m\lambda \\ \sin m\lambda \end{matrix}\right\} \mathrm{d}\lambda \tag{3.7a}$$

$$\left.\begin{matrix} \tilde{C}_{lm} \\ \tilde{S}_{lm} \end{matrix}\right\} = \frac{1+\delta_{m0}}{4} \int_0^{\pi} \left\{\begin{matrix} A_m(\theta) \\ B_m(\theta) \end{matrix}\right\} \tilde{P}_{lm}(\cos\theta)\sin\theta\, \mathrm{d}\theta \tag{3.7b}$$

δ_{m0} is the Kronecker delta function. When $m = 0$, $\delta_{m0} = 1$ otherwise $\delta_{m0} = 0$.

The same as the GSHS, the discretization is also necessary in GSHA.

Discrete

$$\left.\begin{matrix} A_m(\theta_i) \\ B_m(\theta_i) \end{matrix}\right\} = \frac{1}{L(1+\delta_{m0}+\delta_{mL})} \sum_{j=0}^{2L-1} F(\theta_i, \lambda_j) \left\{\begin{matrix} \cos m\lambda_j \\ \sin m\lambda_j \end{matrix}\right\} \tag{3.8a}$$

$$\left.\begin{matrix} \tilde{C}_{lm} \\ \tilde{S}_{lm} \end{matrix}\right\} = \text{to be determined} \tag{3.8b}$$

L is the maximum degree and Eq. (3.8a) is the discrete Fourier transform.

There are different ways to get the $\tilde{C}_{lm}$, $\tilde{S}_{lm}$ in Eq. (3.8b). Before discussing the method, variables need to be expressed into the matrix form:

$$A = \begin{pmatrix} A_m(\theta_1) \\ A_m(\theta_2) \\ A_m(\theta_3) \\ \vdots \\ A_m(\theta_N) \end{pmatrix}, B = \begin{pmatrix} B_m(\theta_1) \\ B_m(\theta_2) \\ B_m(\theta_3) \\ \vdots \\ B_m(\theta_N) \end{pmatrix}, C = \begin{pmatrix} \tilde{C}_{mm} \\ \tilde{C}_{m+1,m} \\ \tilde{C}_{m+2,m} \\ \vdots \\ \tilde{C}_{Lm} \end{pmatrix}, S = \begin{pmatrix} \tilde{S}_{mm} \\ \tilde{S}_{m+1,m} \\ \tilde{S}_{m+2,m} \\ \vdots \\ \tilde{S}_{Lm} \end{pmatrix}$$

$$P = \begin{pmatrix} \tilde{P}_{mm}(x_1) & \tilde{P}_{m+1,m}(x_1) & \dots & \tilde{P}_{Lm}(x_1) \\ \tilde{P}_{mm}(x_2) & \tilde{P}_{m+1,m}(x_2) & \dots & \tilde{P}_{Lm}(x_2) \\ \vdots & \vdots & \ddots & \vdots \\ \tilde{P}_{mm}(x_N) & \tilde{P}_{m+1,m}(x_N) & \dots & \tilde{P}_{Lm}(x_N) \end{pmatrix}$$

According to Eq. (3.5a), the relationship between $A_m(\theta_1)$, $B_m(\theta_1)$ and $\tilde{C}_{lm}$, $\tilde{S}_{lm}$ is obvious and the matrix form is $A = PC$, $B = PS$. The unknowns in Eq. (3.8b) are $\tilde{C}_{lm}$, $\tilde{S}_{lm}$. So the most straightforward way is the *Least Squares Method* (Gauss, 1939) and the solution is:

$$C = (P^T P)^{-1} P^T A, \quad S = (P^T P)^{-1} P^T B \tag{3.9}$$

and adjust the solution to a similar way as Eq. (3.5) and (3.8) :

$$\left.\begin{matrix} \tilde{C}_{lm} \\ \tilde{S}_{lm} \end{matrix}\right\} = \frac{1}{\phi} \sum_{i=1}^{N} \tilde{P}_{lm}(\cos\theta_i) \left\{\begin{matrix} A_m(\theta_i) \\ B_m(\theta_i) \end{matrix}\right\} \tag{3.10}$$

where ideally the $P^T P = \phi I$. Unfortunately the reality is that $P^T P \neq \phi I$ because the $P^T P$ is not a diagonal matrix while Fig. 3.1 shows the normal matrix ($P^T P$) of a global field. In order to deal with the correlated unknowns, there are some methods to solve the problem:

Approximate Quadrature By comparing the Eq. (3.10) and (3.7b) we can get:

$$\left.\begin{matrix} \tilde{C}_{lm} \\ \tilde{S}_{lm} \end{matrix}\right\} = \frac{1}{4}(1+\delta_{m0}) \sum_{i=1}^{N} s_i^q \tilde{P}_{lm}(\cos\theta_i) \left\{\begin{matrix} A_m(\theta_i) \\ B_m(\theta_i) \end{matrix}\right\} \tag{3.11}$$

with weights

$$s_i^q = \frac{\pi}{N} \sin\theta_i \tag{3.12}$$

or

$$s_i^q = \frac{2}{\sum_{k=1}^{N} \sin\theta_k} \sin\theta_i \tag{3.13}$$

see (Ellsaesser, 1966)

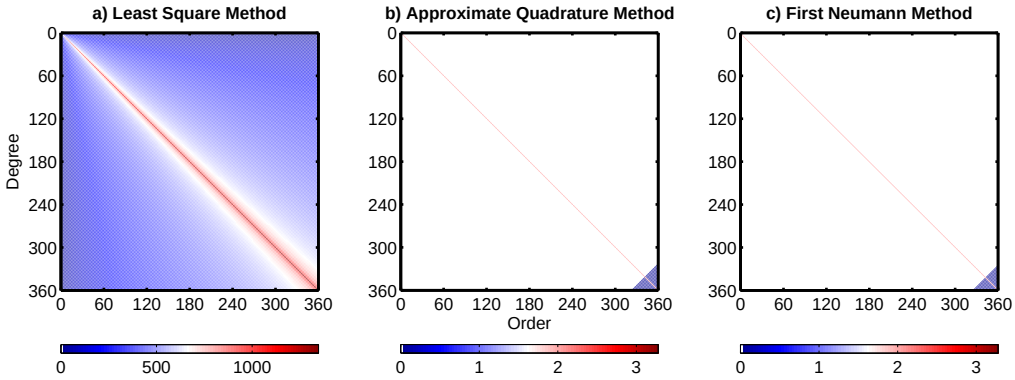

Figure 3.1: *Normal Matrices*

First Neumann Method The approximate orthogonality can be attained in the discrete case by inserting the weight matrix s_i^n which was found by Neumann in the year of 1838. The normal matrix is approximately diagonal:

$$P^T W P = 2\left(2 - \delta_{m0}\right) I \tag{3.14}$$

Therefore, Eq. (3.8b) becomes:

$$\left.\begin{matrix} \tilde{C}_{lm} \\ \tilde{S}_{lm} \end{matrix}\right\} = \frac{1}{4}\left(1 + \delta_{m0}\right) \sum_{i=1}^{N} s_i^n \tilde{P}_{lm}(\cos\theta_i) \left\{\begin{matrix} A_m\left(\theta_i\right) \\ B_m\left(\theta_i\right) \end{matrix}\right. \tag{3.15}$$

with

$$\begin{pmatrix} 1 & 1 & \dots & 1 \\ \tilde{P}_2(x_1) & \tilde{P}_2(x_2) & \dots & \tilde{P}_2(x_{L+1}) \\ \vdots & \vdots & \ddots & \vdots \\ \tilde{P}_{2L}(x_1) & \tilde{P}_{2L}(x_2) & \dots & \tilde{P}_{2L}(x_{L+1}) \end{pmatrix} \begin{pmatrix} s_1^n \\ s_2^n \\ \vdots \\ s_L^n \\ s_{L+1}^{n'} \end{pmatrix} = \begin{pmatrix} 1 \\ 0 \\ \vdots \\ 0 \end{pmatrix} \tag{3.16}$$

with weight $s_{L+1}^{n'} = \frac{1}{2} s_{L+1}^n$.

3.2 Eigenvalue

This section will mainly deal with the vector Λ_l and the transformation between different dimensions which will be used in GRACE and GLDAS model.

3.2.1 Gravity Anomaly

The following context is only a short introduction of the gravity anomaly, for more details please see (Hoffmann-Wellenhof and Moritz, 2005).

The difference between *gravity potential on the geoid* W and *normal gravity potential* U is the *anomalous potential* or *disturbing potential* T:

$$W(x,y,z) = U(x,y,z) + T(x,y,z) \tag{3.17}$$

By computing the gradient of Eq. (3.17) we can get the relationship of the three vectors:

$$\mathbf{g} = \boldsymbol{\gamma} + \boldsymbol{\delta}\mathbf{g} \tag{3.18}$$

The *gravity anomaly* at the point P is the scalar form of the Eq. (3.18):

$$\Delta g(P) = g(P) - \gamma(Q) \tag{3.19}$$

Q is the approximate location of P which is the footprint of P on the reference ellipsoid (approximated by the geosphere) (see Fig. 3.2).

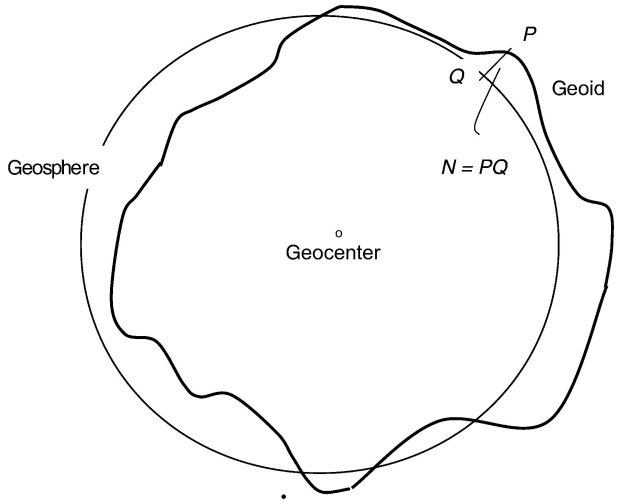

Figure 3.2: *Geoid, P & Q (Moritz, 2010)*

In order to see the changes of the gravity anomalies more clearly, subtract the gravity anomalies by the eight years' annual mean as shown in Fig. 3.3(d) and it is the field mainly discussed in the thesis.

Above all is the theoretical analysis of the gravity anomaly. The eigenvalue of the gravity anomaly can be directly derived from the *fundamental equation of physical geodesy* (Hoffmann-Wellenhof and Moritz, 2005; Sneeuw, 2006):

$$\delta g = -\frac{\partial T}{\partial r} - \frac{2}{r}T \tag{3.20}$$

Expand T into spherical harmonics and insert into Eq. (3.20):

$$\begin{aligned} \delta g &= \frac{GM}{R^2}\sum_{l=0}^{\infty}\left(-\frac{l+1}{R}+\frac{2}{R}\right)\left(\frac{R}{r}\right)^{l+1}\sum_{m=0}^{l}\tilde{P}_{lm}(\cos\theta)(\tilde{C}_{lm}\cos m\lambda + \tilde{S}_{lm}\sin m\lambda) \\ &= \frac{GM}{R^2}\sum_{l=0}^{\infty}(1-l)\left(\frac{R}{r}\right)^{l+1}\sum_{m=0}^{l}\tilde{P}_{lm}(\cos\theta)(\tilde{C}_{lm}\cos m\lambda + \tilde{S}_{lm}\sin m\lambda) \end{aligned} \tag{3.21}$$

So obviously the eigenvalue is:

$$\Lambda_l = \frac{GM}{R^2}(l-1) \tag{3.22}$$

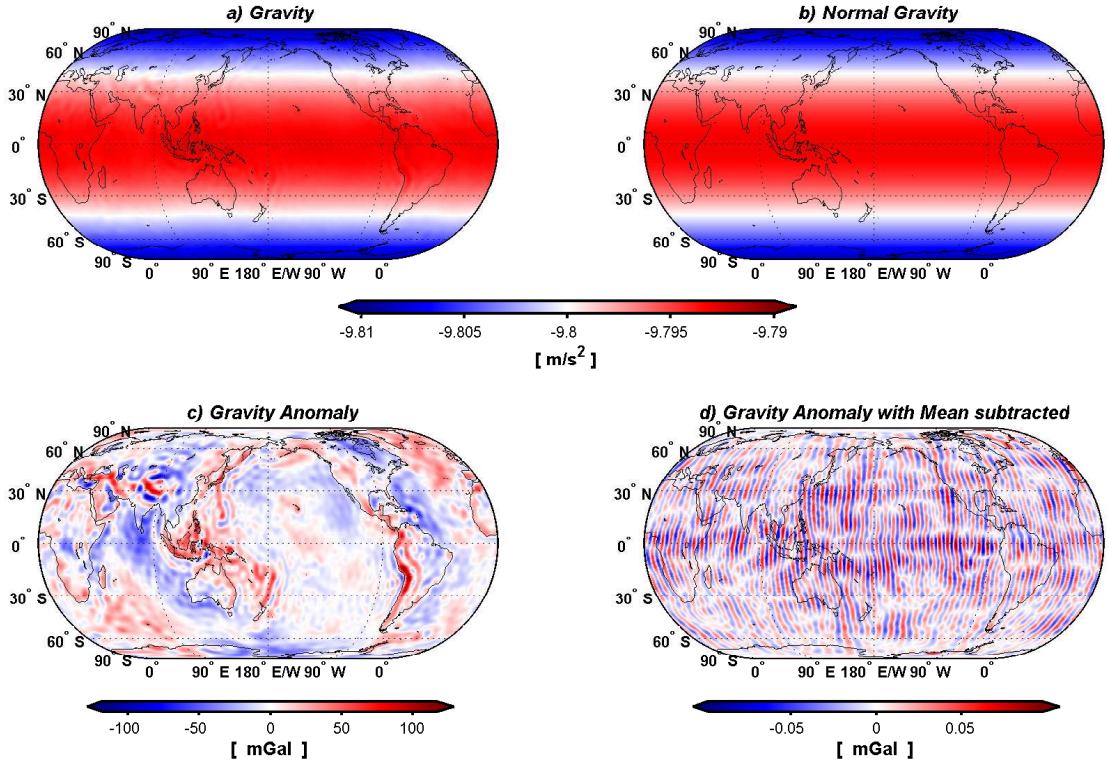

Figure 3.3: *Gravity Anomaly (CSR Mar. 2003)*

3.2.2 Equivalent Water Height (EWH)

Gravity anomaly can reflect the gravity changes in a region. Mass changes close to the surface, however, can also be expressed as surface density or, e.g, as equivalent water height. The relationship between the surface mass changes and the gravity changes is discussed in (Wahr and Molenaar, 1998). The geoid height N can be expressed in spherical harmonics:

$$N(r,\theta,\lambda) = R\sum_{l=0}^{\infty}\sum_{m=0}^{l}\tilde{P}_{lm}(\cos\theta)(\tilde{C}_{lm}\cos m\lambda + \tilde{S}_{lm}\sin m\lambda) \tag{3.23}$$

Time dependent changes in the geoid height can be also expressed:

$$\delta N(r,\theta,\lambda) = R\sum_{l=0}^{\infty}\sum_{m=0}^{l}\tilde{P}_{lm}(\cos\theta)(\delta\tilde{C}_{lm}\cos m\lambda + \delta\tilde{S}_{lm}\sin m\lambda) \tag{3.24}$$

which is the superposition law of the spherical harmonics.

Suppose $\delta\rho\,(r,\theta,\lambda)$ to be the density redistribution leading to the geoid changes. According to (Chao and Gross, 1987) $\delta\rho$ is related to δC_{lm}, δS_{lm} as follows:

$$\left.\begin{matrix}\delta C_{lm}\\ \delta S_{lm}\end{matrix}\right\} = \frac{3}{4\pi R\rho_{\text{ave}}\,(2l+1)}\int \delta\rho\,(r,\theta,\lambda)\tilde{P}_{lm}(\cos\theta) \times\left(\frac{r}{R}\right)^{l+2}\left\{\begin{matrix}\cos\,(m\lambda)\\ \sin\,(m\lambda)\end{matrix}\right\}\sin\theta\,\mathrm{d}\theta\,\mathrm{d}\lambda\,\mathrm{d}r \tag{3.25}$$

where $\rho_{\text{ave}} = 5.517 \times 10^3\ \text{kg/m}^3$ is the average density of the earth. Surface density $\delta\eta$ is derived by integrating over a thin layer:

$$\delta\eta\left(\theta,\lambda\right) = \int_{\text{thin layer}} \delta\rho\left(r,\theta,\phi\right)\ \mathrm{d}r \tag{3.26}$$

Compare to the earth radius (6371 km) the imaginary thin layer is about 10–15 km. So the term $(r/R)^{l+2} \approx 1$ and Eq. (3.25) can be reduced to

$$\left.\begin{matrix}\delta C_{lm}\\ \delta S_{lm}\end{matrix}\right\}_{\text{surf mass}} = \frac{3}{4\pi R\rho_{\text{ave}}\left(2l+1\right)} \int \delta\eta\left(\theta,\lambda\right)\tilde{P}_{lm}(\cos\theta) \times \left\{\begin{matrix}\cos\left(m\lambda\right)\\ \sin\left(m\lambda\right)\end{matrix}\right\} \sin\theta\,\mathrm{d}\theta\,\mathrm{d}\phi \tag{3.27}$$

Eq. (3.27) is the relationship between the direct gravitational attraction of the surface mass and the corresponding changes in the spherical harmonics coefficients. The overall changes of the gravity consist not only of the gravity changes of the surface mass but also the corresponding changes of the underlying solid earth loaded and deformed by the surface mass.

$$\left\{\begin{matrix}\delta C_{lm}\\ \delta S_{lm}\end{matrix}\right\}_{\text{solid Earth}} = k_l \times \left\{\begin{matrix}\delta C_{lm}\\ \delta S_{lm}\end{matrix}\right\}_{\text{surf mass}} \tag{3.28}$$

where k_l is the Love number of degree l (Farrel, 1972). Practically the (elastic) Love number see Table. 3.1 used the value described in (Han and Wahr, 1995) by using the Earth model Preliminary Reference Earth Model (PREM) (Dziewonski and Anderson, 1981).

Table 3.1: *Love Numbers. (Han and Wahr, 1995)*

l	k_l	l	k_l	l	k_l
0	+0.000	7	−0.081	30	−0.040
1	+0.027	8	−0.076	40	−0.033
2	−0.303	9	−0.072	50	−0.027
3	−0.194	10	−0.069	70	−0.020
4	−0.132	12	−0.064	100	−0.014
5	−0.104	15	−0.058	150	−0.010
6	−0.089	20	−0.051	200	−0.007

Interpolation is necessary if the degree is not listed in the Table. 3.1.

In all, the whole earth changes caused by the additional surface load on earth can be expressed by the following equation which is the summation of the Eq. (3.27) and (3.28).

$$\left\{\begin{matrix}\delta C_{lm}\\ \delta S_{lm}\end{matrix}\right\} = \left\{\begin{matrix}\delta C_{lm}\\ \delta S_{lm}\end{matrix}\right\}_{\text{surf mass}} + \left\{\begin{matrix}\delta C_{lm}\\ \delta S_{lm}\end{matrix}\right\}_{\text{solid Earth}} \tag{3.29}$$

Above all, the discussion and equations are for an arbitrary field which can be treated as a surface mass load on earth. The gravity change can be assumed as equivalent to the mass change in a thin layer on the surface of the earth. If the density of thin layer is equal to the

density of the water, we call it Equivalent Water Height (EWH). EWH is obtained by dividing the surface density $\delta\eta$ by the density of water:

$$h_{\mathrm{w}} = \frac{\delta\eta\,(\theta,\lambda)}{\rho_{\mathrm{w}}} \tag{3.30}$$

Equivalent water height can also be expanded into spherical harmonics similar to Eq. (3.24):

$$h_{\mathrm{w}}(\theta,\lambda) = R\sum_{l=0}^{\infty}\sum_{m=0}^{l}\tilde{P}_{lm}(\cos\theta)(\delta\hat{C}_{lm}\cos m\lambda + \delta\hat{S}_{lm}\sin m\lambda) \tag{3.31}$$

Comparing Eq. (3.31), (3.30) and (3.3) and using Eq. (3.6):

$$\left.\begin{matrix}\delta\hat{C}_{lm}\\ \delta\hat{S}_{lm}\end{matrix}\right\} = \frac{1}{4\pi R\rho_{\mathrm{w}}}\int \delta\sigma\,(\theta,\lambda)\tilde{P}_{lm}(\cos\theta)\times\left\{\begin{matrix}\cos(m\lambda)\\ \sin(m\lambda)\end{matrix}\right\}\sin\theta\,\mathrm{d}\theta\,\mathrm{d}\phi \tag{3.32}$$

Both Eq. (3.27) and Eq. (3.32) are the surface mass load or pressure. Comparing those two equations:

$$\left\{\begin{matrix}\delta C_{lm}\\ \delta S_{lm}\end{matrix}\right\}_{\text{surf mass}} = \frac{3\rho_{\mathrm{w}}}{\rho_{\mathrm{ave}}\,(2l+1)}\times\left\{\begin{matrix}\delta\hat{C}_{lm}\\ \delta\hat{S}_{lm}\end{matrix}\right\} \tag{3.33}$$

Considering the solid earth changes, the whole earth changes caused by the surface mass load can be expressed:

$$\left\{\begin{matrix}\delta C_{lm}\\ \delta S_{lm}\end{matrix}\right\} = \frac{3\rho_{\mathrm{w}}\,(1+k_l)}{\rho_{\mathrm{ave}}\,(2l+1)}\times\left\{\begin{matrix}\delta\hat{C}_{lm}\\ \delta\hat{S}_{lm}\end{matrix}\right\} \tag{3.34}$$

Combine with Eq. (3.24). Finally the eigenvalue is

$$\Lambda_l = \frac{\rho_{\mathrm{ave}}\,(2l+1)}{3\rho_{\mathrm{w}}\,(1+k_l)}R \tag{3.35}$$

Above all are the equations for the equivalent water height.

These and other quantities (not derived here) are summarized in Table. 3.2.

Table 3.2: *Options of Eigenvalue Λ_l (Rummel and van Gelderen, 1995)*

Quantity	Dimension (Λ_l)	Unit
None	1	$-$
Geoid	R	m
Gravity Potential	$\frac{GM}{R}$	m^2/s^2
Gravity Anomaly	$(l-1)\,\frac{GM}{R^2} \times 10^5$	mGal
First Radial Derivative	$-(l+1)\,\frac{GM}{R^2} \times 10^5$	mGal
Second Radial Derivative	$(l+1)\,(l+2)\,\frac{GM}{R^3} \times 10^9$	E
Surface Gradient	$\sqrt{l\,(l+1)}$	rad
Equivalent Water Height	$\frac{\rho_{\text{ave}}}{3\rho_{\text{w}}} \cdot \frac{2l+1}{1+k_l} R$	m
Surface Mass Density	$\frac{\rho_{\text{ave}}}{3} \cdot \frac{2l+1}{1+k_l} R$	kg/m^2

3.3 Low Degree Term of the Field

Before launching the GRACE satellites, experts have pointed out that the ocean tide models at that time (2002) were not accurate enough to correct GRACE data at harmonic degrees lower than 47 and the accumulated tide errors might affect the GRACE data up to harmonic degree 60 (Knudsen, 2003; Knudsen and Andersen, 2002). Furthermore, the ocean tide model errors are already considered as a dominant error source for gravity field retrieved from GRACE (Visser et al., 2010). Table. 3.3 lists the eight major ocean tidal components.

Table 3.3: *Major Tides (Knudsen and Andersen, 2002; Visser et al., 2010)*

Constituent	Frequency [Day]	Alias [Day]	Origin
Semi-diurnal			
M_2	0.5175	13.6	Lunar principal
S_2	0.5000	162.2	Solar principal
N_2	0.5274	9.1	Lunar major elliptic of M_2
K_2	0.4986	1460	Lunar/Solar declinational
Diurnal			
K_1	0.9973	0.9969	Solar declinational
O_1	1.0758	0.9969	Lunar principal
P_1	1.0028	0.9969	Solar principal
Q_1	1.1195	0.9969	Lunar elliptic of O_1

It is known that C_{20} is not well-determined by GRACE because the GRACE orbit geometry is less sensitive to this coefficient of the gravity field (Tapley et al., 2004). The C_{20} term is related to the earth dynamic oblateness (J_2) by $C_{20} = -J_2/\sqrt{5}$. In Gross et al. (2008), the author compared different degree-2 terms from GRACE (CSR), SLR, GPS and modeled by the sum of the effect due to atmospheric surface pressure, ocean-bottom pressure, land hydrology and the global mass-conserving ocean layer and concluded that SLR measurements were found to agree best with the modeled degree-2 terms. So here only the GRACE and the SLR C_{20} are compared.

(a) C_{20} from GRACE and SLR

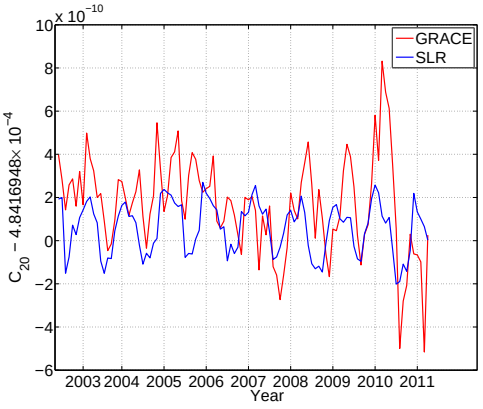

(b) Fourier Analysis of C_{20} from GRACE and SLR

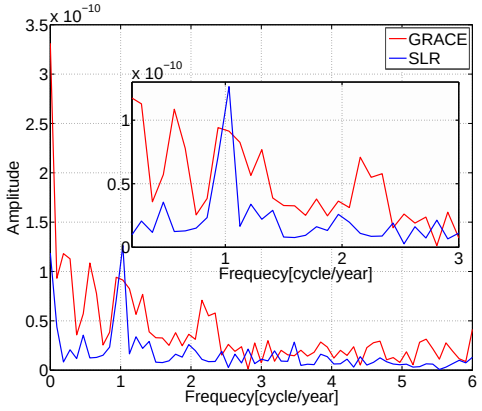

Figure 3.4: *Analysis of the C_{20} Term from GRACE and SLR*

The maximum difference between the time series of the GRACE (CSR) and SLR C_{20} terms is $7.1782 \times e^{-10}$, from 2002 to 2009 the RMS of the difference is $1.7488 \times e^{-10}$, however from 2009 to 2011 the RMS increases to $2.9136 \times e^{-10}$ (see Fig. 3.4(a)). In the spectrum domain (Fig. 3.4(b)) that the first value is only the drift and zoom into the frequency 1–3 there is only one peak in SLR term which the annual cycle. But for the GRACE (CSR) data the three peaks are at about 0.25, 0.5, 1, 2.2 cycle per year which are about 4 years, 2 years, 1 year and 167.4 days respectively. And look up in the Table. 3.3. The corresponding tides for the approximate time span is the K_2 (1460 days = 4 years) and S_2 (162 days). The GRACE data indeed significantly contained the K_2 and S_2 tide errors.

Except CSR data, GFZ and GSFC data have also been analyzed and compared with SLR data of the C_{20} term. Obviously the similar pattern was found in the other datasets see Fig. 3.5 and similar results can be found in Chen and Wilson (2008). Due to the limited data set the peak in the spectrum is not exactly at the position where the tide is but rather close and the close one is considered to be the one which is successfully detected. So the K_2 tide can be seen in CSR, GFZ and GSFC data but the S_2 tide can only be seen in the GSFC and CSR data and in GFZ data there is not so obvious S_2 tide detected but in the vicinity of the S_2 frequency there are some large values. The reason for this is the slightly different tide model (see Table. 3.4). In contrast, SLR data shows only a large peak at the normal seasonal frequency which is the combination of the atmospheric pressure variations and the variations in the distribution of water in the oceans and on land e.g. (Nerem et al., 2000).

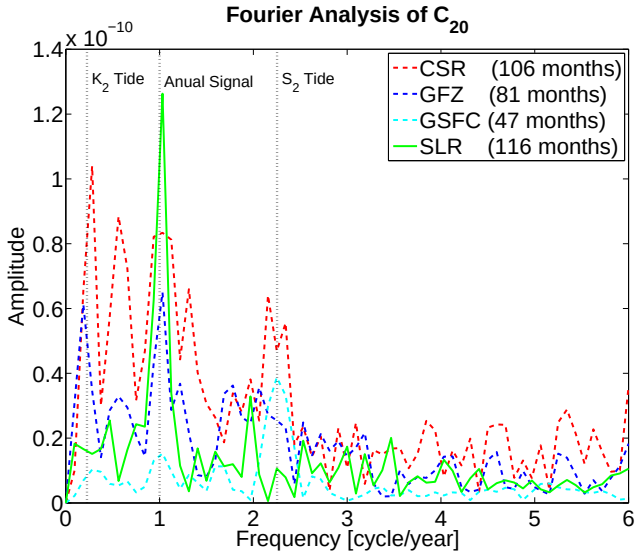

Figure 3.5: *Fourier Analysis of C_{20}*

S_2 and K_2 tides produce systematic errors in GRACE due to the inaccurate tide model and the satellite geometry. The most common way to reduce the errors is the averaging. But unfortunately the averaging cannot eliminate the S_2 and K_2 errors. The results of Knudsen and Andersen (2002) show that by using the actual orbit parameters, S_2 and K_2 are practically unreduced in GRACE monthly averaged gravity fields but the diurnal tides are almost fully reduced. So even subtracting the mean cannot reduce the errors as the alias period of the tide is more than one year.

Dataset	Model	Description
CSR	Tidal Arguments & Amplitudes/Phases	Doodson (1921) Cartwright & Tayler (1971)
	Diurnal/Semi-Diurnal Band Harmonics	Harmonics of model FES2004 to degree 100.
	Long-Period Band - all constituents	Self-consistent equilibrium model.
GFZ	Tidal Arguments & Amplitudes/Phases	Doodson (1921) Schwiderski (1983)
	Tidal Harmonics	Multi-satellite selection of harmonics for discrete tidal lines from FES2004 model (Lefevre, 2005).
GSFC	Convolution Weights	Derived from FES2004 (monthly, fortnightly, diurnal, semidiurnal) and SCEQ (Semi-annual and Annual)
	Expansion	Complete to degree 90

Table 3.4: *CSR, GFZ, GSFC Tide Models (Bettadpur, 2007; Flechtner, 2007; Watkins and Yuan, 2007)*

Here the graph shows the difference of GRACE gravity anomalies which have been subtracted the means between the GRACE field and SLR-C_{20} GRACE field. It shows the scaled C_{20} and

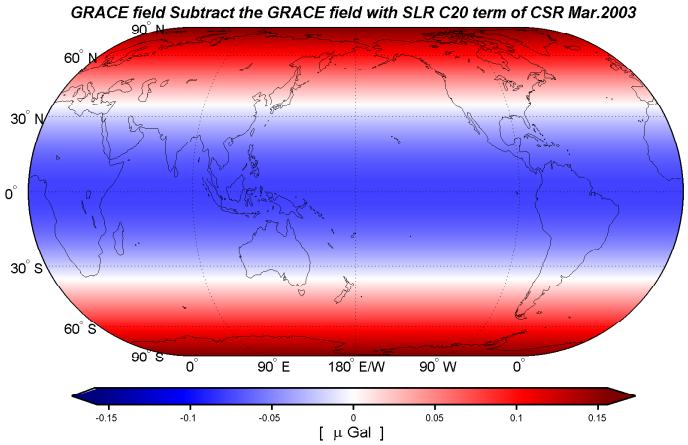

Figure 3.6: *GRACE Field Subtract the GRACE Field with SLR C_{20} Term*

the largest variation are in the high latitude areas as the results from (Chen et al., 2008; Han et al., 2005) which reports the S_2 alias near the Filchner-Ronne ice shelf.

(a) Gravity Difference at 85°N, 103°E

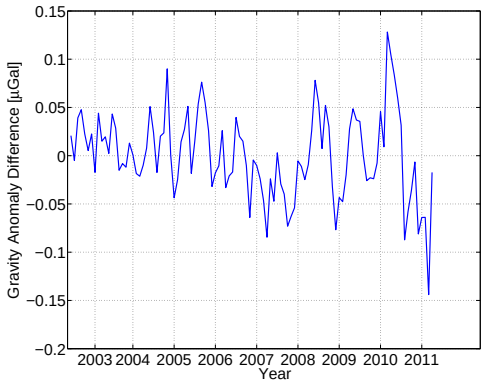

(b) Gravity Difference at 31°N, 103°E

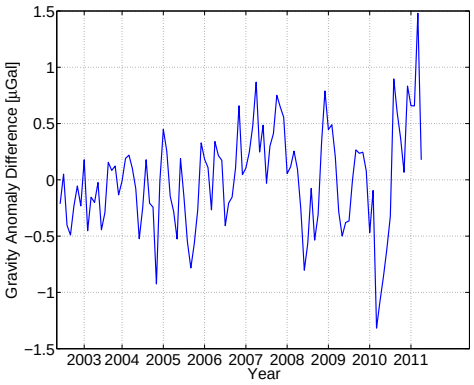

Figure 3.7: *Gravity Differences in the Spatial Domain Caused by C_{20} Term from GRACE and SLR Data*

Fig. 3.7 shows the time series changes between the GRACE and the SLR-C_{20} GRACE which indicates that approximately the influence is magnitude 1 μGal and need to be considered. And other author has proved that replacing the C_{20} term with other estimation for example the SLR will improve the gravity field (Chen et al., 2005). In this thesis, SLR C_{20} term (Cheng and Tapley, 2004) instead of the original C_{20} term in GRACE are used, but without the consideration of the correlation of the spherical harmonic coefficients.

3.4 Spatial Filtering

As the signal contains errors (see Fig. 3.3(d) and 3.8) and to reduce the errors usually the mean values are subtracted and it is the same on the sphere.

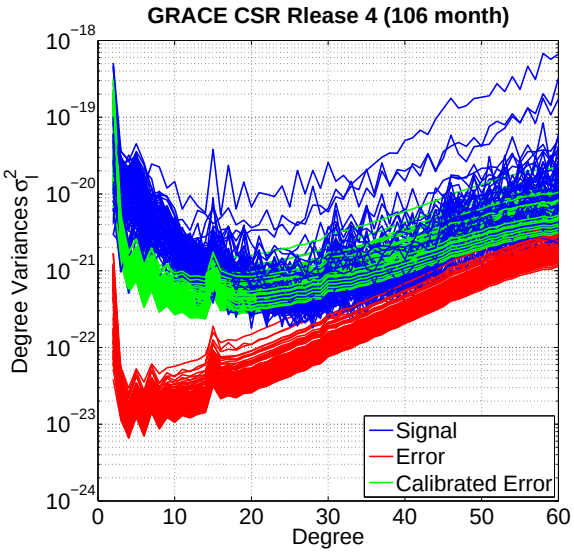

Figure 3.8: *GRACE Signals and Errors*

Filtering on the sphere is much more complex than that on the plain despite the principle is the same. Generally the filters are divided into four groups:

	Deterministic Filter	Stochastic Filter
Isotropic Filter	e.g, Gauss Filter	e.g, Wiener Filter (isotropic)
Anisotropic Filter	e.g, Fan Filter	e.g, Wiener Filter (anisotropic)

Table 3.5: *Types of Filters*

The definitions are

1. **Deterministic filter**: do not consider about the real signal and only depends on the mathematical analysis of the model;
2. **Stochastic filter**: considering the statistical property of the real observations such as Signal-to-Noise Ratio (SNR);
3. **Isotropic filter**: the weight function only depends on the degree or in another word, azimuth independent;
4. **Anisotropic filter**: the weight function depends on both degree and order.

In this thesis, only the theory of the deterministic filter will be discussed.

3.4.1 General Theory

The two dimensional "Legendre transform" is defined in Eq. (3.6). And now we use

$$\tilde{Y}_{lm}(\theta,\lambda) = \tilde{P}_{lm}(\cos\theta)\left\{\begin{array}{c}\cos m\lambda\\ \sin m\lambda\end{array}\right\} \tag{3.36}$$

which is called the *Surface Spherical Harmonic Function* (its property can be seen from Appendix. A or (Wahr, 1996)) to rewrite the formula:

$$\left.\begin{matrix}\tilde{C}_{lm}\\ \tilde{S}_{lm}\end{matrix}\right\} = \frac{1}{4\pi}\iint_{\Phi} F(\theta,\lambda)\,\tilde{Y}_{lm}(\theta,\lambda)\ \mathrm{d}\Phi \tag{3.37}$$

The following theorem and formulae are according to the report Jekeli (1981).

The general definition of the convolution of two functions defined on the sphere is:

$$H(\bar{\theta},\bar{\lambda}) = (G*F)(\bar{\theta},\bar{\lambda}) = \frac{1}{4\pi}\iint_{\Phi} G(\psi,\xi)\,F(\theta,\lambda)\ \mathrm{d}\Phi \tag{3.38}$$

where ψ, ξ are spherical coordinates, colatitude and longitude in the system rotated by the angles $\bar{\theta}$, $\bar{\lambda}$ and θ, λ are the spherical coordinates on the sphere.

Since it is rather too complex to explain the $2D$ convolution of $G(\psi,\xi)$ which is both based on latitude and longitude (anisotropic filter). Thus the $G(\psi)$ based only on the ψ (isotropic filter) is used. Eq. (3.38) can be used:

$$H(\bar{\theta},\bar{\lambda}) = (G*F)(\bar{\theta}) = \frac{1}{4\pi}\iint_{\Phi} G(\psi)\,F(\theta,\lambda)\ \mathrm{d}\Phi \tag{3.39}$$

But the difference is that $\mathrm{d}\Phi = \sin\theta\,\mathrm{d}\theta\,\mathrm{d}\lambda$ where $\cos\psi = \cos\theta\cos\bar{\theta} + \sin\theta\sin\bar{\theta}\cos\nu$ and $\nu = \lambda - \bar{\lambda}$. Next, expand the $G(\psi)$ by using the normalized and non-normalized Legendre polynomials:

$$G(\psi) = \sum_{l=0}^{\infty} g_l \tilde{P}_{l0}(\cos\psi) = \sqrt{2l+1}\sum_{l=0}^{\infty} g_l P_{l0}(\cos\psi) \tag{3.40}$$

And because of the addition theorem of the Legendre polynomials:

$$P_l(\cos\psi) = \frac{1}{2l+1}\sum_{m=0}^{l} \tilde{Y}_{lm}(\bar{\theta},\bar{\lambda})\,\tilde{Y}_{lm}(\theta,\lambda) \tag{3.41}$$

So

$$G(\psi) = \sum_{l=0}^{\infty}\frac{g_l}{\sqrt{2l+1}}\sum_{m=0}^{l} \tilde{Y}_{lm}(\bar{\theta},\bar{\lambda})\,\tilde{Y}_{lm}(\theta,\lambda) \tag{3.42}$$

Insert Eq. (3.42) into (3.39) and compare with Eq. (3.6), resulting in:

$$\begin{aligned} H(\bar{\theta},\bar{\lambda}) &= \frac{1}{4\pi}\iint_{\Phi}\sum_{l=0}^{\infty}\frac{g_l}{\sqrt{2l+1}}\sum_{m=0}^{l} \tilde{Y}_{lm}(\bar{\theta},\bar{\lambda})\,\tilde{Y}_{lm}(\theta,\lambda)\,F(\theta)\ \mathrm{d}\Phi \\ &= \sum_{l=0}^{\infty}\frac{g_l}{\sqrt{2l+1}}\sum_{m=0}^{l} \tilde{Y}_{lm}(\bar{\theta},\bar{\lambda})\underbrace{\frac{1}{4\pi}\iint_{\Phi}\tilde{Y}_{lm}(\theta,\lambda)\,F(\theta,\lambda)\ \mathrm{d}\Phi}_{f_{lm}=\left\{\begin{matrix}\tilde{C}_{lm}\\ \tilde{S}_{lm}\end{matrix}\right\}} \\ &= \sum_{l=0}^{\infty}\sum_{m=0}^{l}\frac{g_l f_{lm}}{\sqrt{2l+1}}\tilde{Y}_{lm}(\theta,\lambda) \end{aligned} \tag{3.43}$$

Therefore the spectrum of $H\left(\bar{\theta},\bar{\lambda}\right)$ is

$$h_{lm}=\frac{1}{\sqrt{2l+1}}g_l f_{lm} \tag{3.44}$$

which is *not* $h_{lm}=g_l f_{lm}$ as the the convolution theorem states in the Cartesian coordinate.

Treat Eq. (3.39) as an operator:

$$\Gamma\equiv\frac{1}{4\pi}\iint_{\sigma}G\left(\psi\right)\left(\bullet\right)\mathrm{d}\sigma \tag{3.45}$$

And it is easy to get:

$$\Gamma\tilde{Y}_{lm}\left(\theta,\lambda\right)=\frac{1}{\sqrt{2l+1}}g_l\tilde{Y}_{lm}\left(\theta,\lambda\right) \tag{3.46}$$

which means that the Γ is an eigenfunction. According to this, we can conclude that the $2D$ convolution on the sphere by the function that can be expanded into spherical harmonics is equal to the operation on the spherical harmonic coefficients by the spectrum of the corresponding function $(\bullet)$ and the kernel ($G\left(\psi\right)$). The eigenfunctions are $\tilde{Y}_{lm}\left(\theta,\lambda\right)$ and $\frac{1}{\sqrt{2l+1}}g_l$ are the eigenvalues (Meissl, 1971).

Then treat the function $G\left(\psi\right)$ as the smooth function and rewrite it to a normalized weighting function:

$$G\left(\psi\right)=\frac{w\left(\psi\right)}{\frac{1}{4\pi}\iint_{\Phi}w\left(\psi\right)\mathrm{d}\Phi} \tag{3.47}$$

where $\left|w\left(\psi\right)\right|\leqslant 1$ for $0\leqslant\psi\leqslant\pi$. Then use Eq. (3.6) but the non-normalized Legendre polynomials when $m=0$, so $\tilde{P}_l=\sqrt{2l+1}P_l$ and then integral the λ:

$$\underbrace{\left.\begin{matrix}\tilde{C}_{lm}\\ \tilde{S}_{lm}\end{matrix}\right\}}_{g_l}=\frac{\sqrt{2l+1}}{2}\int_0^{\pi}G\left(\psi\right)P_l(\cos\psi)\sin\psi\,\mathrm{d}\psi \tag{3.48}$$

the same as Eq. (3.44) and let:

$$\beta_l=\frac{g_l}{\sqrt{2l+1}} \tag{3.49}$$

practically β_l is very important, it is the eigenvalue in the Eq. (3.46) and the constant that multiply to the corresponding degree of the spherical harmonics.

Finally β_l can be directly multiplied to the spherical harmonic coefficients, considering the general case in the Eq. (3.38) and combining with Eq. (3.3), the filtered field $H\left(\bar{\theta},\bar{\lambda}\right)$ can be expressed in the spatial domain:

$$H\left(\bar{\theta},\bar{\lambda}\right)=\sum_{l=0}^{\infty}\beta_l\Lambda_l\sum_{m=0}^{l}\tilde{P}_{lm}(\cos\bar{\theta})(\tilde{C}_{lm}\cos m\bar{\lambda}+\tilde{S}_{lm}\sin m\bar{\lambda}) \tag{3.50}$$

3.4.2 Gauss Filter

For a common deterministic filter such as the Gauss filter, generally there are three steps to define the β_l which is a weight in the spectral domain for the spherical harmonics of degree l:

First, define the weight function in the spatial domain, thus the weight function of the Gauss filter is:

$$w = e^{-a(1-\cos\psi)}, \quad a > 0 \tag{3.51}$$

w expresses the weight in the spatial domain, ψ is the spherical distance and a is the averaging cap.

The second step is to normalize the w on the whole sphere by using the Eq. (3.47):

$$G(\psi) = \frac{e^{-a(1-\cos\psi)}}{\frac{1}{2a}\left(1-e^{-2a}\right)} \tag{3.52}$$

The last step is to get β_l which is the spectrum of the function $G(\psi)$ using the Eq. (3.48) and (3.49):

$$\beta_l = \int_0^{\pi} \frac{ae^{-a(1-\cos\psi)}}{1-e^{-2a}} P_l(\cos\psi)\sin\psi \, \mathrm{d}\psi \tag{3.53}$$

Due to the complexity of the integral of the $P_l(\cos\psi)$ we cannot get the explicit formula for β. Instead the recursion formulae are:

$$\begin{aligned} \beta_{l+1} &= -\frac{2l+1}{a}\beta_l + \beta_{l-1}, l \geqslant 1 \\ \beta_0 &= 1, \\ \beta_1 &= \frac{1+e^{-2a}}{1-e^{-2a}} - \frac{1}{a}. \end{aligned} \tag{3.54}$$

Wahr and Molenaar (1998) changed the normalization of w by normalizing the w (Jekeli, 1981) so that $\frac{1}{4\pi}\iint_{\Phi} w(\psi)\, \mathrm{d}\Phi = 1$. We get

$$w = \frac{b}{2\pi}\frac{e^{-b(1-\cos\psi)}}{1-e^{-2b}} \tag{3.55}$$

with $b = ln(2)/(1-\cos(r_{1/2}/R))$ and the $r_{1/2}$ the spherical distance on the earth surface where $w(r_{1/2}/R) = 1/2w(0)$.

Finally the set of formulae becomes:

$$\begin{aligned} \beta_{l+1} &= -\frac{2l+1}{b}\beta_l + \beta_{l-1}, l \geqslant 1 \\ \beta_0 &= 1, \\ \beta_1 &= \frac{1+e^{-2b}}{1-e^{-2b}} - \frac{1}{b}. \end{aligned} \tag{3.56}$$

Fig. 3.9 shows the β of Gauss filter.

3.4.3 Fan Filter

The Fan filter is developed by (Zhang et al., 2009). It is an anisotropic filter. However, the idea of the Fan filter is very straightforward. By using the equation similar to Eq. (3.50):

$$H\left(\bar{\theta},\bar{\lambda}\right)=\sum_{l=0}^{\infty}\beta_l\Lambda_l\sum_{m=0}^{l}\beta_m\tilde{P}_{lm}(\cos\bar{\theta})(\tilde{C}_{lm}\cos m\bar{\lambda}+\tilde{S}_{lm}\sin m\bar{\lambda}) \tag{3.57}$$

The same β_l and β_m can be used to smooth the degree and order of spherical harmonic coefficients. This method can change any deterministic isotropic filter into anisotropic filter. It is a very flexible filter. But on the other hand, the smoothing process is treated independently on the degree and order and this filter lacks a theoretical basis. Fig. 3.9 shows the β of Fan filter. Its name originates from the shape of the filter in the spectral domain which looks like a fan.

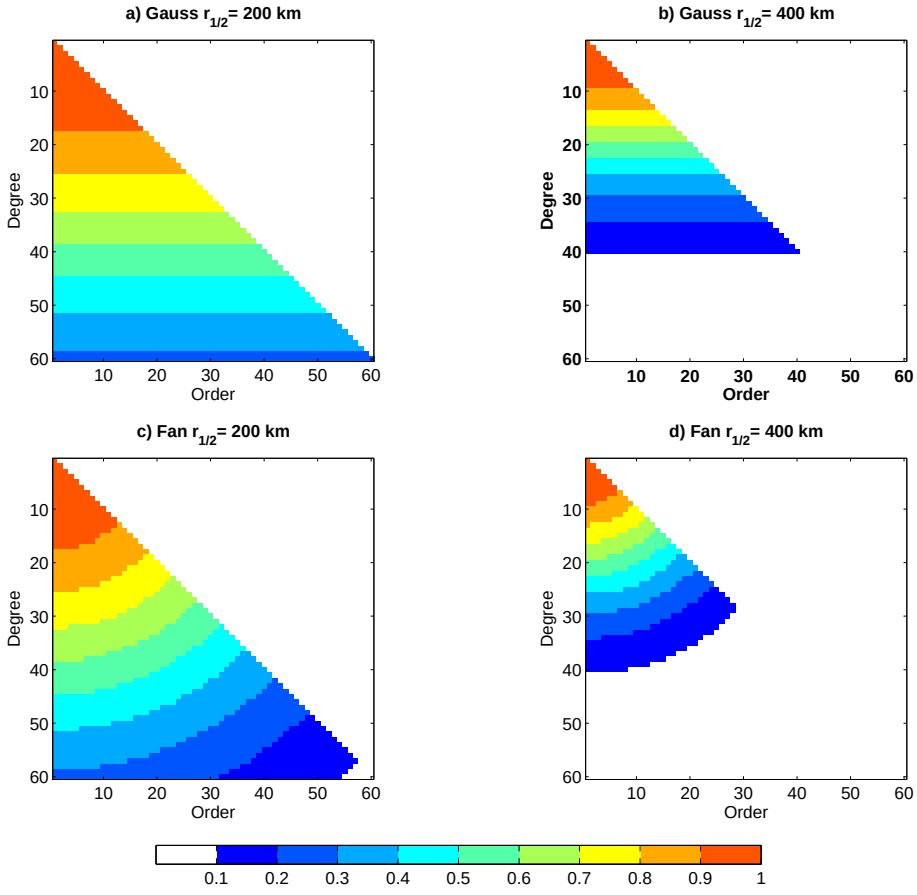

Figure 3.9: *The Spectrum Domain of Gauss and Fan Filters*

Here is the comparison between Gauss filter and Fan filter by using the damping factor (α) (Kusche, 2007):

$$\alpha=\frac{\iint\limits_{\Phi}H^2\left(\bar{\theta},\bar{\lambda}\right)\,\mathrm{d}\Phi}{\iint\limits_{\Phi}F^2\left(\bar{\theta},\bar{\lambda}\right)\,\mathrm{d}\Phi}=\frac{\sum\limits_{l=0}^{\infty}\sum\limits_{m=0}^{l}\beta_l f_{lm}}{\sum\limits_{l=0}^{\infty}\sum\limits_{m=0}^{l}f_{lm}} \tag{3.58}$$

Another formula is raised in (Devaraju and Sneeuw, 2009):

$$\alpha_{SNR} = \frac{\mathrm{SNR}\left(H\left(\Phi\right)\right)}{\mathrm{SNR}\left(F\left(\Phi\right)\right)} \tag{3.59}$$

where SNR$= \frac{\text{Signal power}}{\text{Noise power}}$.

The result for CSR data Mar. 2003 of the Gauss filter 500 km $\alpha^G_{SNR} = 0.23$ and Fan filter (Gauss filter 500 km) $\alpha^G_{SNR} = 0.24$. It indicates that the Fan filter can reduce the noise slightly better than the Gauss filter. Furthermore, several researches related to GRACE detecting earthquake signals use this filter (Ogawa and Heki, 2007; Heki and Matsuo, 2010*a*; Matsuo and Heki, 2011), in this thesis the Fan filter based on 350 km Gauss filter is used.

3.4.4 Destriping Filter

This filter is described in (Swenson and Wahr, 2006). See from Fig. 3.3(d), there are significant north to south stripes in the original field. And see from Fig. 3.10(a) and (c) which apply the Gauss filter and Fan filter only, the north to south stripes can be clearly seen as well. These three signals in the spatial domain indicate the correlation in the spectral domain. Swenson found that the even and odd coefficients do not appear correlated with one another. For a given spherical harmonic order, the simplified operation of the destriping filter is described by (Chen et al., 2007):

1. use least squares to fit a polynomial the even and odd coefficient pairs separately;
2. remove the same polynomial of a certain order such as 3.

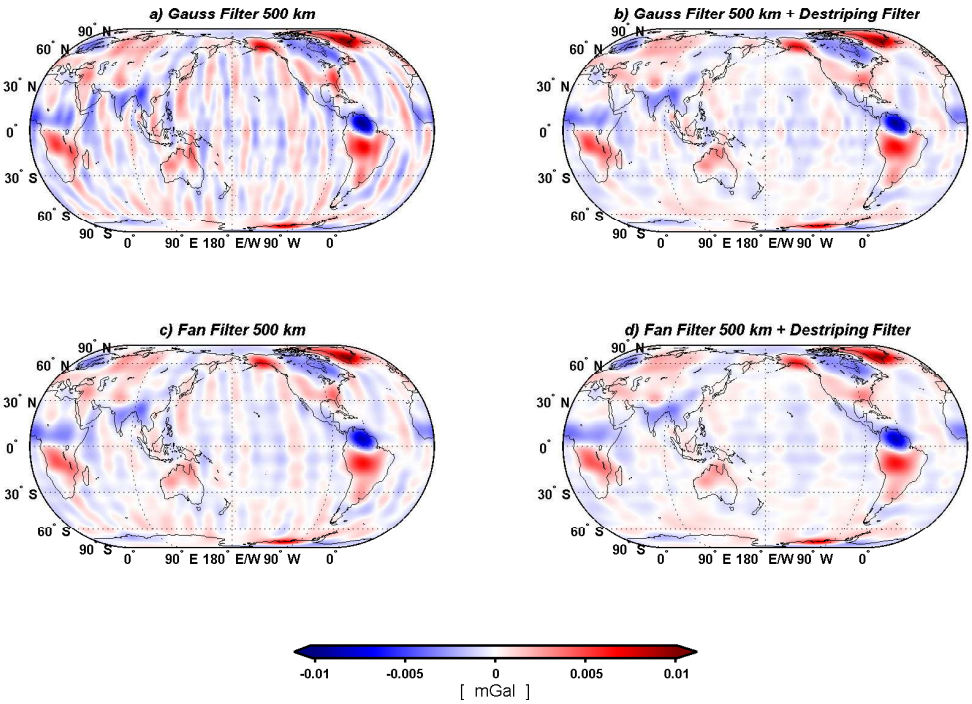

Figure 3.10: *Destriping Filter Combined with Gauss and Fan Filter*

After applying the destriping filter, in the Fig. 3.10, the north to south stripes are not so significant in 3.10(b) and (d).

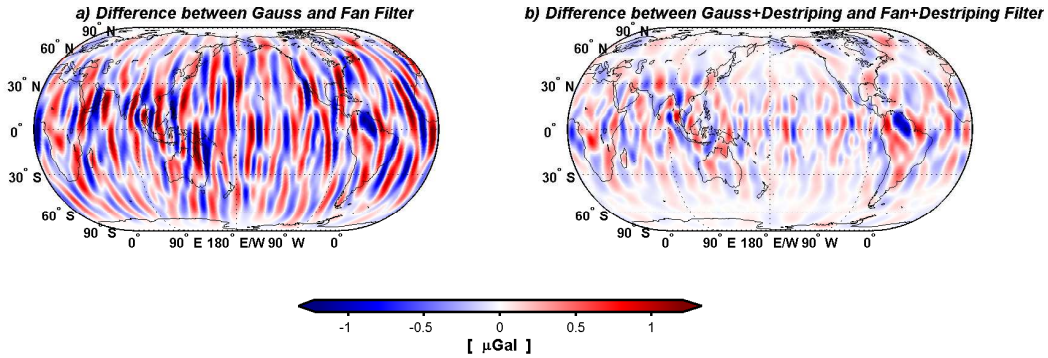

Figure 3.11: *Difference of the Fan and Gauss Filter*

Last, compare the combination of the Gauss filter and Fan filter with the destriping filter. See Fig. 3.11, the differences between the Gauss filter and Fan filter indicate that as an anisotropic filter, Fan filter eliminates the longitude dependent errors much more than the Gauss filter. And by applying the destriping filter, it removes the errors in the higher latitudes which is related to removing the correlation errors of the lower orders.

However, as in my thesis the earthquake data are analyzed and many of the earthquakes are ruptured in the north to south direction, the stripes should be cautiously removed.

Furthermore there are many other filters such as the EOF filter (Wouters and Schrama, 2007; Bentel, 2009), Regularization filter (Lorenz, 2009), Optimal filter (Klees et al., 2008) and Han's filter (Han et al., 2005) which can be used alternatively.

3.5 Eliminate the Hydrology Signal

To eliminate the hydrology signal is necessary though GLDAS model is not accurate enough. By such elimination, to some extent, the hidden earthquake signals might appear.

The hydrological effect is estimated by GLDAS model. GLDAS model is developed by scientists at Goddard Space Flight Center (GSFC) of NASA and National Oceanic and Atmospheric Administration, U.S (NOAA), National Centers for Environmental Prediction, U.S (NCEP) (Rodell et al., 2004).

GLDAS is a global, high-resolution, offline (uncoupled to the atmosphere) terrestrial modeling system which uses ground and space-based observations together to constrain Land Surface Models (LSMs) with observation based meteorological fields. GLDAS model is a numerical model and the data is provided in equivalent water height on a $1° \times 1°$ grid on JPL website (http://grace.jpl.nasa.gov/data/gldas/). Such data cannot be directly used in my research since all the data used here is expressed in the gravity anomalies. Nevertheless the transformation between the equivalent water height and the gravity anomalies should be applied and is described in Sec. 3.2.2. Meanwhile, GLDAS does not provide any uncertainty estimation.

See from the Fig. 3.12(a), there are some areas GLDAS model is not valid — Greenland, Tibet, north Canada and Siberia, due to the lack of ground data from Fig. 3.12(b). In the Sahara

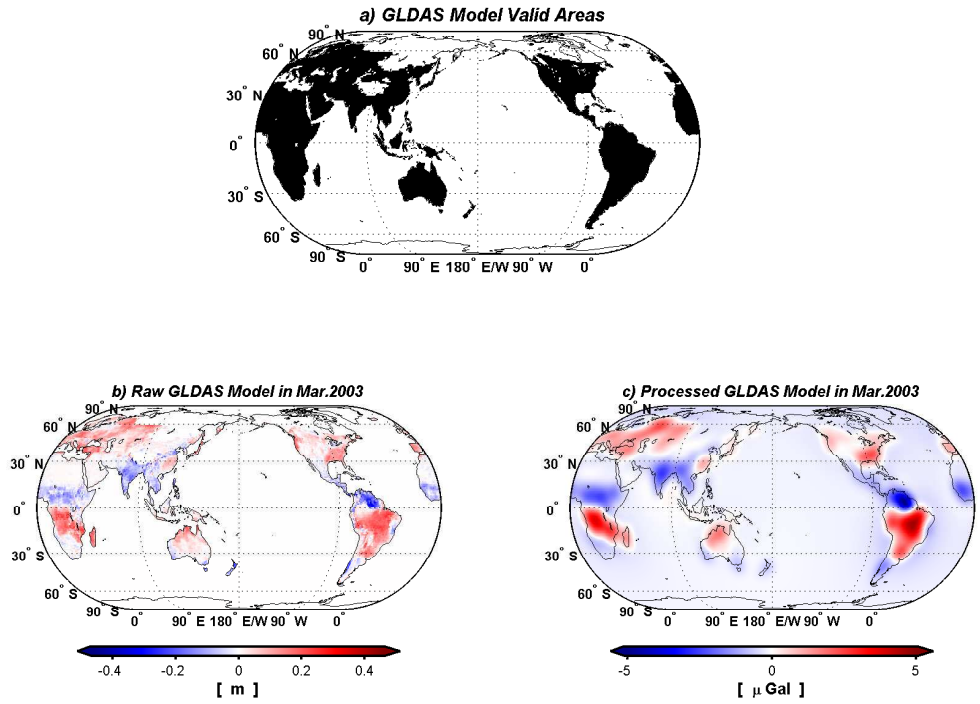

Figure 3.12: *GLDAS Model*

Desert and the Arabian Desert, GLDAS model agrees with the local properties. In the Amazon area, GLDAS indicates strong hydrological changes. In Fig. 3.12(c), because of the effect of the data leakage, the blank area disappears but it is more smooth than the figure in the left due to the increased resolution and the smoothing process. The leakage effect will affect some of the earthquake areas analyzed — Sichuan and Maule.

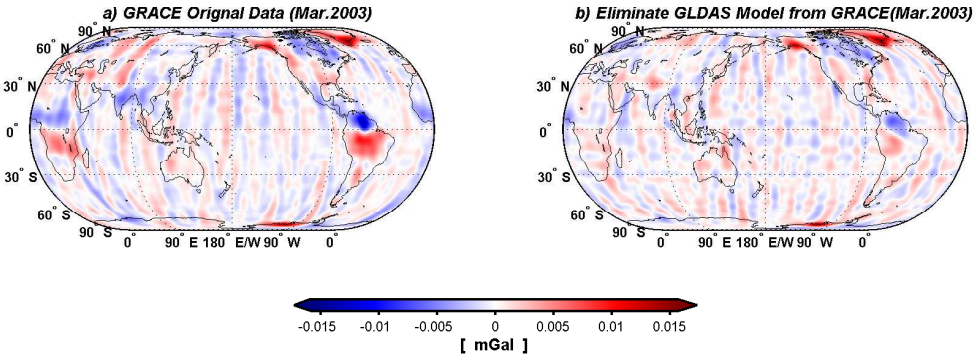

Figure 3.13: *Eliminate GLDAS Model from GRACE*

After subtracting GLDAS model from GRACE, the signals in Amazon, north Canada and south Africa where the hydrology effect is decreased significantly (see Fig. 3.13). However, GLDAS model cannot estimate all the hydrological data, for example, in the Amazon area it is reported that GLDAS cannot estimate the 2005 Amazon drought which could be estimated by GRACE data (Chen et al., 2009). Because the model is not valid globally, leakage effect and the problem of some particular area, GLDAS model cannot fully eliminate the hydrology effect while the re-

maining hydrological effect will affect the analysis of the earthquake coseismic and postseismic changes. In this thesis, the hydrology effect has the biggest influence on Sichuan area where it is near to Tibet. There is no GLDAS model in a small part of the selected area of Sichuan. Maule area is near the coastline and Amazon area, where both leakage and strong hydrology effect cannot be fully modeled by GLDAS.

3.6 Error Analysis

The Error estimation is mainly on GRACE data because GLDAS model is a numerical model that there is no error estimation for this model. For the errors in GRACE, there are two types of errors in GRACE (Wahr et al., 2006):

1. **Stochastic errors**: due to the errors in the monthly GRACE solutions;
2. **Model errors**: the difference between the true GRACE solutions and corresponding real geophysical changes such as gravity anomalies.

Here the Stochastic error is what will be discussed. The model errors can be reduced by the better geophysical model such as the tide model mentioned in Sec. 3.3.

The discussion begins from Eq. (3.57). Rewrite the equation by combining all the time-independent coefficients defining the averaging kernel together:

$$H\left(\bar{\theta},\bar{\lambda}\right)=\sum_{l=0}^{\infty}\sum_{m=0}^{l}\left(\bar{A}_{lm}\tilde{C}_{lm}+\bar{B}_{lm}\tilde{S}_{lm}\right) \tag{3.60}$$

where $\bar{A}_{lm}=\beta_l\Lambda_l\beta_m\tilde{P}_{lm}\left(\cos\bar{\theta}\right)\cos m\bar{\lambda}$ and $\bar{B}_{lm}=\beta_l\Lambda_l\beta_m\tilde{P}_{lm}\left(\cos\bar{\theta}\right)\sin m\bar{\lambda}$.

$$\delta H\left(\bar{\theta},\bar{\lambda}\right)=\sum_{l=0}^{\infty}\sum_{m=0}^{l}\left(\bar{A}_{lm}\delta\tilde{C}_{lm}+\bar{B}_{lm}\delta\tilde{S}_{lm}\right) \tag{3.61}$$

$\delta H\left(\bar{\theta},\bar{\lambda}\right)$, $\delta\tilde{C}_{lm}$ and $\delta\tilde{S}_{lm}$ are the corresponding errors from Eq. (3.60).

$\delta\tilde{C}_{lm}$ and $\delta\tilde{S}_{lm}$ are the diagonal elements of the covariance matrix which contained in GRACE data as the "calibrated errors" in the Stokes coefficients. It intends to represent all the Stochastic errors of the gravity field solutions.

Let

$$K_{\mathrm{DO}}=\left[\bar{A}_{lm};\bar{B}_{lm}\right]\ \text{ and }\ C_{\mathrm{DO}}=\left[\delta\tilde{C}_{lm};\delta\tilde{S}_{lm}\right]^T$$

where K_{DO} and C_{DO} is the degree ordering described in Appendix. C. Error propagation law is applied to analyze the errors in the spatial domain. Then rewrite the terms into the matrix format:

$$H=K_{\mathrm{DO}}\times C_{\mathrm{DO}} \tag{3.62}$$

Applying the error propagation law (see (Sneeuw and Krumm, 2008)):

$$Q_H=KQ_CK^T \tag{3.63}$$

The formula above is not the full error propagation (Sneeuw, 2000) but the block error propagation. Finally the error field is $\sigma_H=\sqrt{\mathrm{diag}\left(Q_H\right)}$ in the spatial domain, see Fig. 3.14.

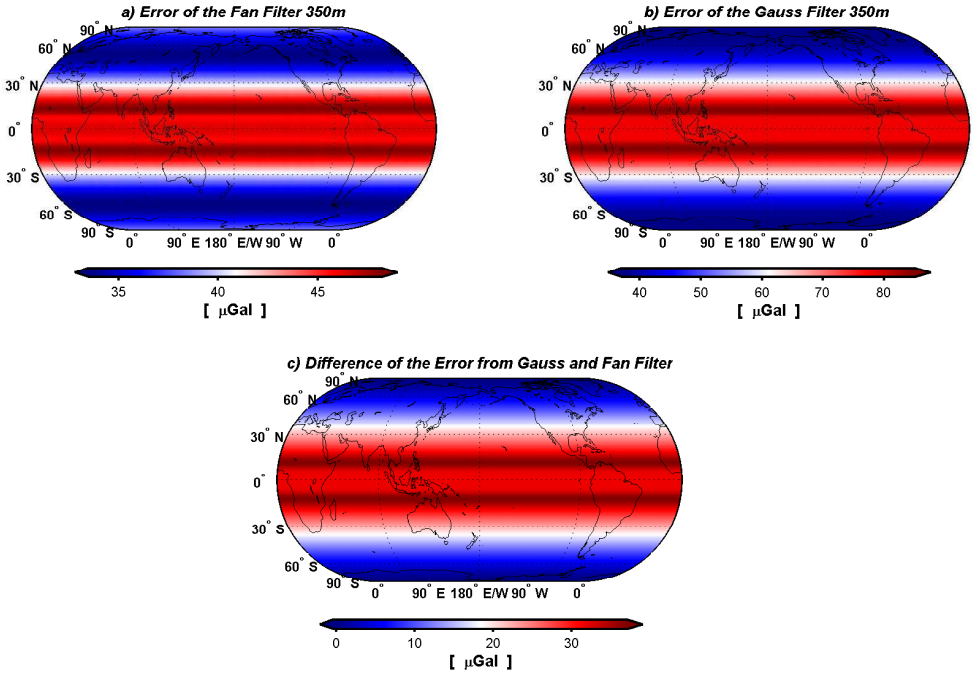

Figure 3.14: *Errors of the Fan Filter and Gauss Filter*

From the Fig. 3.14 we can observe that the largest error appears in the low latitude areas but not on the equator. The Fan filter can reduce more errors than the Gauss filter which agrees with the results of the Damping factor in Eq. (3.59). And the difference of those two filters indicates that the reduction of the errors is mainly in the low latitude area as well. Compare the Fig. 3.14 with the Fig. 3.6, the pattern is opposite but the C_{20} error is much smaller than the stochastic error.

3.7 Modeling of Earthquake-induced Changes in the Gravity Anomaly

In the gravity data the co-seismic and post-seismic changes are the most significant. And such signal can be only observed in the area near the epicenter. Since the types of earthquakes are different, the behaviors of such changes are also different.

3.7.1 Modeling of Co-seismic and Post-seismic Processes

The co-seismic process is modeled by:

$$y(t,t_0) = \begin{cases} a_1 + a_2 t + \sum_{i=1}^{2} \left(a_{2i+1}\cos(\omega_i t) + a_{2i+2}\sin(\omega_i t)\right) & \text{if } t \leqslant t_0, \\ a_7 + a_8 t + \sum_{i=1}^{2} \left(a_{2i+7}\cos(\omega_i t) + a_{2i+8}\sin(\omega_i t)\right) & \text{if } t > t_0, \end{cases} \tag{3.64}$$

The post-seismic process is modeled by:

$$y(t, t_0) = a_{13} + \sum_{i=1}^{2} \left(a_{2i+12} \cos(\omega_i t) + a_{2i+13} \sin(\omega_i t)\right) + a_{18} e^{-\frac{t-t_0}{\tau}} \quad \text{with } t > t_0 \tag{3.65}$$

where

ω_1	annual frequency
ω_2	the frequency of S_2 tide in Sec. 3.3
t	time with unit of year
t_0	the month when earthquake took place

Eq. (3.64) and (3.65) are very common equations (Einarsson et al., 2010; de Linage et al., 2009; Ogawa and Heki, 2007; Heki and Matsuo, 2010*a*; Matsuo and Heki, 2011). Therefore in this research the same model is applied.

a_1 & a_7 and a_2 & a_8 are the bias and linear trend before and after the earthquake respectively. The annual signals most probably caused by hydrology variations and the S_2 tide are estimated by $\cos(\omega_i t)$ and $\sin(\omega_i t)$ with $i = 1, 2$.

The co-seismic rupture from Eq. (3.64) is:

$$a_7 + a_8 t_0 + \sum_{i=1}^{2} \left(a_{2i+7} \cos(\omega_i t_0) + a_{2i+8} \sin(\omega_i t_0)\right) - \left[a_1 + a_2 t_0 + \sum_{i=1}^{2} \left(a_{2i+1} \cos(\omega_i t_0) + a_{2i+2} \sin(\omega_i t_0)\right)\right]$$

and the post-seismic signal is estimate by the exponential term $a_{18} e^{-\frac{t-t_0}{\tau}}$ in Eq. (3.65). The discussion of τ which is Maxwell Relaxation Time will be in the Sec. 3.7.3.

τ was fixed to 0.6 in the estimation of the postseismic signal of Sumatra by Ogawa and Heki (2007). In this thesis, τ is also estimated. However, as a small change in the estimation in τ will lead large change in the regression model as the term $a_{18} e^{-\frac{t-t_0}{\tau}}$ will enlarge the effect of the τ.

The stabilities of the two models are compared:

1.
$$y = a_1 + \sum_{i=1}^{2} \left(a_{2i} \cos(\omega_i t) + a_{2i+1} \sin(\omega_i t)\right) + a_6 e^{-\frac{t-t_0}{\tau}} \tag{3.66}$$

2.
$$y = a_1 e^{-\frac{t-t_0}{\tau}} \tag{3.67}$$

By linearization of the two model and insert the t and initial value, for Eq. (3.66):

$$A = \left[1 \quad \cos(\omega_1 t) \quad \sin(\omega_1 t) \quad \cos(\omega_2 t) \quad \sin(\omega_2 t) \quad e^{-\frac{t-t_0}{a_{40}}} \quad a_{60} e^{-\frac{t-t_0}{\tau_0}} \left(\frac{t-t_0}{\tau_0^2}\right)\right] \tag{3.68}$$

and construct the normal matrix ($N = A^T A$) and do the singular value decomposition of N. The condition number $\kappa = (\text{Max Eigenvalue}) / (\text{Min Eigenvalue})$. κ changes with the different initial number. When $a_{60} = 0.5$ and $\tau_0 = 0.7$, for Eq. (3.66) $\kappa = 1005.3$ and for Eq. (3.67)

$\kappa = 297.6$, which means Eq. (3.67) is more stable than Eq. (3.66). Although adjustment of all the parameter together will be much better than adjustment by part, the estimation of τ is still done separately otherwise the other coefficient will be affected.

The estimation is done by the least squares method and τ is estimated by Levenberg-Marquardt algorithm (Seber and Wild, 2003) or Trust-Region-Reflective algorithm (Coleman and Li, 1996) which are different from the non-linear least-squares minimization method using a quasi-Newton iterative algorithm (Tarantola, 2005) in de Linage et al. (2009). Meanwhile as the signal is not stable after two years from the earthquake time and the instability of the regression model, only two years data is estimated for τ.

The model contains the t_0 which is the changepoint in the time series. Two questions should be answered:

1. **Time domain**: As there are 106 months, when is the most significant jump in the time series? If the time t_0 detected is in the month when the earthquake took place, such detection is successful otherwise the detection fails.

2. **Spatial domain**: Whether in the spatial domain the rupture at "earthquake month" is significant only in the area near the epicenter.

Only if these two tests are both successful, can we say the changepoint detection is successful. And the discussion of those two tests will be in Sec. 3.7.2.

Meanwhile τ is not a parameter for the normal changepoint detection but a geophysical parameter which will be discussed in Sec. 3.7.3.

Here is an example of the fitting by Eq. (3.64) of GRACE data in Sumatra-Andaman Earthquake (Indonesia) 2004 on ($3°N$, $96°E$) by Fan filter 350 km to give you an expression of what kind of data that are dealt with.

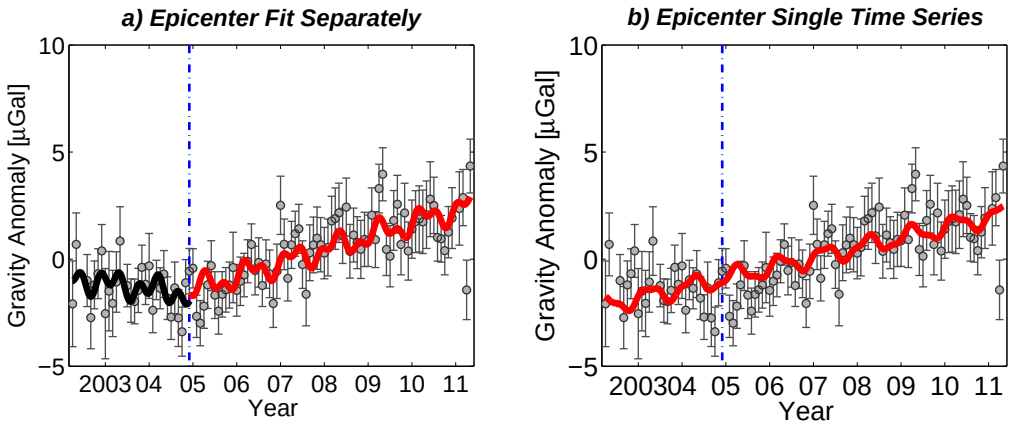

Figure 3.15: *Model the Earthquake Time Series (Sumatra)*

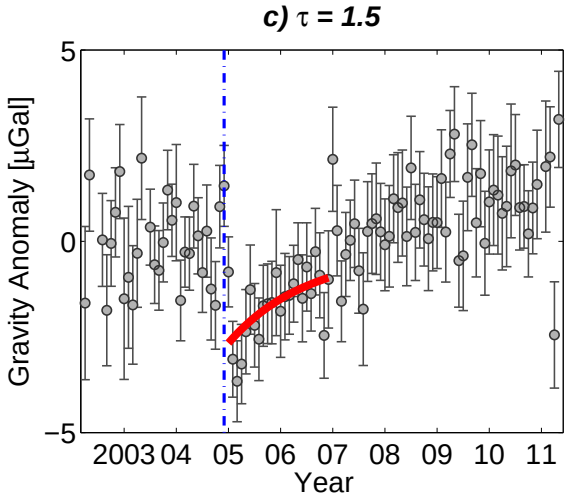

Figure 3.16: *Maxwell Relaxation Time τ (Sumatra)*

3.7.2 Changepoint Detection

A changepoint is a time at which the structural pattern of a time series changes (Lund et al., 2007). The earthquake signals are not always big jumps which can be directly seen from the time series and sometimes the coseismic jumps are hidden in the signals. However, the changepoint detection is easier than that in climate science since only one changepoint in the time series of earthquake signals. Corresponding to the two questions raised in Sec. 3.7.1, two tests are explained below:

- Two Phase detection (Lund and Reeves, 2002) is the detection of the significance in the time domain;
- Ratio test is the detection of the significance in the spatial domain.

3.7.2.1 Two Phase Changepoint Detection

The aim of the Two Phase detection is similar to Cannelli et al. (2008) that to find whether there are significant jumps in the time series at t_0 of the coefficients.

The two phase changepoint detection originally comes from the two phase regression model. The model is designed by scientists in climate science. We begin with the simplified linear trend model:

$$y(t, t_0) = \begin{cases} b_1 + c_1 t + \varepsilon_1 & \text{if } t \leqslant t_0, \\ b_2 + c_2 t + \varepsilon_2 & \text{if } t > t_0. \end{cases} \tag{3.69}$$

The hypothesis for the test is

$$H_0 : b_1 \neq b_2 \cup c_1 \neq c_2; \quad H_a : b_1 = b_2 \cap c_1 = c_2$$

First, using the least squares adjustment to fit the time series separately and get the standard deviations σ_s^2. Second, fit the time series under the alternative hypothesis and get σ_{a}^2 as well. When the true variance is unknown, the sample variance obeys the χ^2 distribution. So that

$$\sigma_{\mathrm{s}}^2 \sim \chi^2(2n) \quad \sigma_{\mathrm{a}}^2 \sim \chi^2(n)$$

where n is the number of unknowns and from Eq. (3.69) $2n = 4$.

The value for the testing is

$$F(t_0) = \frac{\left(\sigma_{\mathrm{s}}^2 - \sigma_{\mathrm{a}}^2\right)/2}{\sigma_{\mathrm{a}}^2/(N-2n)} = \frac{\delta\chi^2}{\chi^2_{N-2n}} \tag{3.70}$$

where N is the overall sample size, $2n$ is the number of unknowns and $N - 2n$ is the degree of freedom. As F is the ratio of two χ^2 distribution, F obeys the fisher distribution

$$F(t_0) \sim \mathcal{F}(2, N-2n)$$

and for each t_0, $F(t_0)$ is a measurement of how much the function in the H_0 improves the fitting of function in H_{a} (Cannelli et al., 2008). The following steps are similar to the method of data snooping (Sneeuw and Krumm, 2008) in the detection of the gross errors. All the values for $F(t_0)$ need to be computed and the maximum values should be found and perform the hypothesis testing.

However, unlike the standard $\mathcal{F}$ test with $\mathcal{F} = \frac{\chi^2(n_1)/n_1}{\chi^2(n_2)/n_2}$, the definition of $F(t_0)$ in Eq. (3.70) is more complex. The value of the $\mathcal{F}_{\max}$ is computed by simulating a time series satisfying Eq. (3.69) with H_{a} and then compute $F_{\max}$. The $\mathcal{F}_{\max}$ percentiles are obtained by simulating $1,000,000$ values for each time series with length n (Lund and Reeves, 2002).

Table 3.6: *The $\mathcal{F}_{\max}$ and $\mathcal{F}_{3,n-4}$ Percentiles. (Lund and Reeves, 2002)*

n	$\mathcal{F}_{max,0.90}$	$\mathcal{F}_{3,n-4,0.90}$	$\mathcal{F}_{max,0.95}$	$\mathcal{F}_{3,n-4,0.95}$	$\mathcal{F}_{max,0.99}$	$\mathcal{F}_{3,n-4,0.99}$
10	8.39	3.29	11.56	4.76	22.38	9.78
25	6.10	2.36	7.37	3.07	10.55	4.87
50	5.91	2.20	6.92	2.81	9.31	4.24
75	5.94	2.16	6.88	2.73	9.07	4.07
100	5.99	2.14	6.91	2.70	8.98	3.99
200	6.14	2.12	7.01	2.65	8.96	3.88
300	6.26	2.10	7.11	2.64	9.03	3.85
400	6.33	2.10	7.18	2.63	9.08	3.83
500	6.39	2.09	7.24	2.62	9.10	3.82
750	6.53	2.09	7.37	2.62	9.22	3.81
1000	6.57	2.09	7.42	2.61	9.26	3.80
2500	6.79	2.09	7.65	2.61	9.51	3.79
5000	6.98	2.08	7.85	2.61	9.68	3.79

If the length n is not listed in Table. 3.6, an interpolation is needed. Eq. (3.71) is the empirical formular for $n \geq 100$.

$$\hat{\mathcal{F}}_{max,0.95} = 3.5642 + 2\ln[\ln(n-4)]\left\{1 + \frac{4\ln[\ln(n-4)]}{n-4}\right\}, \quad n \geq 100 \tag{3.71}$$

So if $F(t_0)_{\max} > \mathcal{F}_{\max}$, H_0 is accepted, otherwise H_a is accepted.

Fig. 3.17 is the two phase results of the example data from Fig. 3.15 with $\mathcal{F}_{\max} \approx 6$.

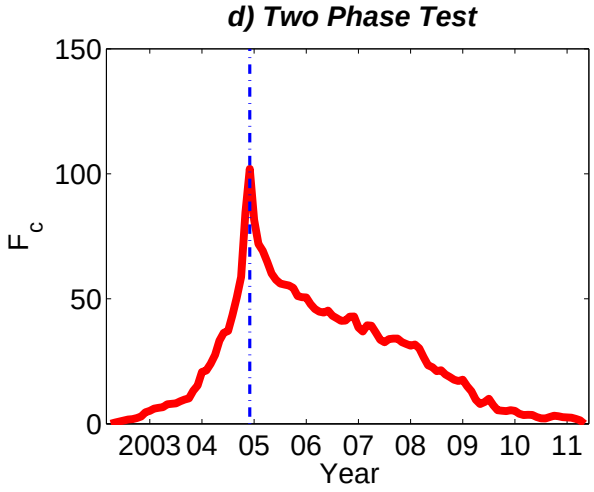

Figure 3.17: *Significant Test of Time Series (Sumatra)*

3.7.2.2 Ratio Detection

The ratio detection (e.g. Fig. 4.6(b)) is similar to the two phase test, but with the value of t_0 at the time when the earthquake took place. The formula is the same in Eq. (3.70). For each point $F(t_0)$ is computed and commonly the largest ratio appears near the area of the epicenter.

The method to interpret those two tests:

1. If the two phase test cannot detect the earthquake signals in the area around the epicenter when the earthquake took place, that means the earthquake rupture is not significant in time. There are many reasons such as a large hydrology signal. And practically the Two Phase test cannot detect the signal jump at the beginning and at the end of the time series.
2. If the ratio test fails, that means the earthquake signal is not significant in spatial at the time when earthquake took place. Other signals such as the hydrology signals sometimes can explain this phenomenon.

3.7.3 Maxwell Relaxation Time

The earth is not a rigid body, but elastic. If the lithosphere is brittle, its behavior will not be time dependent. But the deformation of the ductile rock depends on time. There are many interesting phenomena which can be explained by the viscoelastic models such as the postseismic relaxation and the postglacial rebound (Stein and Wysession, 2003). To model the viscoelastic relaxation stimulated by the stress on elastic body, there are many models (Conry, 2004):

1. Maxwell Model

2. Kelvin Model
3. Standard Linear Solid Model
4. Burgers Model (Einarsson et al., 2010)

Those models all consist of:

1. **Spring**: store energy and make time *independent* respond to the stress.
2. **Dashpots/Dampers**: dissipate energy in the form of heat and make time *dependent* response to the stress.

In this thesis the Maxwell model is used. Fig. 3.18 is the mechanism of the Maxwell model.

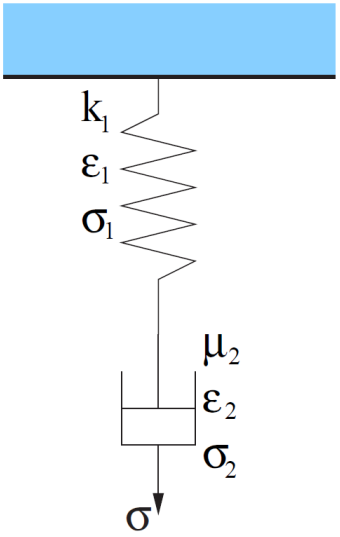

Figure 3.18: *Maxwell Viscoelastic Model*[a]

[a] where (Conry, 2004)

k_1	the linear spring constant (ratio of force and displacement, unit N/m)
μ_2	the linear dashpot constant (ratio of force and velocity, unit $\mathrm{N \cdot s/m}$)
ε_1 and ε_1	corresponding displacement of the spring and dashpot (unit m)
σ_1, σ_2 and σ	corresponding stress of the spring and dashpot and overall stress (unit N)

The relaxation time of the Maxwell model is explained in (Manias, 2011). We begin with the hypothesis that at time $t = 0$, a sudden deform to constant displacement ε_0 and according to *Hooke's Law of Spring*:

$$\sigma_1 = k_1 \varepsilon_1 \tag{3.72}$$

Meanwhile for the dashpot, according to *Newton's Law*:

$$\sigma_2 = \mu_2 \frac{\mathrm{d}\varepsilon_2}{\mathrm{d}t} \tag{3.73}$$

Because the spring and the dashpot are in series:

$$\sigma = \sigma_1 = \sigma_2 \tag{3.74}$$

and

$$\varepsilon_0 = \varepsilon_1 + \varepsilon_2 \tag{3.75}$$

from Eq. (3.72), (3.73), (3.74) and (3.75):

$$k_1 (\varepsilon_0 - \varepsilon_2) = \mu_2 \frac{\mathrm{d}\varepsilon_2}{\mathrm{d}t} \tag{3.76}$$

Eq. (3.76) is nothing but first order differential equation. By shifting items and integral on both side:

$$\frac{k_1}{\mu_2} t = -\ln (\varepsilon_0 - \varepsilon_2) + C \tag{3.77}$$

By the boundary condition, when $t = 0$ and $\varepsilon_2 = 0$, C equals $\ln \varepsilon_0$. Then

$$\frac{\varepsilon_0 - \varepsilon_2}{\varepsilon_0} = e^{-\frac{k_1}{\mu_2} t} \tag{3.78}$$

Combine Eq. (3.72), (3.74) and (3.78):

$$\sigma (t) = k_1 \varepsilon_0 e^{-\frac{k_1}{\mu_2} t} \tag{3.79}$$

Compare the Eq. (3.79) with (3.65). The unit of $y(t)$ is $\mathrm{m/s^2}$ which is the unit of the gravity. On the other hand the unit of σ is N which is $\mathrm{kg \cdot m/s^2}$. Then let $a_{18} = \frac{k_1 \varepsilon_0}{1\,\mathrm{kg}}$ and the *Maxwell viscoelastic relaxation time* is:

$$\tau = \frac{\mu_2}{k_1} \tag{3.80}$$

For the times less than τ the underground material can be considered as an elastic solid and for the time longer than τ it can be considered as a viscous fluid (Stein and Wysession, 2003). Meanwhile, τ is a parameter which indicates the elastic feature of an area different from the commonly used Love Number which is a global model.

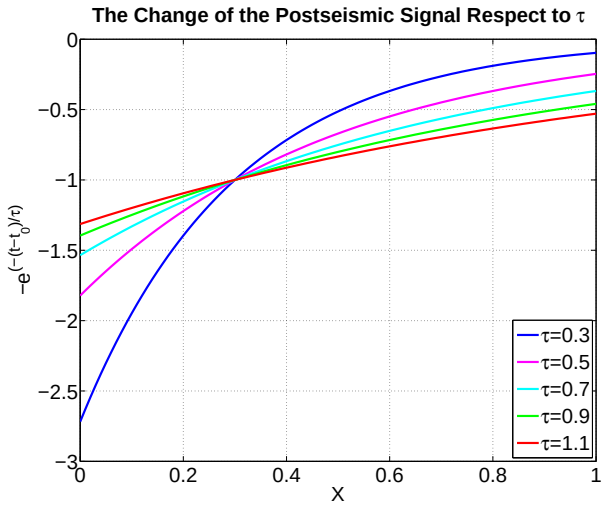

Figure 3.19: *The Change of the Postseismic Signal Respect to τ ($t_0 = 0.3$)*

From Fig. 3.19, the smaller τ is the faster the postseismic signal changes. The curves approaches x-axis but will never reach it.

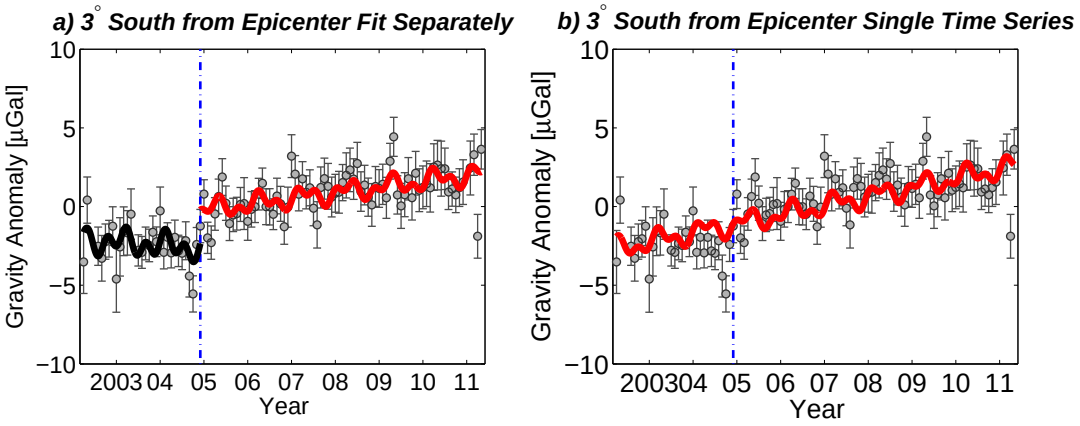

Figure 3.20: *Model the Earthquake Time Series (Sumatra)*

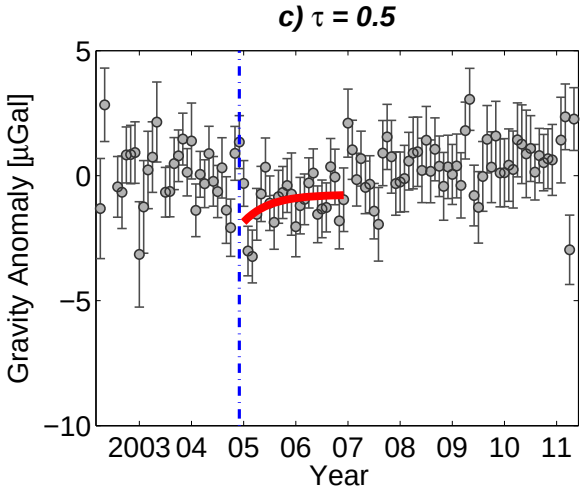

Figure 3.21: *Maxwell Relaxation Time τ (Sumatra)*

In the real GRACE data, the following figures are another point which is 3° north of the example points in Fig. 3.15, the behavior of τ is different in Fig. 3.16 and 3.21. It can be seen that the Fig. 3.16 is more "elastic solid" and Fig. 3.21 is more "viscous fluid".

3.8 Empirical Orthogonal Functions (EOF) Analysis

EOF is the abbreviation of the Empirical Orthogonal Function and the EOF method is equivalent to Principal Component Analysis (PCA). EOF technique aims at finding a new set of variables that represents most of the observed variances for the data through a linear combination of the original variables.

Suppose a map at time t_i for all the time from $i = 1, \cdots, n$ and it has q points:

$$\Psi = \begin{pmatrix} p_1(t_1) \\ p_1(t_2) \\ \vdots \\ p_1(t_n) \end{pmatrix} \mathbf{e}_1^T + \begin{pmatrix} p_2 \\ p_2 \\ \vdots \\ p_2 \end{pmatrix} \mathbf{e}_2^T \ldots + \begin{pmatrix} p_q \\ p_q \\ \vdots \\ p_q \end{pmatrix} \mathbf{e}_q^T \tag{3.81}$$

Using Singular Value Decomposition (SVD) to the matrix Ψ:

$$\Psi = Z\Sigma D^T \tag{3.82}$$

Z is the normalized eigenvector of $\Psi\Psi^T$ and D is the normalized eigenvector of $\Psi^T\Psi$, which indicates that $Z^TZ = I_t$ and $D^TD = I_q$, rearrange the Σ in the descending order $\sigma_1 > \sigma_2 \ldots > \sigma_{\min(q,t)}$, and the again the Ψ can be expressed:

$$\Psi = \begin{pmatrix} p_1' \\ p_1' \\ \vdots \\ p_1' \end{pmatrix} \mathbf{d}_1^T + \begin{pmatrix} p_2' \\ p_2' \\ \vdots \\ p_2' \end{pmatrix} \mathbf{d}_2^T \ldots + \begin{pmatrix} p_q' \\ p_q' \\ \vdots \\ p_q' \end{pmatrix} \mathbf{d}_{\min(q,t)}^T \tag{3.83}$$

Using SVD to the matrix Ψ: $\mathbf{d}_{\min(q,t)}^T$ is the ith column of matrix D^T and $P_i' = \Psi d_i$ which is called the *Principle Components (PC)*.

An EOF example can be seen in Appendix. B.

EOF analysis is widely used. The selection of the largest eigenvalues can reduce the noise of the signals and compress the volume of the storage and it can also find the axis of the largest direction of the covariance.

There are three conditions of EOF analysis of the earthquake signal (de Viron et al., 2008):

1. the best time for a jump is at less than three months from the "true time";
2. The Heaviside function, fitted on the observation, explains at least 20% of the variance of EOF time-series;
3. the synthetic and the retrieved patterns have a correlation coefficient larger than 0.5.

Meanwhile the last condition needs a priori information on the ground displacement, therefore it cannot be used this in the thesis.

Chapter 4

Data Analysis

4.1 Introduction

4.1.1 Earthquake Data

Theoretically the coseismic deformations of an earthquake with a seismic magnitude of $M_w = 7.5$ are expected to be detectable by GRACE (Sun and Okubo, 2004). But the depth of the hypocenter and the type of the earthquake should also be considered (Sun and Okubo, 2004). In this thesis, I tried to detect four earthquakes' signals from GRACE data combined with GLDAS model:

- Sumatra-Andaman Earthquake (Indonesia) 2004 ($M_w = 9.1$)
- Sichuan Earthquake (China) 2008 ($M_w = 7.9$)
- Maule Earthquake (Chile) 2010 ($M_w = 8.8$)
- Tōhoku Earthquake (Japan) 2011 ($M_w = 9.0$)

4.1.2 Datasets and Parameters

The datasets and parameters are listed in Table. 4.1.

Data	GRACE		CSR Release 4 (until May, 2011)
	C_{20}		JPL (Cheng and Tapley, 2004)
	GLDAS		JPL (Rodell et al., 2004)
Parameters	Eigenvalue		Gravity
	Grid		Block
	Block Size		$0.5^\circ \times 0.5^\circ$
	Filter	Gauss	350 km
		Fan	350 km
		Destriping	Degree: 8–60
			Order: 8–60
			Polynomial Degree: 2

Table 4.1: *Datasets and Parameters Description*

The error estimation of the field is done by combining the calibrated error with the C_{20} error by SLR. Since many papers (Heki and Matsuo, 2010*b*; Ozawa et al., 2011) used Fan filter 350 km, it is also used here. Furthermore, the destriping filter might remove the earthquake signals which are usually north to south stripes, so only some of the graphs used it in order to reduce the noise. Meanwhile the destriping filter is not used for the GLDAS but Gauss or Fan filter are applied in GLDAS same as GRACE.

4.2 Sumatra-Andaman Earthquake (Indonesia) 2004

4.2.1 The Geophysical Structure of the Sumatra Area

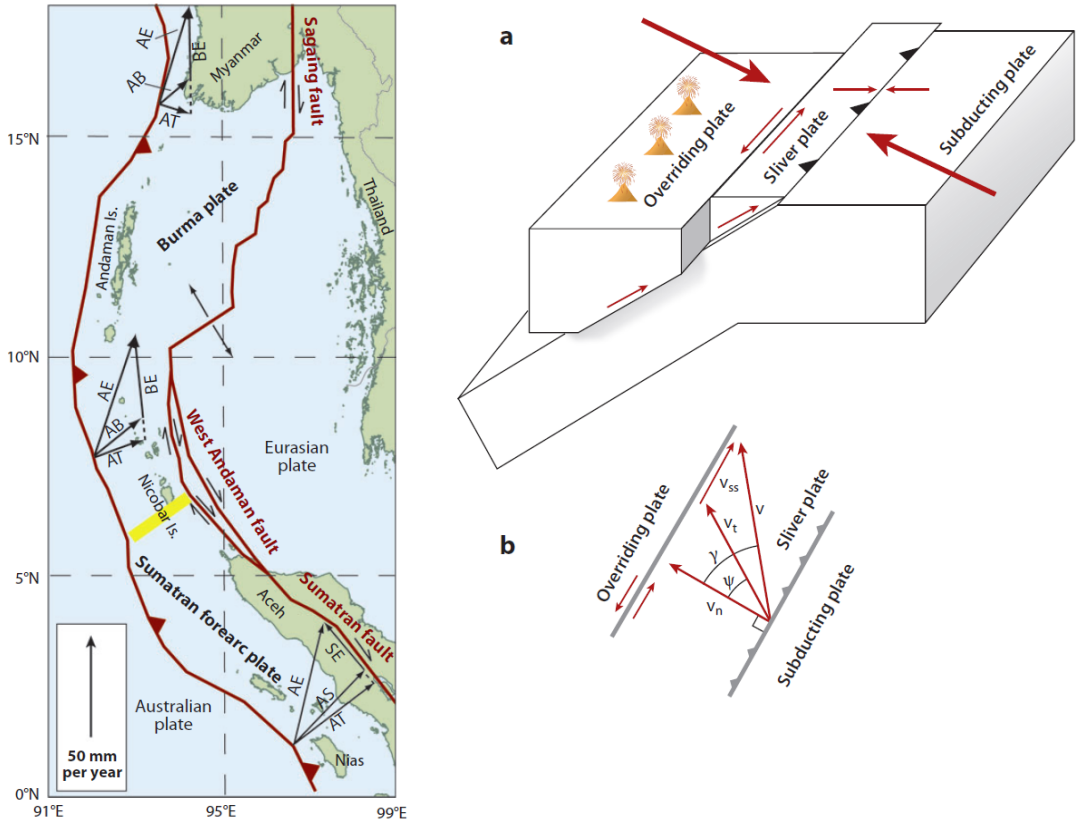

Figure 4.1: *Sumatra Area Structure (McCaffrey, 2009)*[a]

[a]where

AB: Australian-Burma motion;
AE: Australian-Eurasian motion;
AS: Australian-Sumatran forearc motion;
AT: Australian-Trench motion (component of convergence across subduction zone);
BE : Burma-Eurasian motion;
SE : Sumatran forearc-Eurasian motion

The Sumatra area has for a long time been a field laboratory for the studies of important geological processes. But compared to the subduction zones near developed countries like Japan and the United States, the Sumatra area has been paid little attention before the great earthquake and tsunami in 2004.

The simple structure of the Sumatra area is the interaction between the Indian-Australian and the Eurasian plates (see Fig. 4.1 left). However, the structure of this area in detail is much more complex. First, the Indian-Australian plate consists of two separated plates that are bounded by a board and it is currently being subducted at Sunda trench (DeMets et al., 1994) which is a long arc in the off shore area of Sumatra and Java island. Second, the existence of the sliver plate (see Fig. 4.1 right) which is the isolated wedge of forearc and leads to the related motion between plates is hard to be examined. It could happen that the coseismic and postseismic signal is quite far away from the epicenter due to the related motion spread by the small plates.

In 2004 the great Sumatra-Andaman Earthquake ($M_w = 9.1$) took place in such a region. According to the USGS's data: The epicenter is 3.316°N, 95.854°E and the depth is 30 km. The magnitude is 9.1 and it is the third largest earthquake in the world since 1900 and the largest since the 1964 Prince William Sound, Alaska earthquake.

There is another enormous earthquake the Nias earthquake three month later after Sumatra-Andaman Earthquake. Unfortunately, the Nias and the Sumatra-Andaman Earthquake signals cannot be reliably separated using only GRACE measurements (Einarsson et al., 2010). However, Panet et al. (2007) and Matsuo and Heki (2011) found such signal. In this thesis, I do not distinguish those two signals, so GRACE signals to be analyzed of Sumatra-Andaman Earthquake potentially contains two earthquakes' signals.

4.2.2 Time Series Analysis

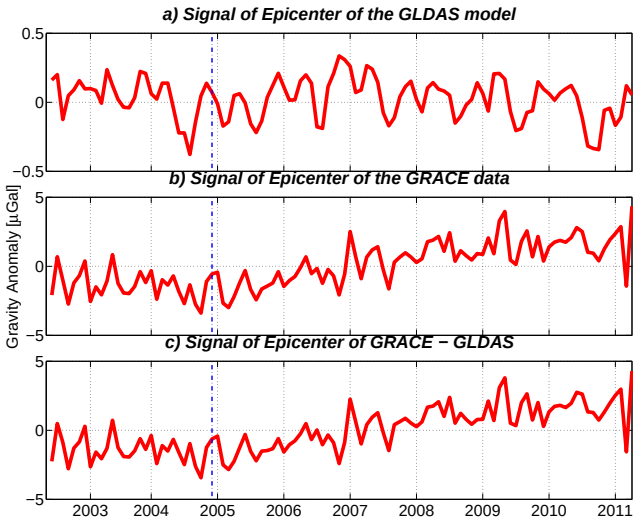

Figure 4.2: *Time Series in Epicenter (3°N, 96°E) of Sumatra-Andaman Earthquake (Indonesia) 2004 (Fan Filter 350 km)*

Fig. 4.2 shows GRACE and GLDAS model at the epicenter of Sumatra-Andaman Earthquake. There is no apparent jump in GRACE data whereas the signal begins to steadily increase after

the earthquake. In contrast, there is no such phenomenon in GLDAS model which is quite periodic. Meanwhile GLDAS model is not necessary because the epicenter is in the sea not on land since GLDAS model is only valid on land. The reason for GLDAS model in the figure is the data leakage effect and such effect is also demonstrated in Fig. 3.12. Furthermore, the scale of GLDAS model is 1/10 of GRACE data. As a result that GRACE data subtracted GLDAS model does not change so much compared to the original GRACE signal .

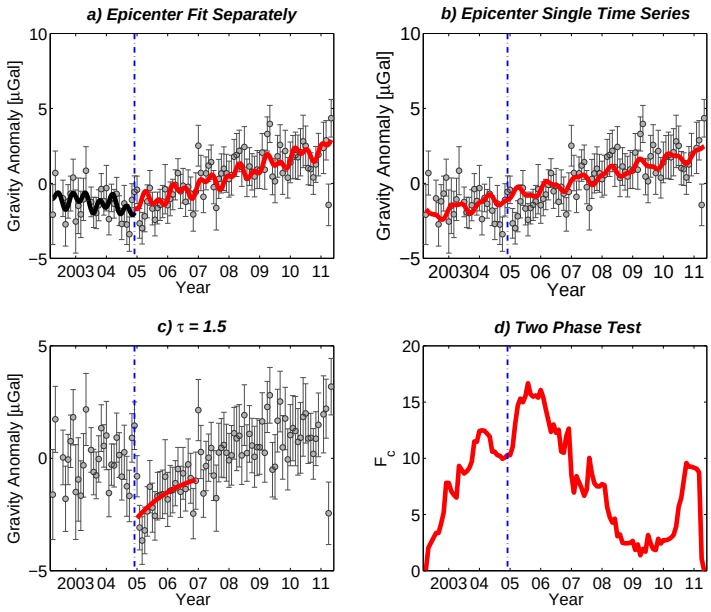

Figure 4.3: *Fit and Changepoint Detection of Time Series in Epicenter* (3°N, 96°E) *of Sumatra-Andaman Earthquake (GRACE Fan Filter* 350 km*)*

The time series of GRACE data in Fig. 4.3(a) is modeled by applying the method introduced in Sec. 3.7 to each point of the selected field. In Fig. 4.3(a), it can be clearly seen that the trend of the gravity changes is decreased before Dec. 2004. In comparison, after the earthquake the trend begins to increase. Obviously in Fig. 4.3(b) the overall fit is not suitable for the dataset.

After subtracting the annual and S_2 waves from GRACE data, the postseismic signals can be more easily discovered by fitting the data with the function $1 - e^{-\frac{t}{\tau}}$ which indicates the speed of the postseismic change. τ equals 1.5 according to two years data at the point of the epicenter. The function of the postseismic fitting is a nonlinear equation (Eq. (3.65)) with the term $e^{-\frac{t-t_0}{\tau}}$. Thus, the solution is much unstable if τ is treated as a parameter to be estimated. Fix $\tau = 0.6$ will stabilize the solution and 0.6 is an empirical number that can best fit the results everywhere (Ogawa and Heki, 2007). Considering the instability of the estimation of τ, only limited points near the epicenter are modeled using the Maxwell relaxation model.

The peaks of Two Phase test of the signal in the epicenter do not occur when the earthquake took place but it is around the May. 2005. Analyze the signal shown in Fig. 4.3(a) in a mathematical way that if the change point of the fitting from Dec. 2004 to around May. 2005, the fitting will be better as that the black wave can go further. Although this fit can be better, there

is no geophysical meaning in it and the Two Phase test is not suitable for such data.

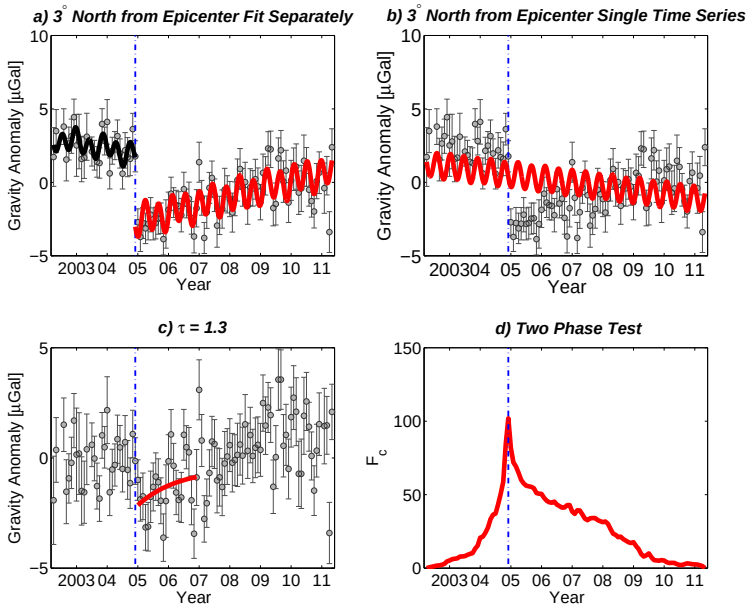

Figure 4.4: *Fit and Changepoint Detection of Time Series in* 3° *North of Epicenter* (3°N, 96°E) *of Sumatra-Andaman Earthquake (GRACE Fan Filter* 350 km*)*

Fig. 4.4 is the time series at point 6°N, 96°E. Unlike the signal in Fig. 4.3, the rupture of the signal can be directly seen even without the modeling. The jump is about 6–7 μGal in this point. For the Gauss filter's results in Fig. 4.5, the rupture is about 10 μGal. So the filter can strongly affect the specific value of the rupture. Meanwhile postseismic changes are similar to that in the epicenter. The postseismic recovery is 1.3 about the same of that at the epicenter. The result for the Gauss filter is also different from Fan filter which is 1.2. For the Two Phase change point test, it performs very well at point (6°N, 96°E). There is only one peak in the data and it is the time of earthquake.

4.2.3 Rupture Detection

By applying the Two Phase test, Fig 4.6(a) illustrates the significant jump in the area along northwest direction of the epicenter and the Andaman Sea. This is one of the two earthquakes that the test can detect exactly the earthquakes rupture both in the time and spatial domain (compare with Fig. 4.21 and 4.52). The related condition for the detection of the rupture is the best among all the four earthquakes to be analyzed. Sichuan Earthquake is relatively small and the hydrological signal is too strong for the time series analysis. Maule Earthquake is near the Amazon area where the hydrological effect cannot be completely neglected. Tōhoku Earthquake is similar to Sumatra-Andaman Earthquake but at present there is not enough data for such analysis.

The detection of the rupture by the Ratio test is successful in Sumatra-Andaman Earthquake and the coseismic rupture can be clearly seen in both the Andaman Sea and the area near

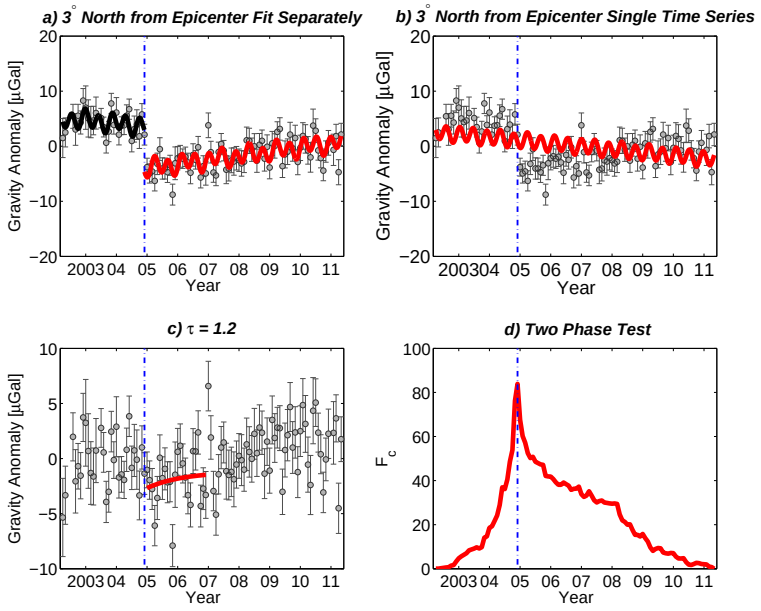

Figure 4.5: *Fit and Changepoint Detection of Time Series in* 3° *North of Epicenter* (3°N, 96°E) *of Sumatra-Andaman Earthquake (GRACE Gauss Filter* 350 km*)*

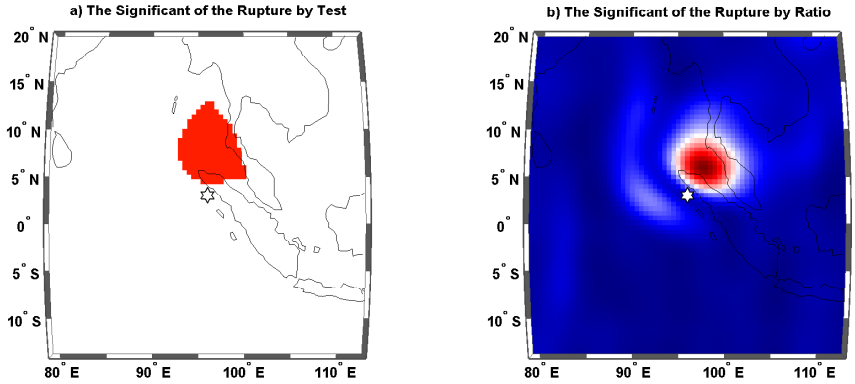

Figure 4.6: *Detection of the Rupture by Test of Sumatra-Andaman Earthquake (Indonesia) 2004 (GRACE Fan Filter* 350 km*)*

the Sunda Trench. So the coseismic signals from both sides of the epicenter can be seen in Fig. 4.6. In addition the peak of the signal is in the Andaman sea. The hydrological signal in the Indochinese peninsula does not affect such detection of the rupture. To summarize, the Sumatra-Andaman Earthquake is both significant in the time and spatial domain of GRACE signals.

4.2.4 Least Squares Adjustment

By the method of the least squares adjustment, the coseismic rupture is also visible similar to the Fig. 4.5 and the estimated maximum jump is more than 6 μGal for the Fan filter and more

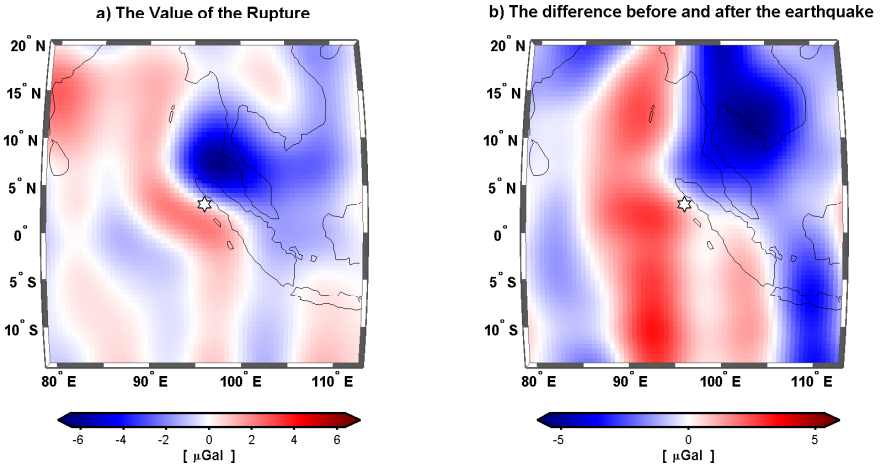

Figure 4.7: *Rupture and Gravity Field Before and After Sumatra-Andaman Earthquake (Indonesia) 2004 (GRACE Fan Filter* 350 km*)*

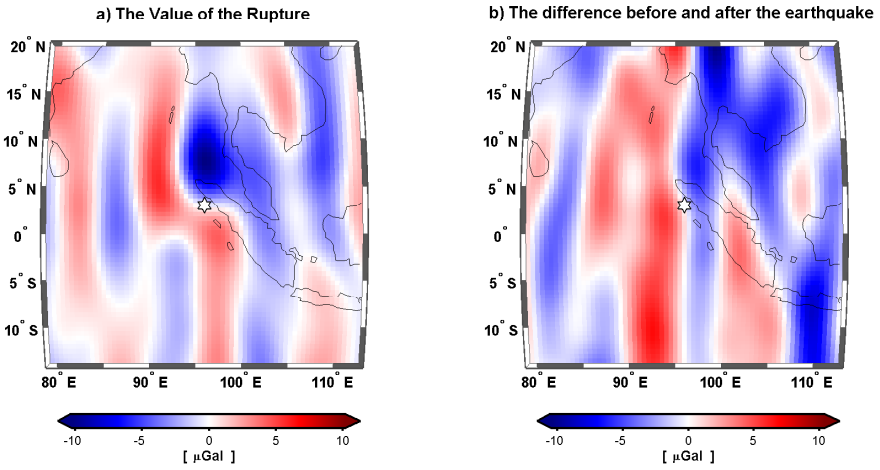

Figure 4.8: *Rupture and Gravity Field Before and After Sumatra-Andaman Earthquake (Indonesia) 2004 (GRACE Fan Filter* 350 km*)*

than 10 μGal for the Gauss filter (See Fig. 4.8). Similar result was found in (de Linage et al., 2009; Han et al., 2006) in Fig. 4.9. The coseismic signal is approximately 10 μGal for the CSR release 4 data.

The hydrological effect can be also seen in the Fig. 4.10. Compared to the Fig. 4.7 which is the difference of the months before and after the earthquake, the signal is very strong in the Indochinese peninsula. It is the hydrological change caused by the climate. Thus such hydrological signal only affects the signal in the Indochinese peninsula and in Fig. 4.7(a) the signal in the Andaman Sea area is the same signal as which has been reported in Han et al. (2006); Ogawa and Heki (2007); Chen et al. (2007); Han et al. (2008); de Linage et al. (2009); Panet et al. (2010).

(a) Result from de Linage et al. (2009) (b) Result from Han et al. (2006)

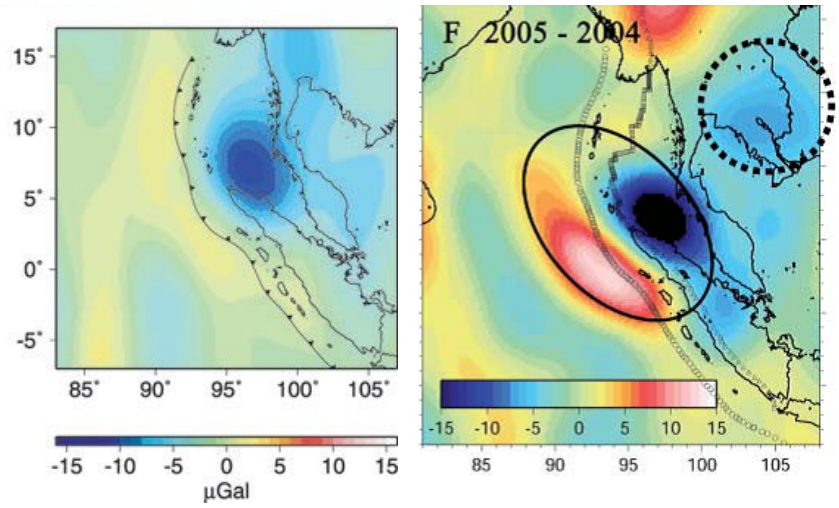

Figure 4.9: *Comparison of Gravity Change Results of of Sumatra-Andaman Earthquake (Indonesia) 2004*

The coseismic rupture in the Andaman Sea area is due to the crustal dilatation caused by the sea floor crust expansion (Han et al., 2006). But de Linage et al. (2009) interpreted the signal to be the ocean mass lateral redistribution.

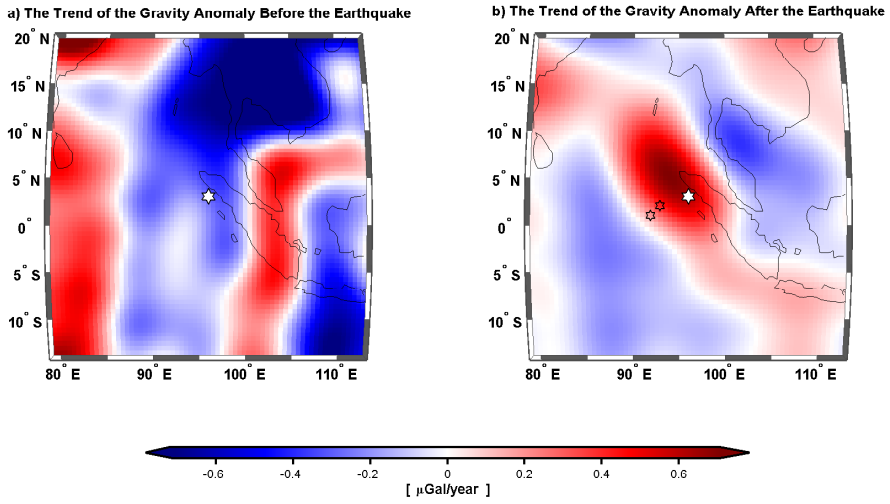

Figure 4.10: *Gravity Trend Before and After Sumatra-Andaman Earthquake (Indonesia) 2004 (GRACE Fan Filter* 350 km*)*

The trend before and after the earthquake are quite different. Before the earthquake the trend is only the decreasing of gravity in the Andaman Sea and the Indochinese peninsula. However the postseismic signal is very strong and should be carefully dealt with. This signal has been discussed by several scientists. Ogawa and Heki (2007) interpreted it by the theory of the mantle water diffusion. According to Jónsson et al. (2003), the pore fluid diffusion causes post-

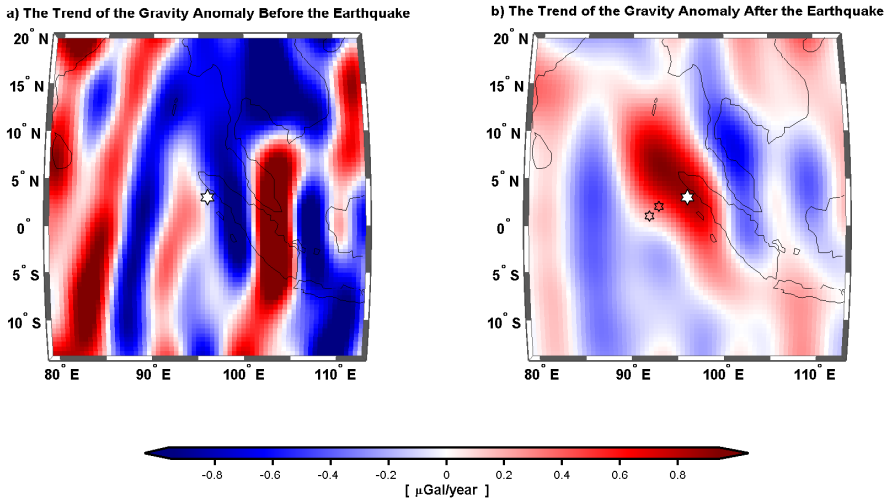

Figure 4.11: *Gravity Trend Before and After Sumatra-Andaman Earthquake (Indonesia) 2004 (GRACE Gauss Filter* 350 km*)*

seismic changes opposite to coseismic changes with relatively short timescales. In the case of Sumatra-Andaman Earthquake the supercritical water abundantly exists in subduction zones. The mantle water will stop to flow when the new hydrostatic equilibrium is reached. But see from Fig. 4.3 there are no traces of the slowing down of the signal during such a long time scale of seven years (see Fig. 4.3(a)). At the same time the viscoelastic relaxation is very important to explain the signal but cannot explain all the gravity variations. Panet et al. (2010) modeled the postseismic signal by a viscoelastic relaxation with a lower upper mantle viscosity, to which after slip at the downdip continuation of the ruptured surface is added. But all those hypotheses need to be checked by the longer time of GRACE data.

Some geologist also examined the Sumatra-Andaman area not by the common means of geodesy but by the corals. Fig. 4.12 gives some other geology hypothesis. The coral from the offshore area can record the sea level changes during hundreds of years because of the special property of the coral growth. By observing the coral rings, expert finds the earthquake supercycles in the West Sumatra area and predicts that the Mentawai patch which is about 5° southwest of the epicenter of Sumatra-Andaman Earthquake will rupture soon (Sieh et al., 2008).

Although the postseismic signal is a little far from the area which is predicted to rupture, it can still consider to be a relative event. But the reason for steadily increase signal of Fig. 4.3 is still unknown and the supercycle theory is still under debate as well. One opinion is that the large ruptures on faults can be very infrequent such as Sichuan Earthquake (China) 2008 which has approximately 3000 years recurrence interval (Wiseman et al., 2011). However, it is fortunate that the supercycle might just begin and would last some decades. Finally it could be proved or rejected by time:

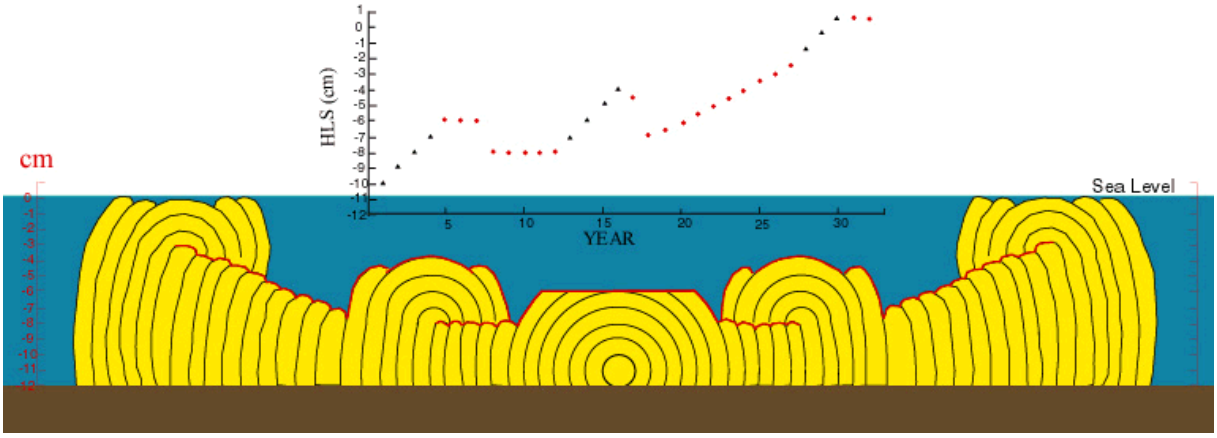

Figure 4.12: *The Sumatra Coral from Caltech's Research. (http://www.tectonics.caltech.edu/sumatra/corals.html)*

> Nonetheless, to those living in harm's way on the coasts of western Sumatra, it should be useful to know that the next great earthquake and tsunami are likely to occur within the next few decades, well within the lifetimes of children and young adults living there now (Sieh et al., 2008).

The small stars in Fig. 4.10(b) is the two earthquakes epicenters (0.773°N, 92.452°E, depth 16.4 km with $M_w = 8.2$ and 2.311°N, 93.063°E, depth 22.9 km with $M_w = 8.6$ from: USGS) on Apr. 11, 2012. It is not known yet if those two earthquakes are relevant to the postseismic process of Sumatra-Andaman Earthquake (Indonesia) 2004.

Eight fields in Fig. 4.13 are showing the annual and S_2 waves of the Sumatra area. The annual signals are mainly in the areas of the Indochinese peninsula. However, the S_2 signals are both in the ocean and land. The S_2 signals in the north of epicenter become more concentrated after the earthquake.

4.2.5 Empirical Orthogonal Functions (EOF) Analysis

See from Fig. 4.14, in the mode 1 of EOF analysis which is the largest component of all the PCs, annual hydrological data of the area cannot be seen from the PC. It shows clearly the earthquake rupture process. Meanwhile the field result shows earthquake signal clearly as well. The maximum value is 2.38 μGal. The white area between the red and blue peak is where the Sunda Trench is. The mode 1 clearly demonstrates the coseismic signal of the earthquake.

Mode 2 accounts for 12.4% of the total changes. The result is interesting. The PCs shows a sharp drop down in Oct. 2004. According to de Viron et al. (2008), the earthquake signal is still obvious in PC of mode 2.

For EOF mode 3 – 5, the earthquake signal is not so significant as that of the mode 1 and 2.

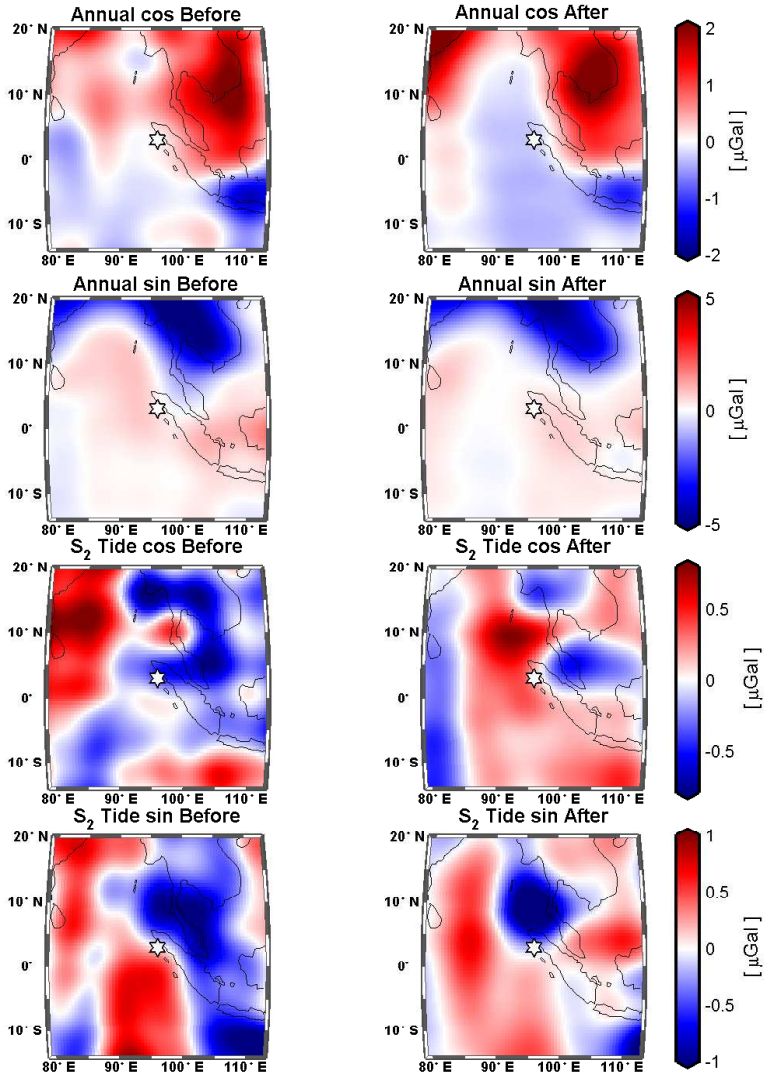

Figure 4.13: *Annual and* S_2 *Tide Waves Before and After Sumatra-Andaman Earthquake (Indonesia) 2004 (GRACE Fan Filter* 350 km*)*

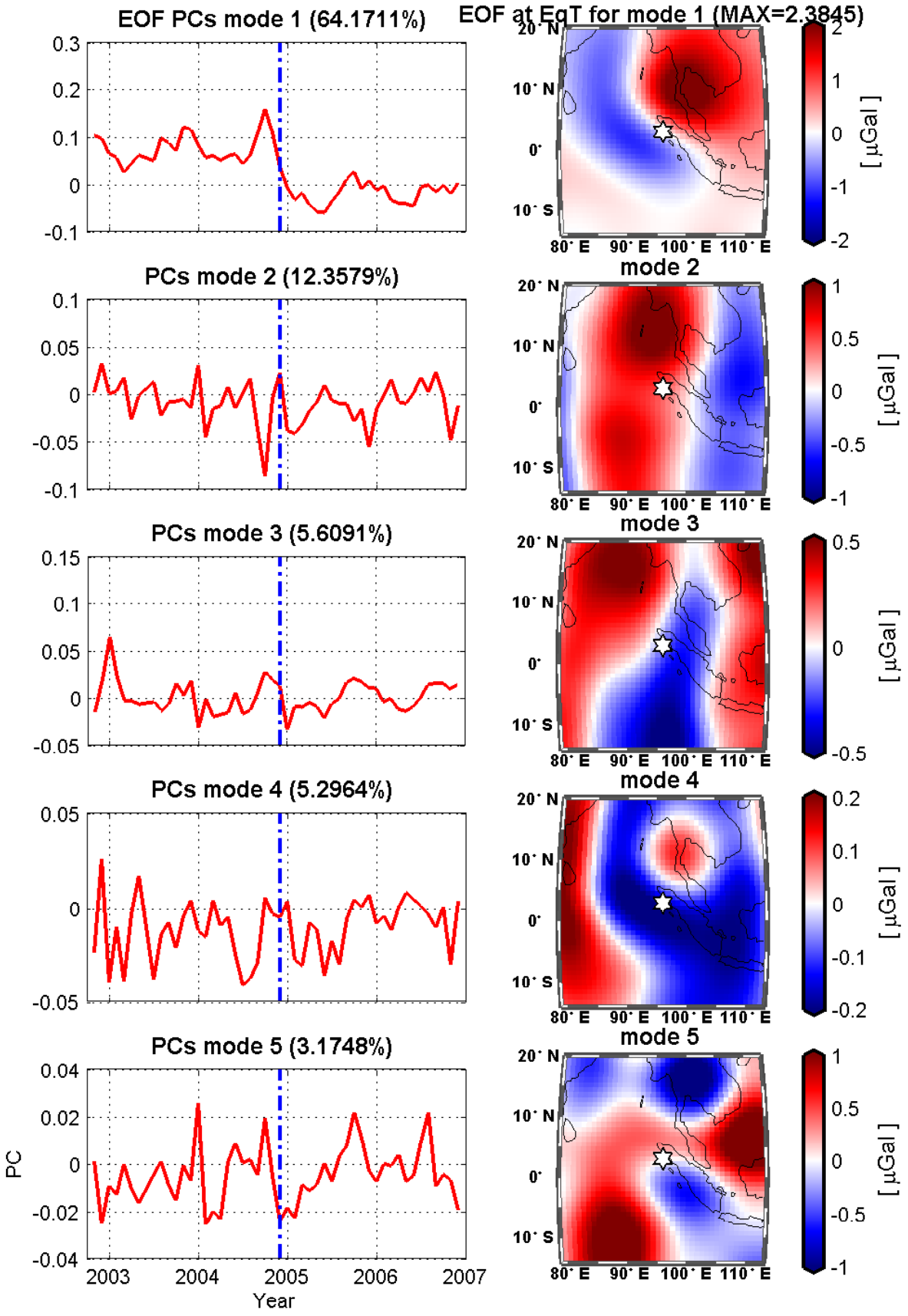

Figure 4.14: *EOF Analysis of Sumatra-Andaman Earthquake (Indonesia) 2004 (GRACE Fan Filter* 350 km*)*

4.3 Sichuan Earthquake (China) 2008

4.3.1 The Geophysical Structure of the Sichuan Area

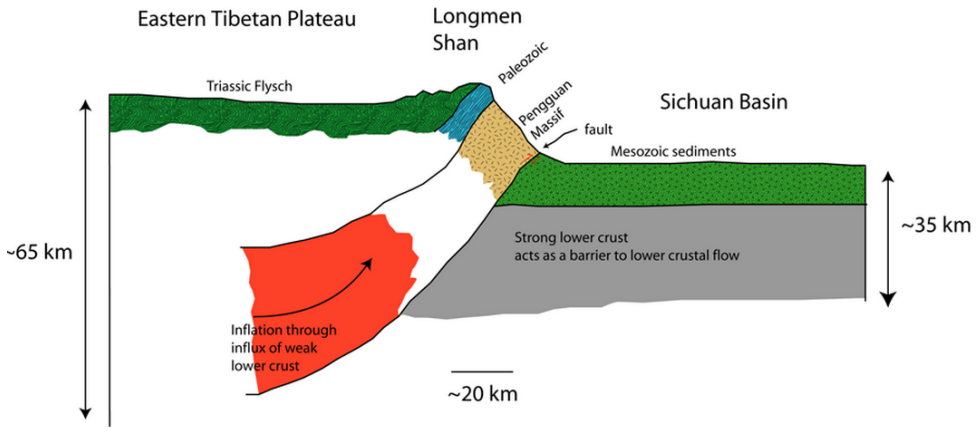

Figure 4.15: *Longmen Shan Area Structure (MIT, n.d.)*

The Sichuan (also Wenchuan) Earthquake ($M_w = 7.9$) on the west edge of the Sichuan Basin struck one of the most densely populated regions in China on May. 12, 2008 with the epicenter at $(30.986°\text{N}, 103.364°\text{E})$ and 19 km deep (from: USGS). No doubt that it is the largest earthquake in western China.

The earthquake occurred in an area where the Indian plate and the Eurasian plate collide and this process has been going on for 50 Ma. In detail, the Guanxian-Beichuan-Wenchuan faults system structures the Longmen Shan belt which is the east wedge of the Tibetan plateau moving towards the stable Yangtze craton (Robert et al., 2010). The Longmen Shan main fault, which is 308 km × 40 km, is divided into 110 sub-faults with the cell size of 14 km × 8 km. The front Longmen Shan fault about the size of 84 km × 32 km consists of 24 sub-faults of 14 km × 8 km each (Wang et al., 2010).

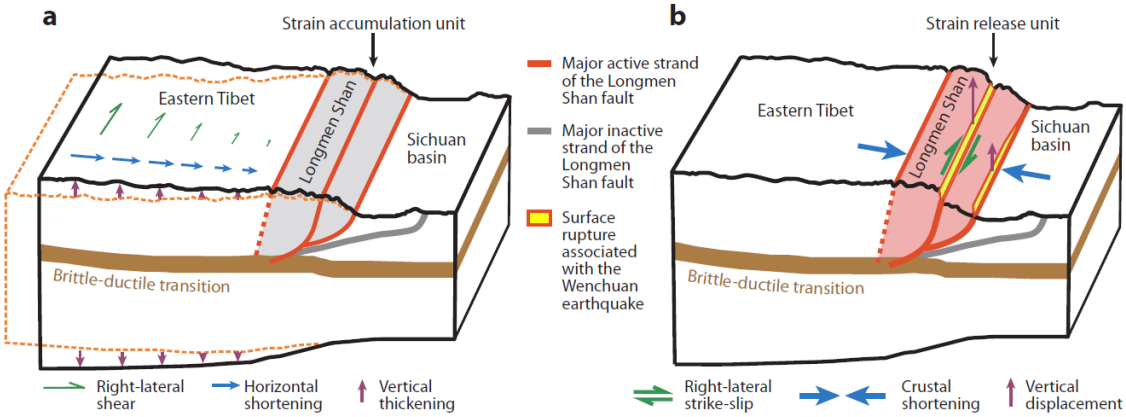

Figure 4.16: *Movement of the Faults in Longmen Shan (Zhang et al., 2010)*

Fig. 4.16 shows the relative movements of the faults before and during Sichuan Earthquake. Since the late Mesozooic the Sichuan basin has been locked and behaved very stably. The energy accumulation of the postseismic process includes the shortening, wrenching and uplifting of the eastern Tibet while the Longmen Shan fault was locked. The coseismic process (see Fig. 4.16(b) is a complex movement with the right-lateral strike-slip, crustal shortening and the vertical displacement (Zhang et al., 2010). The estimated maximum slip on the fault can reach up to 12.5 m. Theoretically GRACE can detect a seismic magnitude of $M_w = 7.5$. By applying the same filter as Han et al. (2006), Sun calculated the respectively gravity changes of Sichuan Earthquake that is about -1.6–$+3.2$ μGal for 100 km Gauss filter and -0.12–$+0.24$ μGal for 300 km Gauss filter (Wang et al., 2010). Considering the hydrological effect and GRACE errors, it is difficult to detect such small signal. Nevertheless I choose to make a try in this thesis.

4.3.2 Time Series Analysis

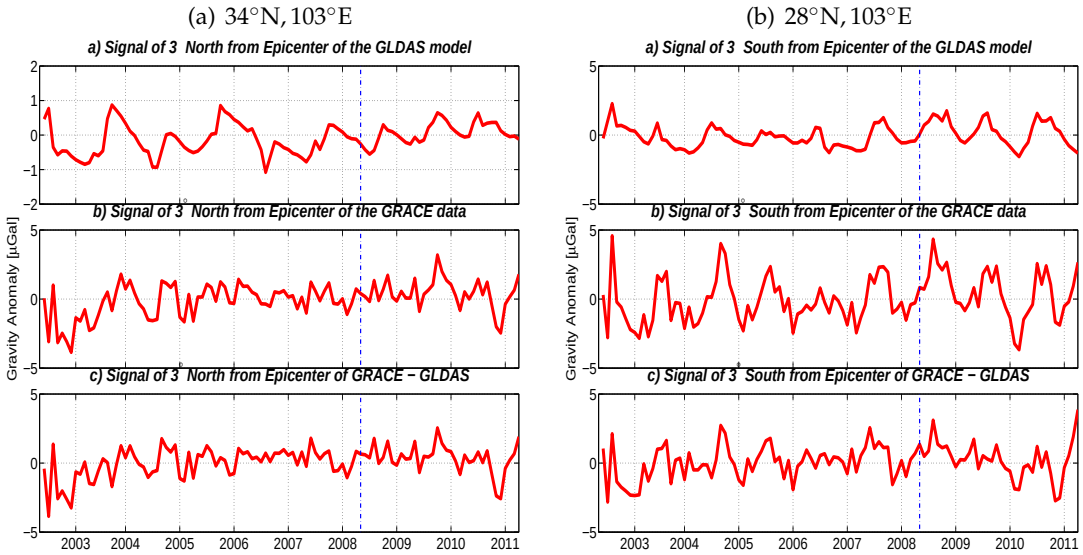

Figure 4.17: *Time Series in* 3° *North and South of the Epicenter* (31°N, 103°E) *of Sichuan Earthquake (China) 2008 (Fan Filter* 350 km*)*

The time series of the point 3° north of epicenter show the very small but periodic hydrology signal from GLDAS. GRACE data is about -3–3 μGal and GLDAS is about -1–1 μGal. It is reasonable because in the northern part of the earthquake area is the Loess Plateau where it is very dry. And GRACE data contains a lot of hydrology signals. After subtracting GLDAS model from GRACE data, Fig. 4.17 left (c) does not show obvious change. However, the earthquake jump is not visible there.

In contrast, the hydrological signal is much stronger at the point 3° south of epicenter. The magnitude is -2–2 μGal which is two times as big as the north one. Contrary to the situation in the north, the southern part of the Epicenter is the Yunnan-Guizhou Plateau where it is very moist. And the elimination of the hydrology signal is not so satisfactory that after subtracting GLDAS model, the remaining GRACE signal is still periodic.

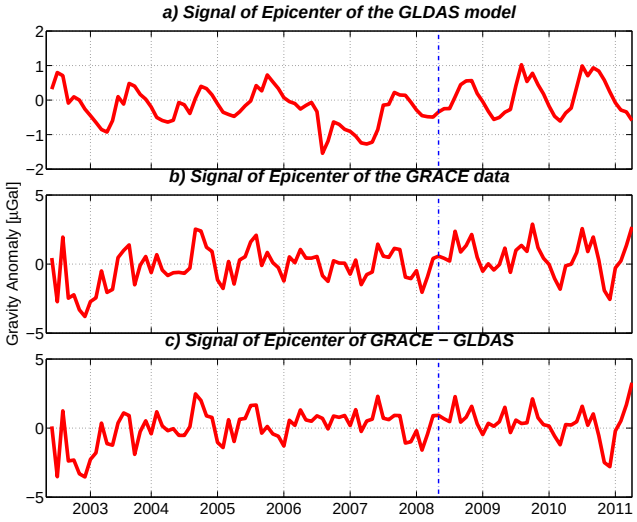

Figure 4.18: *Time Series in Epicenter* (31°N, 103°E) *of Sichuan Earthquake (China) 2008 (Fan Filter* 350 km*)*

The magnitude of the time series of the epicenter is just between the two points mentioned. GRACE data is about −4–4 μGal similar to that in the south and GLDAS model is about −1–1 μGal similar to that in the north. Geographically the epicenter is in the middle of those points. Again, no jump is visible in time series. But in GLDAS, there is a significant change in the year of 2007 due to unknown reason.

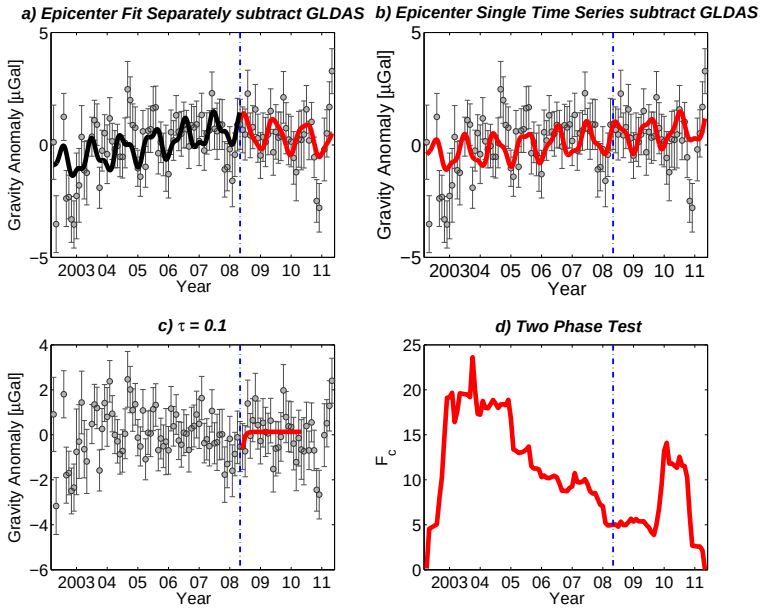

Figure 4.19: *Fit and Changepoint Detection of Time Series in Epicenter* (31°N, 103°E) *of Sichuan Earthquake (China) 2008 (GRACE-GLDAS Fan Filter* 350 km*)*

Comparing the two figures of fitting in Fig. 4.19, the separate fitting is not significantly better which is proved by (d). But the estimation of τ is still done and the value is invalid. Fig. 4.19(d) shows that the Two Phase test fails here.

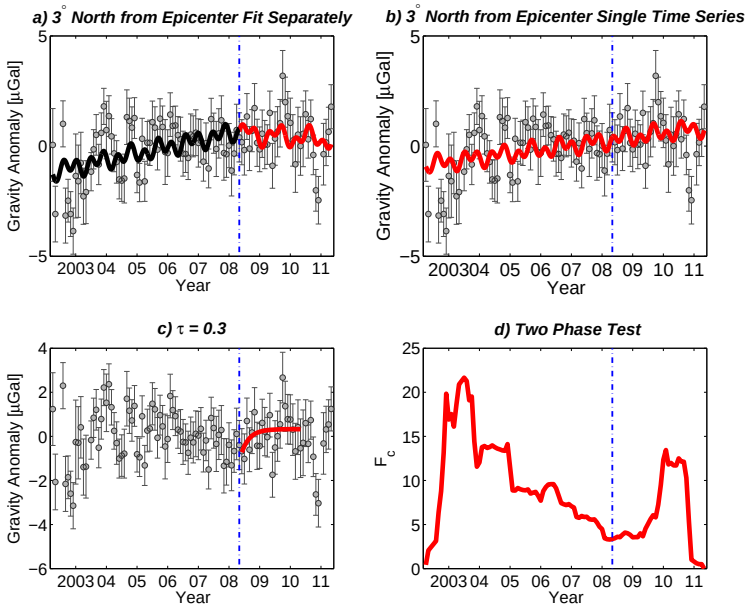

Figure 4.20: *Fit and Changepoint Detection of Time Series in 3° North of the Epicenter (31°N, 103°E) of Sichuan Earthquake (China) 2008 (GRACE Fan Filter 350 km)*

In the Fig. 4.20, it shows the point 3° north from the epicenter of GRACE only field. The overall fit is not better than fit separately and in the time around Jan. 2011, there is a significant drop in GRACE signal and the reason is unknown.

4.3.3 Rupture Detection

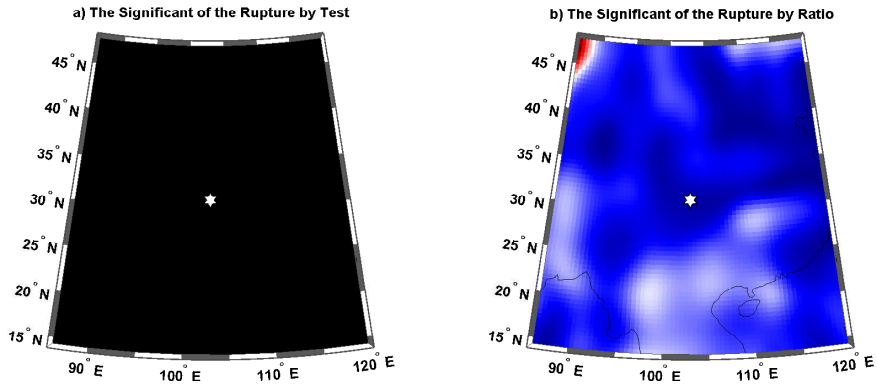

Figure 4.21: *Detection of the Rupture by Test of Sichuan Earthquake (China) 2008 (GRACE Fan Filter 350 km)*

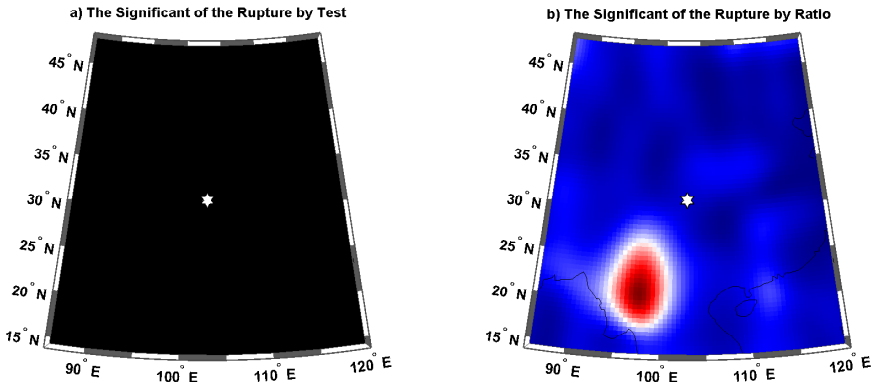

Figure 4.22: *Detection of the Rupture by Test of Sichuan Earthquake (China) 2008 (GRACE-GLDAS Fan Filter* 350 km*)*

Fig. 4.21 is the analysis of GRACE data. The Two Phase test cannot detect the rupture in Sichuan Earthquake (China) 2008 and the results of the Ratio test as well. The main reasons for the failure of those two methods are firstly that compared to the earthquake signal the hydrological signal is relatively strong, secondly that the earthquake signal is too weak.

The elimination of the hydrological signals is done and analyzed in Fig. 4.22. Still the Two Phase test fails (the black color means not a single point has significant jump when the earthquake took place). Yet the Ratio test draws a very interesting graph showing the rupture in the southwest direction of the epicenter. Seismologically the signal covers another place of the earthquakes: Burma. Burma is located east of India, where it is roughly along the northern extension of the Andaman arc. The motion of the Indian and Eurasian plates is about 5 cm/year and the tectonics and seismic activity occurs over a broad zone hundred kilometers wide (Frohlich, 2006). Since there is no large earthquake in this area in 2008, the signal should be caused by the hydrological signal as seen in Fig. 4.18. Such signal could be due to the hydrological change in Burma area or that GLDAS model does not model the Burma area very well.

GLDAS model shows the same change in the Fig. 4.23 and 4.24, so this is not the earthquake signal but the hydrological signal.

The signal in the Indochinese peninsula appears in both subfigures of Fig. 4.25. Comparing magnitudes of the Fig. 4.25(a) and Fig. 4.26(a), GLDAS model can eliminate the hydrological signal significantly in the north area and in the south area the peak moves to the northwest after getting rid of GLDAS model. Similar phenomenon appears in Fig. 4.25(b) and Fig. 4.26(b).

4.3.4 Least Squares Adjustment

In Fig. 4.27 and 4.28, the same pattern to the southwest direction of epicenter (see Fig. 4.26) appears in the trend after the earthquake, which is due to hydrology. There are no significant changes before the earthquake whether to subtract GLDAS model or not.

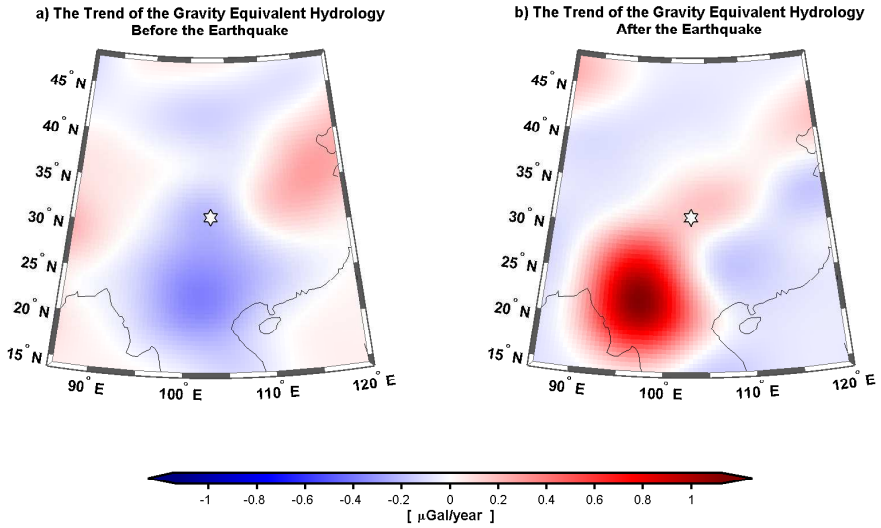

Figure 4.23: *Gravity Equivalent Hydrology Trend Before and After Sichuan Earthquake (China) 2008 (GLDAS Gauss Filter* 350 km*)*

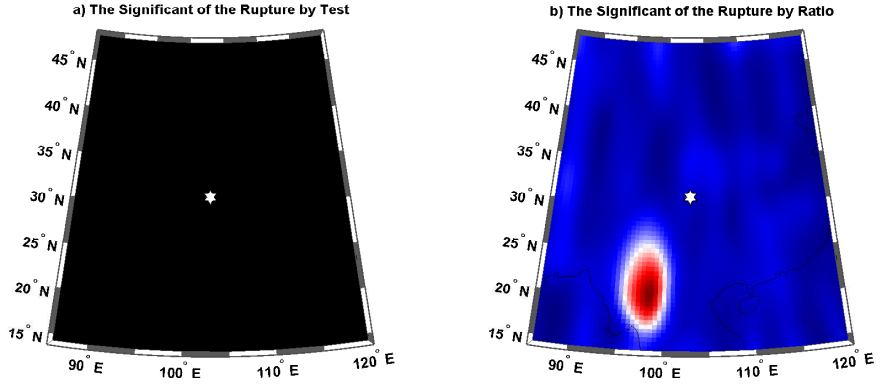

Figure 4.24: *Detection of the Rupture by Test of Sichuan Earthquake (China) 2008 (GLDAS Gauss Filter* 350 km*)*

In Fig. 4.29, the coefficients of the annual and S_2 waves indicate strong hydrological signal in the southwest of the epicenter. Compared to Fig. 4.30, the magnitudes of the annual and S_2 signals decrease after subtracting GLDAS model, which shows the effect of the elimination.

4.3.5 Empirical Orthogonal Functions (EOF) Analysis

EOF analysis is done by using both GRACE data only and GRACE data subtracted GLDAS model. Fig. 4.31 shows EOF analysis using only GRACE data. In mode 1, the PC is obviously the annual change and the field of the mode 1 is the hydrological distribution in that area. In the north, the hydrological signal is very small and in the south it is very strong. The mode 2

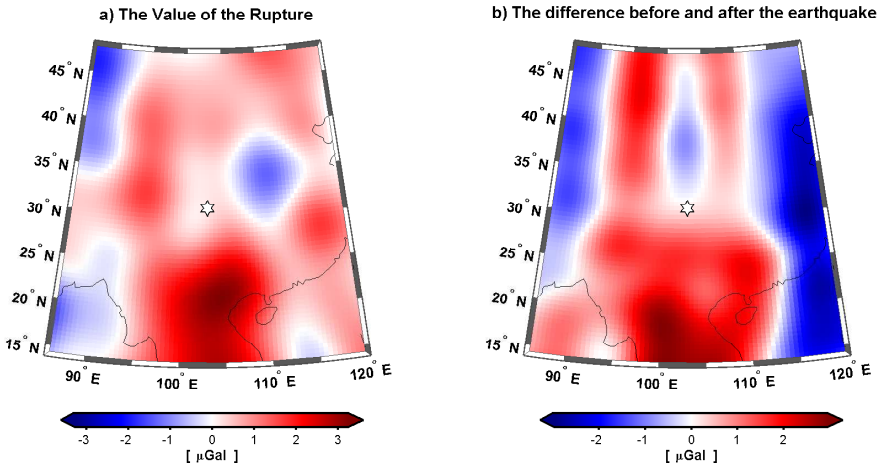

Figure 4.25: *Rupture and Gravity Field Before and After Sichuan Earthquake (China) 2008 (GRACE Fan Filter* 350 km*)*

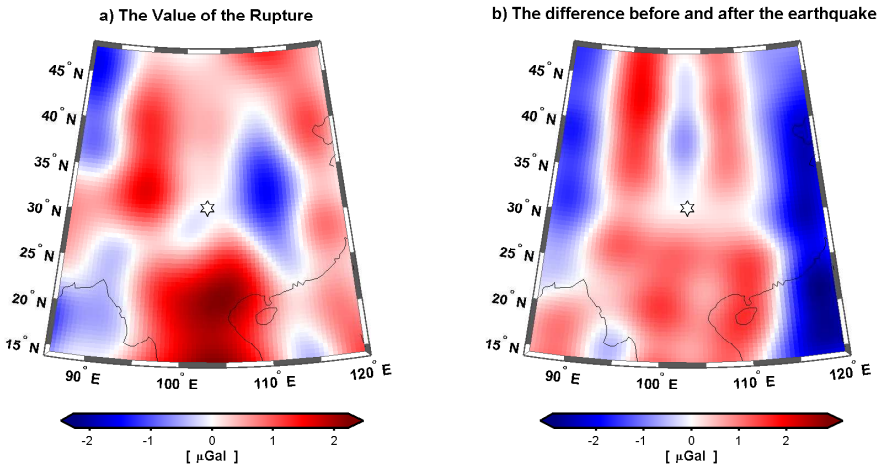

Figure 4.26: *Rupture and Gravity Field Before and After Sichuan Earthquake (China) 2008 (GRACE-GLDAS Fan Filter* 350 km*)*

PC is not quite periodic. But with a peak at the time when the earthquake took place. And in the EOF, the field is divided into two parts. Whether this signal is caused by the earthquake needs further proof. The PCs in mode 3 – 5 are periodic and there are no obvious earthquake pattern as well.

Fig. 4.32 shows EOF analysis of GRACE data subtracted GLDAS model. The mode 1 is much different from the mode 1 in Fig. 4.31, the hydrological effect is not so strong in the EOF field. And the PC in mode 2 in Fig. 4.32 shows the similar pattern as Fig. 4.31. But the PC slightly changed. The reason again might be the earthquake. From mode 3 - 5 the PCs are quite annual. But the EOF field in mode 4 shows some interesting results although it is annual signal indicated by the PC.

After all, whether the suspicious signal is earthquake signal or not needs further proof.

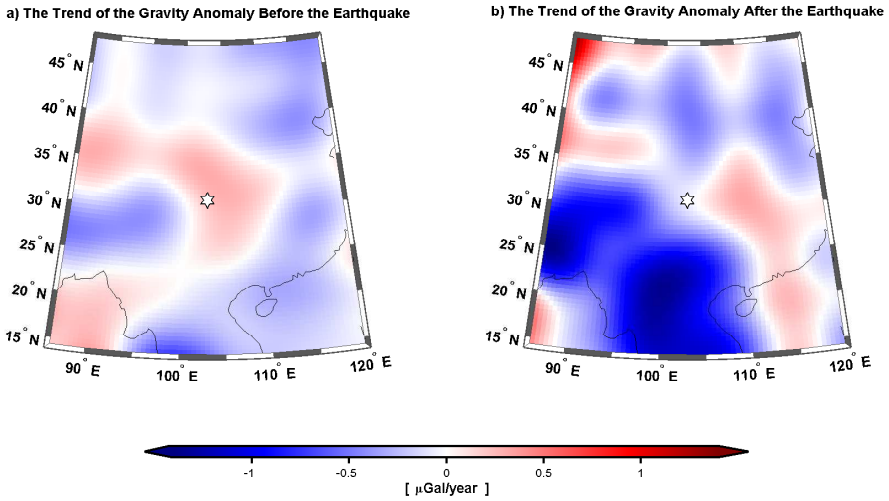

Figure 4.27: *Gravity Trend Before and After Sichuan Earthquake (China) 2008 (GRACE Fan Filter* 350 km*)*

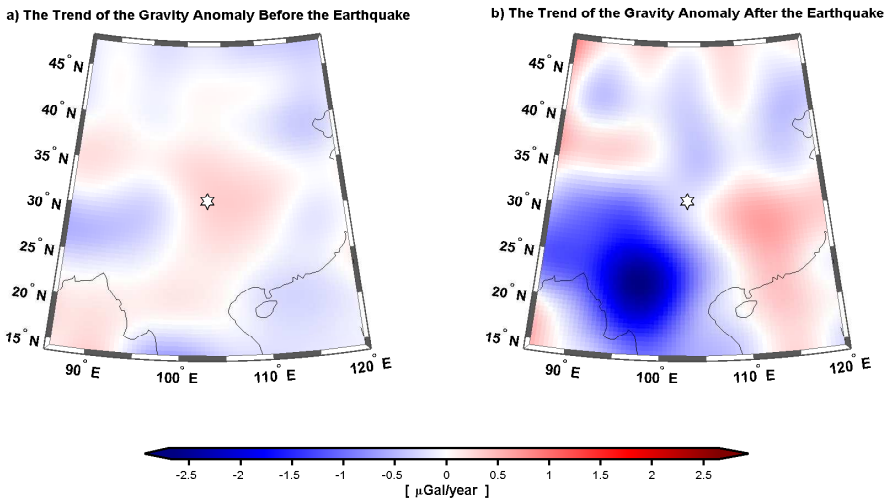

Figure 4.28: *Gravity Trend Before and After Sichuan Earthquake (China) 2008 (GRACE-GLDAS Fan Filter* 350 km*)*

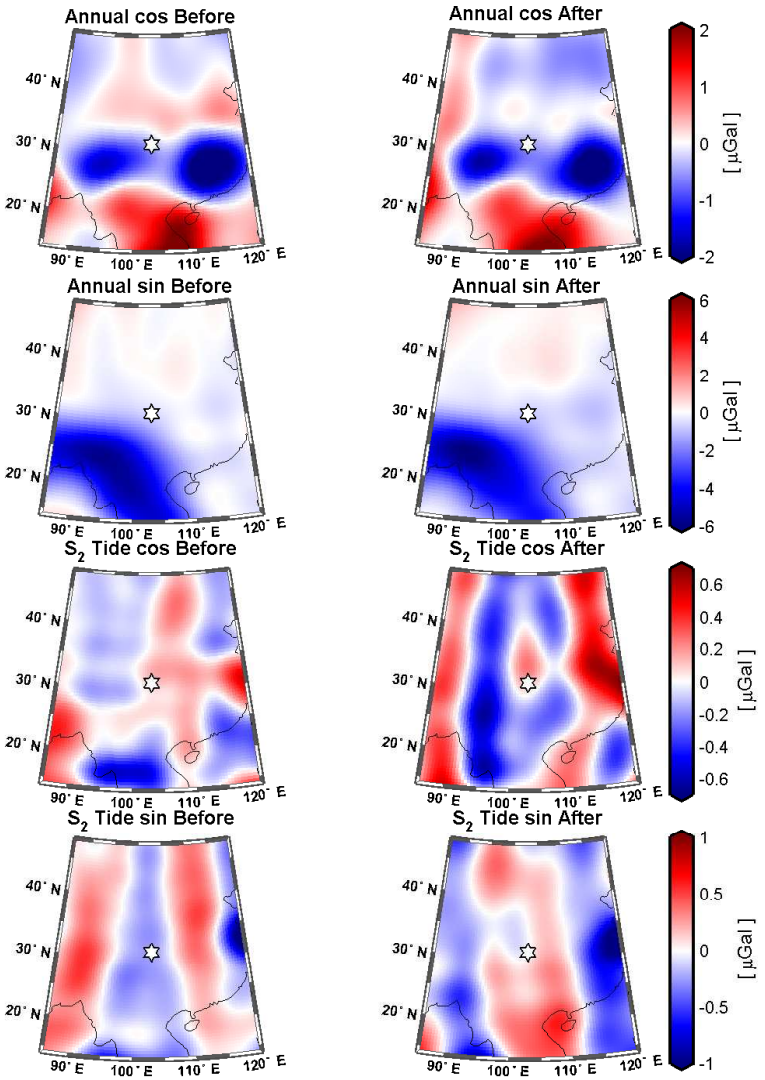

Figure 4.29: *Annual and S_2 Tide Waves Before and After Sichuan Earthquake (China) 2008 (GRACE Fan Filter 350 km)*

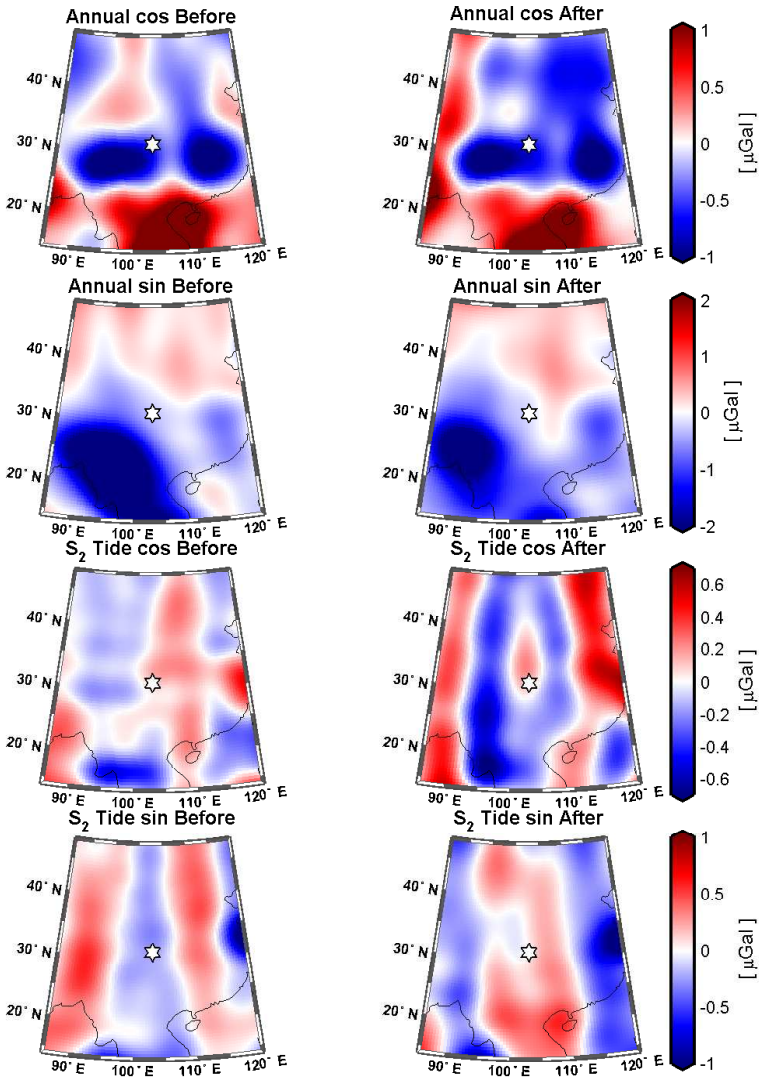

Figure 4.30: *Annual and* S_2 *Tide Waves Before and After Sichuan Earthquake (China) 2008 (GRACE-GLDAS Fan Filter* 350 km*)*

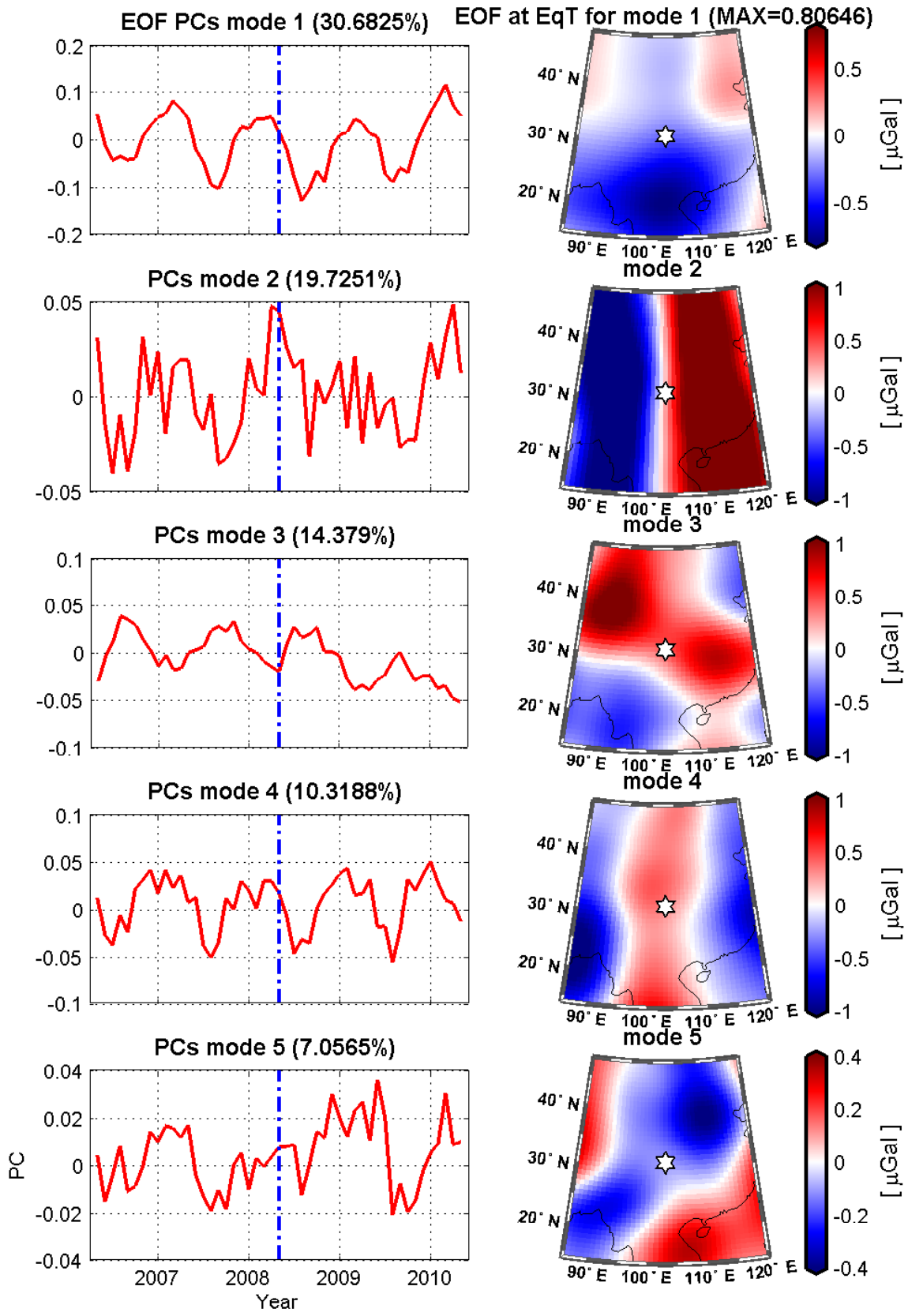

Figure 4.31: *EOF Analysis of Sichuan Earthquake (China) 2008 (GRACE Fan Filter* 350 km*)*

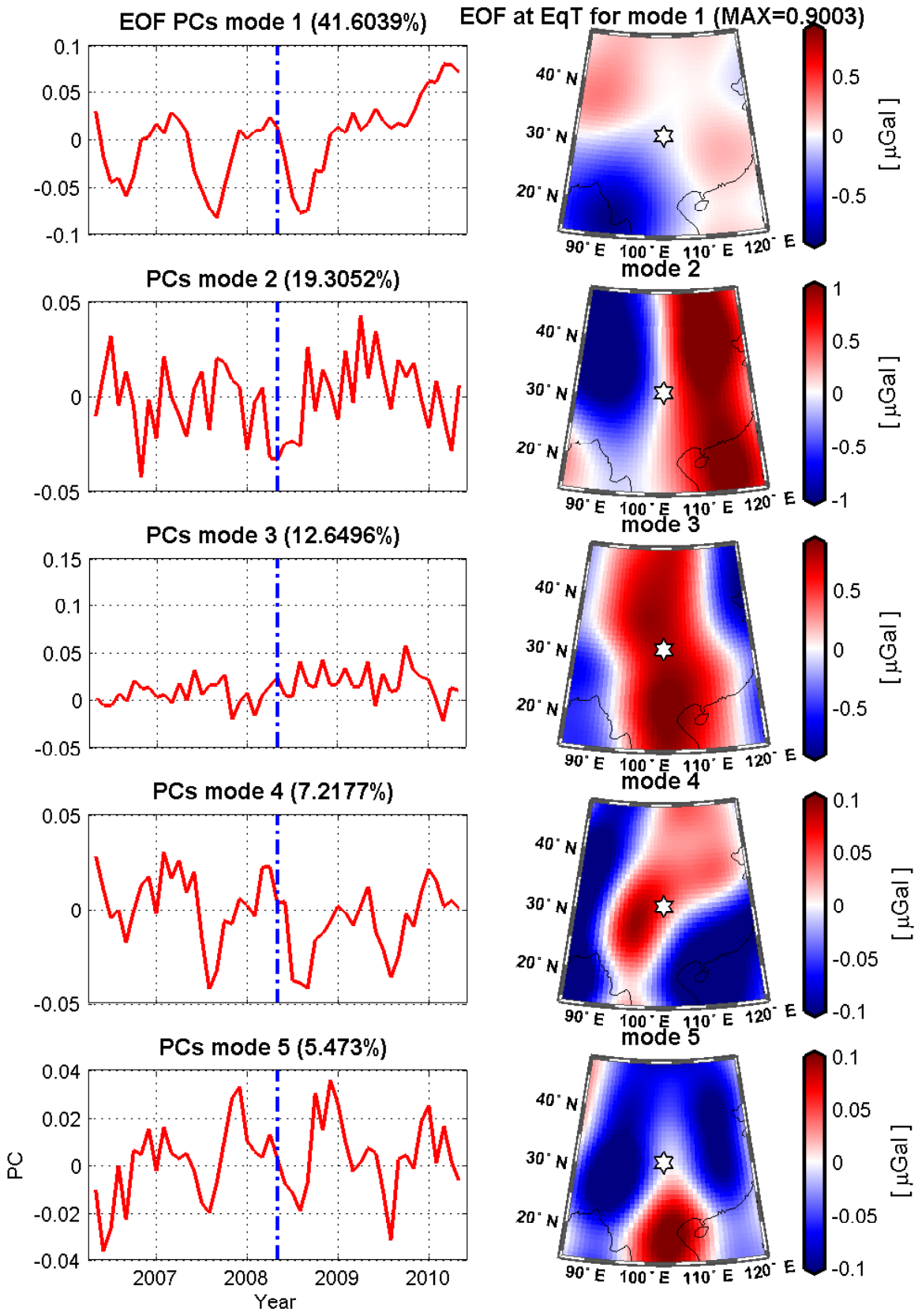

Figure 4.32: *EOF Analysis of Sichuan Earthquake (China) 2008 (GRACE-GLDAS Fan Filter* 350 km*)*

4.4 Maule Earthquake (Chile) 2010

4.4.1 The Geophysical Structure of the Maule Area

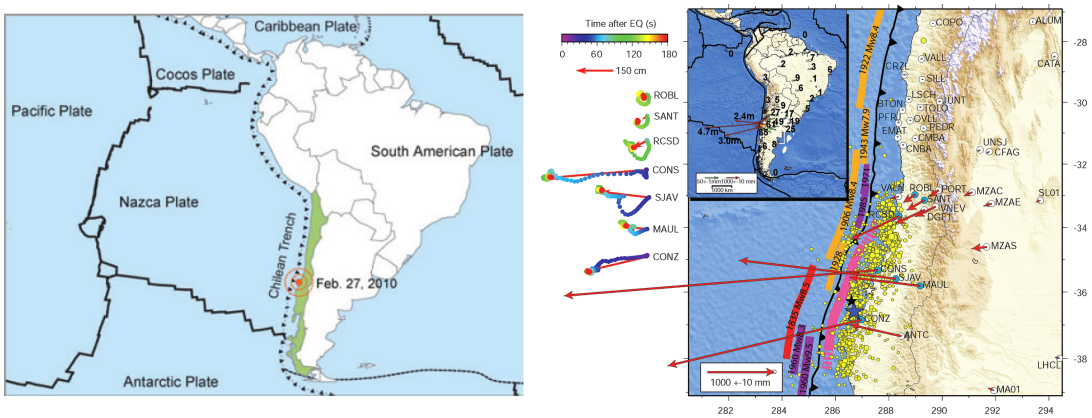

Figure 4.33: *The Plate (Shen-Tu and Mahdyiar, 2011) and GPS Monitor Movement of Maule Earthquake (Chile) 2010 (Vigny et al., 2011)*

The Maule earthquake ($M_w = 8.9$) is the sixth largest earthquake since modern record began. The earthquake occurred on Feb. 27, 2010 with the epicenter at (35.909°S, 72.733°W) and depth 35 km (from: USGS). The earthquake occurred on a locked megathrust fault where the oceanic Nazca plate subducts beneath the continental South American plate with the rate about 6.5 cm/year (see Fig. 4.33(a)). The rupture of the earthquake is more than 600 km along the strike (N18°E) and 60 km along dip (18°) in the area around Maule, Chile (Han et al., 2010).

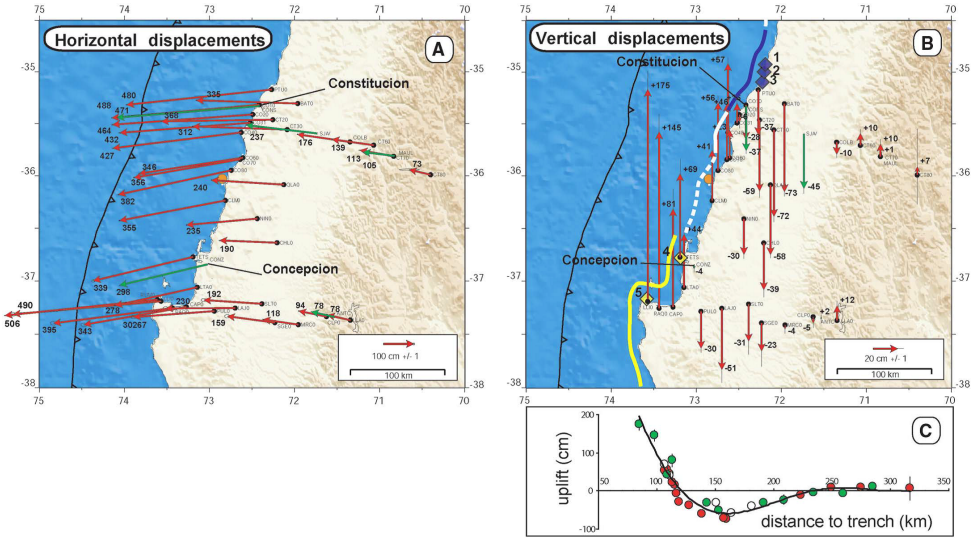

Figure 4.34: *Vertical and Horizontal Movement of Maule Earthquake (Chile) 2010 (Vigny et al., 2011)*

The figure above shows the relative movement horizontally and vertically on GPS station of the continent. The maximum horizontal movement is about 4.9 m and the vertical movement is about 1.8 m on land. Fig. 4.34(c) shows a cross section of land-level changes as a function of distance to the stretch. Compared to Sumatra-Andaman Earthquake (Indonesia) 2004 and Tōhoku Earthquake (Japan) 2011, there are limited scientific researches on Maule Earthquake (Chile) 2010.

4.4.2 Time Series Analysis

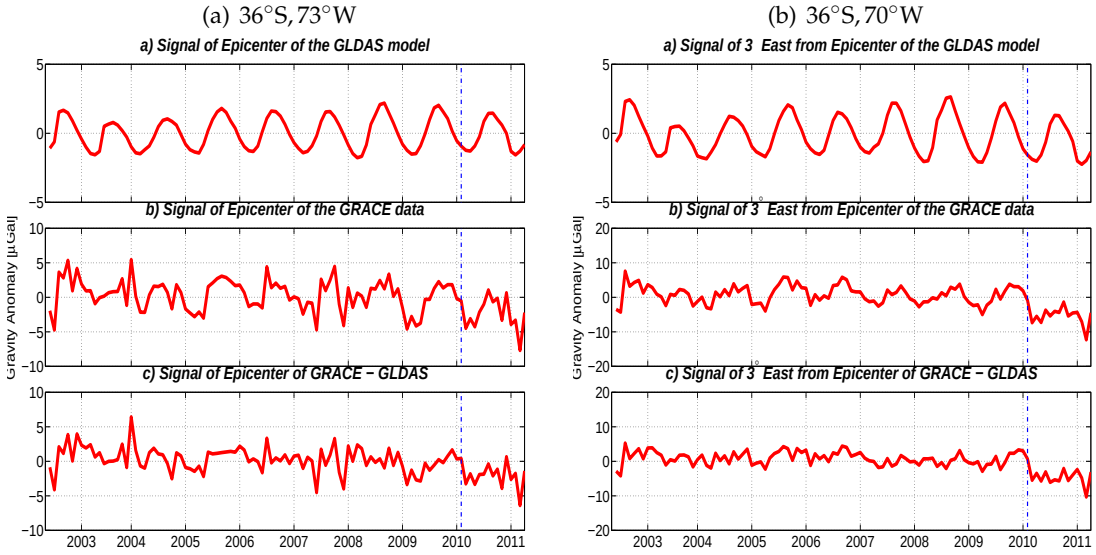

Figure 4.35: *Time Series in Epicenter and* 3° *East of Epicenter* (36°S, 73°W) *of Maule Earthquake (Chile) 2010 (GRACE Gauss Filter* 350 km*)*

The time series of the Epicenter from GRACE data is presented in Fig. 4.35 left. (b) is the raw GRACE data, the annual wave is pretty obvious in the graph. GLDAS model is showed in (a) and the hydrological effect is quite annual. After subtracting GLDAS model from GRACE data, compared to (b) the periodic signals are much less in (c).

The figure on the right, shows the same signal from the point 3° east of the Epicenter. The periodical hydrological signal is similar with the one on the left. Time series contain significant rupture which is approximately 5 μGal, after the earthquake the signal remains in the lower position different from Sumatra-Andaman Earthquake (Indonesia) 2004 which starts to recover.

Maule Earthquake is in South America and near to the Amazon area where the hydrological effect is quite strong and not easy to model, which will have a negative effect in the modeling of the earthquake signals.

There are three types of the time series there:

1. Signal in epicenter. From the time series there is no significant changepoint. Fitting the signal in the Epicenter shows that it is better to fit separately. The postseismic recovery rate τ is not stable for this fitting. The Two Phase test cannot detect the rupture as well. (See Fig. 4.36)

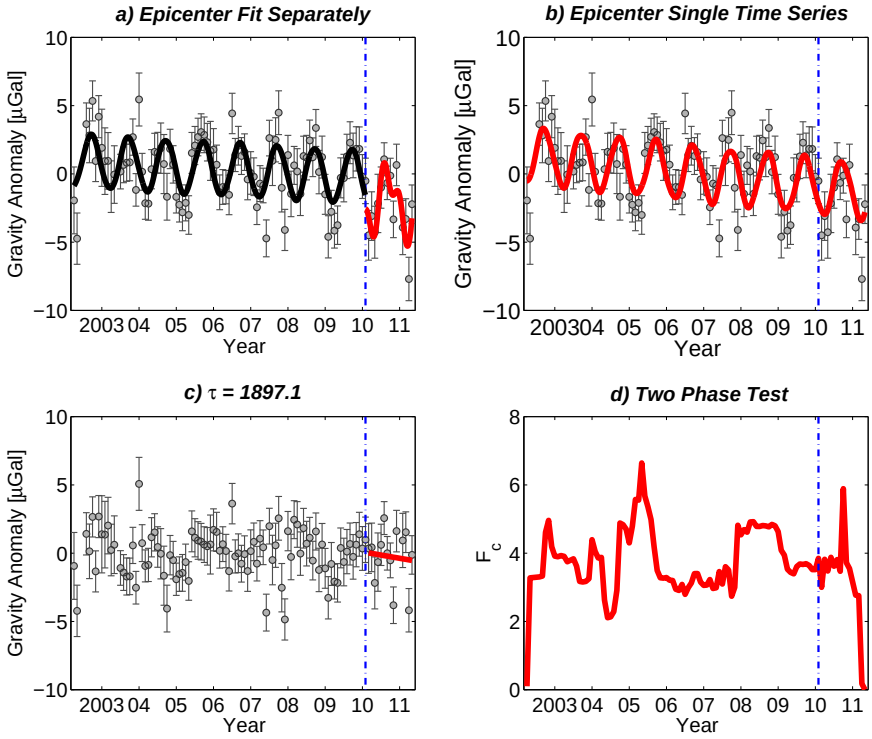

Figure 4.36: *Fit and Changepoint Detection of Time Series in Epicenter (36°S, 73°W) of Maule Earthquake (Chile) 2010 (GRACE Gauss Filter 350 km)*

2. The time series signal in the 5° southwest of the epicenter. There is a very significant jump in the time series, however, the signal recovers very quickly to the original state. τ equals 0 and the value is reasonable. From Sec. 3.7.3, it shows small τ which indicates that it is very elastic in that area. (See Fig. 4.37)

3. In Fig. 4.38 is a point 3° east of the epicenter and the jump in the earthquake time is significantly visible. And after the earthquake the gravity anomaly remains in a low state and there is no sign of the recovery. Meanwhile $\tau = 9.1$ which is unreasonable. But the Two Phase test can detect the time of the rupture.

4.4.3 Rupture Detection

Compare the Fig. 4.39 and 4.40, the Two Phase test can detect the coseismic change which is in the east of the epicenter in both of them. But the area with hydrological signal subtracted is smaller than that in the raw GRACE data. The hydrological signal indeed interferes the rupture detection. Meanwhile on the other side, the ratio test can detect the coseismic change as well.

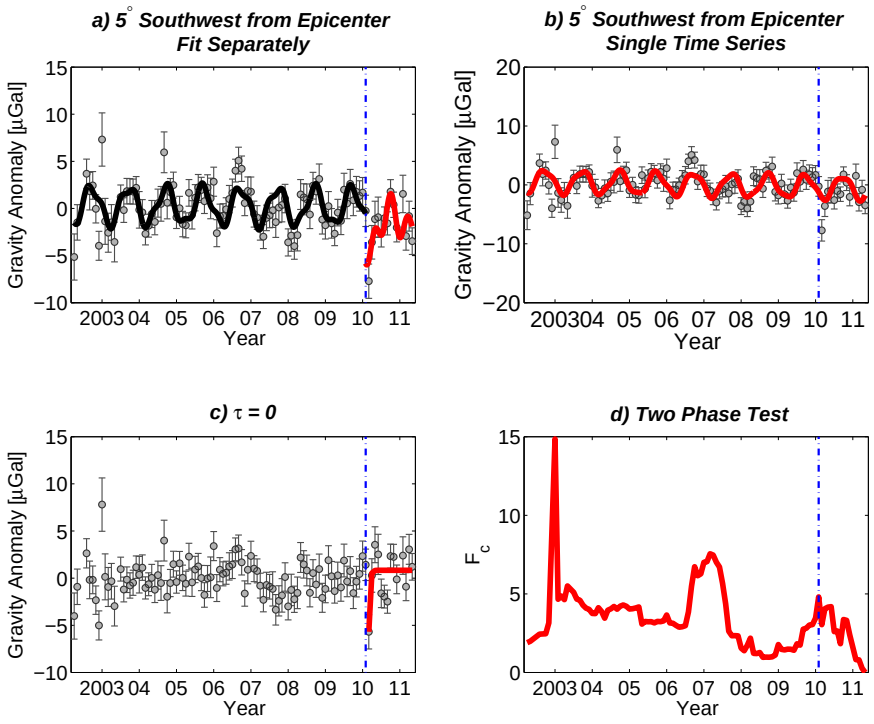

Figure 4.37: *Fit and Changepoint Detection of Time Series in* 5° *Southwest of Epicenter* (36°S, 73°W) *of Maule Earthquake (Chile) 2010 (GRACE-GLDAS Gauss Filter* 350 km)

Fig. 4.41 contains only GRACE data, the signal is about 4 μGal in the area in the east of the epicenter. The large signal in the north areas are the remaining hydrological noise which is not caused by the earthquake. The difference before and after the earthquake does not reveal any event.

In Fig. 4.42, after eliminating the hydrological signal, the earthquake signal becomes apparent in (a). The only peak value in the graph is to the east of the epicenter which is about 4 μGal.

Compare Fig. 4.41 and 4.42 with Fig. 4.43 from Heki and Matsuo (2010*b*) with the smaller area than this research, the pattern is similar, with the peak in the east of the epicenter and second peak in the sea area which is 5° southeast of the epicenter. The gravity change reported by Heki and Matsuo (2010*b*) and Han et al. (2010) is approximately 5 μGal, however due to different filter and data (Heki and Matsuo (2010*b*) used Fan filter 300 km and Han et al. (2010) used level 1B data), the gravity change detected here is about 4 μGal. No significant gravity change was found offshore.

4.4.4 Least Squares Adjustment

In Fig. 4.45, the trend before the earthquake shows negative signal in the south of the epicenter where it is the Patagonia Icefield melting. The Patagonia Icefield is the second largest ice body in the Southern Hemisphere (Warren and Sudgen, 1993). It is a place for studying the global

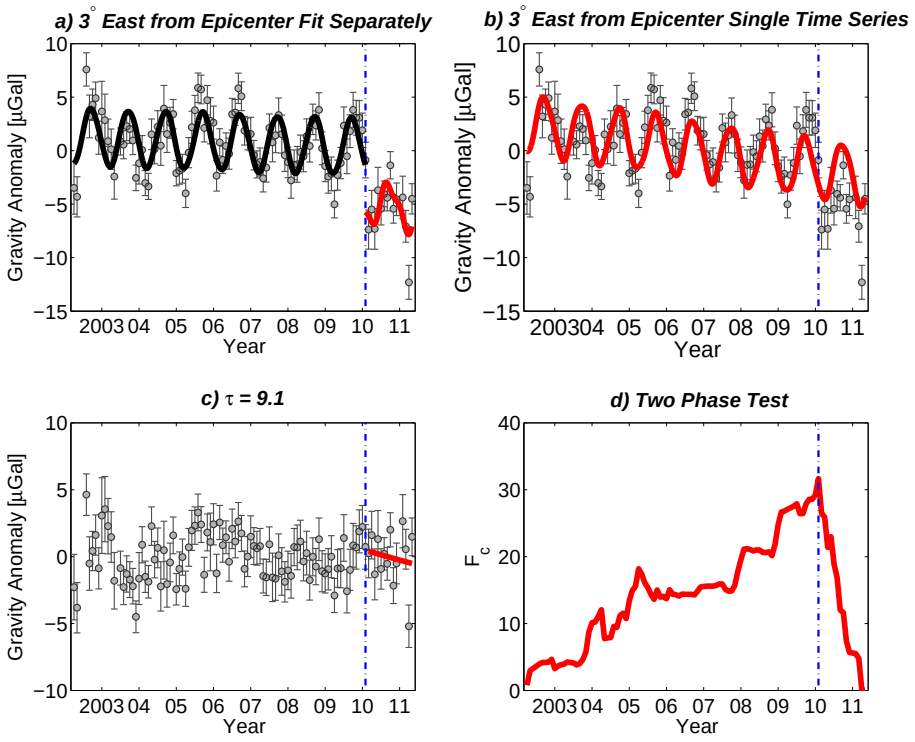

Figure 4.38: *Fit and Changepoint Detection of Time Series in* 3° *East of Epicenter* (36°S, 73°W) *of Maule Earthquake (Chile) 2010 (GRACE-GLDAS Gauss Filter* 350 km*)*

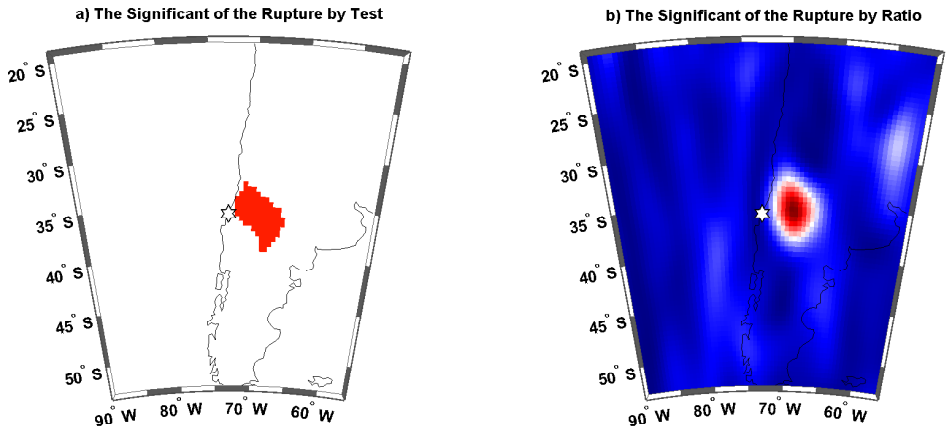

Figure 4.39: *Detection of the Rupture by Test of Maule Earthquake (Chile) 2010 (GRACE Gauss Filter* 350 km*)*

warming. But after the earthquake no postseismic signal is found, due to the reason that in gravity change in South America:

1. No regular seasonal changes;

2. Large interannual variations;

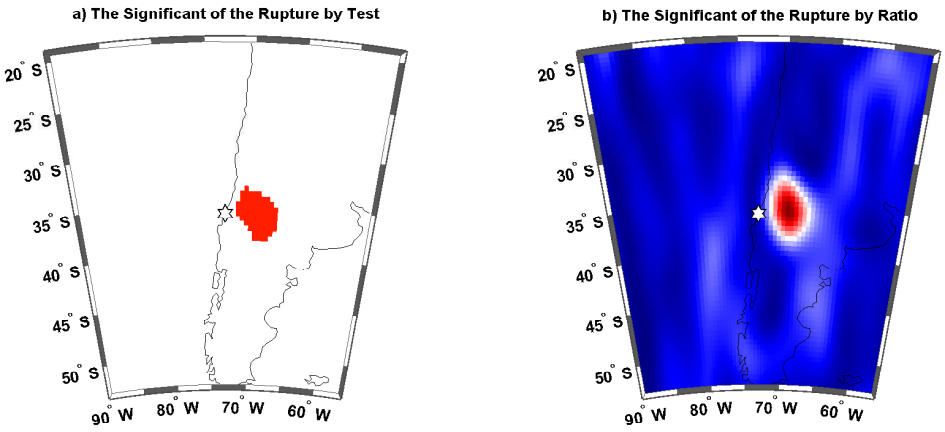

Figure 4.40: *Detection of the Rupture by Test of Maule Earthquake (Chile) 2010 (GRACE-GLDAS Gauss Filter* 350 km*)*

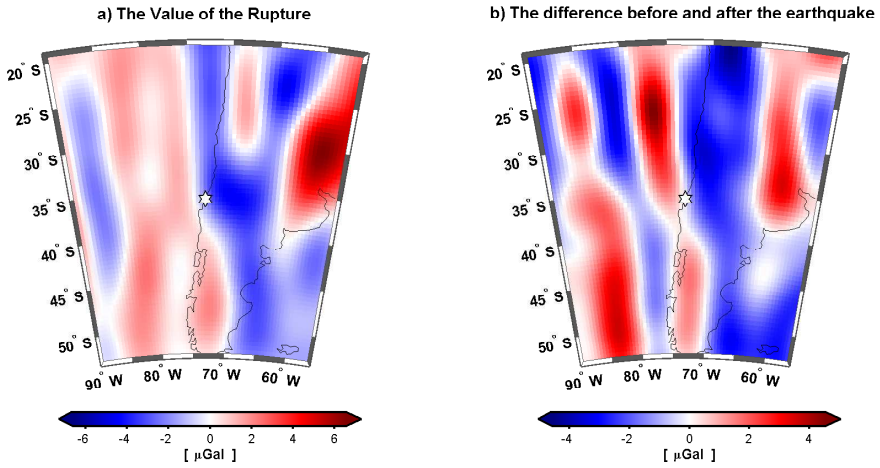

Figure 4.41: *Rupture and Gravity Field Before and After Maule Earthquake (Chile) 2010 (GRACE Gauss Filter* 350 km*)*

3. Difficult to model (Heki and Matsuo, 2010*a*).

Han et al. (2010) explained the coseismic signal as the result of crustal dilatation as well as surface subsidence at the inland region.

4.4.5 Empirical Orthogonal Functions (EOF) Analysis

Two EOF analysis will be mentioned here, one is GRACE only signal (Fig. 4.46) and the other is GRACE signal subtracting GLDAS model (Fig. 4.47). In both mode 1 of EOF fields, the strongest signals are in the place where the coseismic signal is detected in Fig. 4.42. However, both PCs show the changes when earthquake took place, meanwhile after subtracting the GLDAS, the annual frequency is much less.

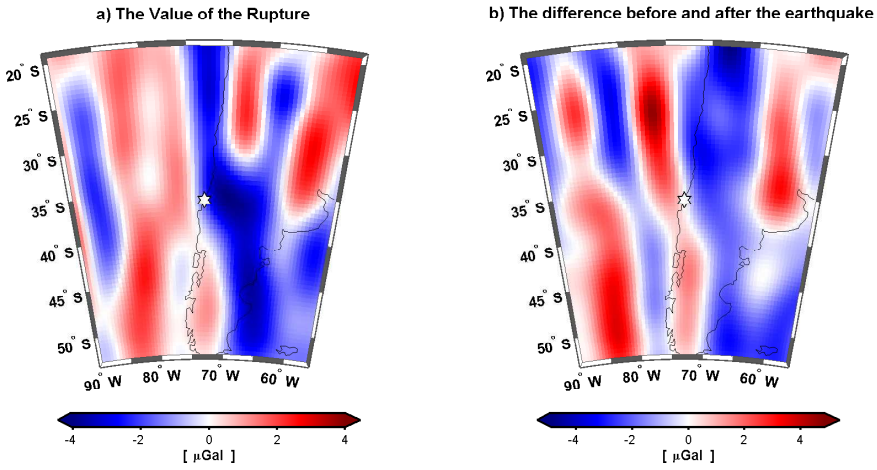

Figure 4.42: *Rupture and Gravity Field Before and After Maule Earthquake (Chile) 2010 (GRACE-GLDAS Gauss Filter* 350 km*)*

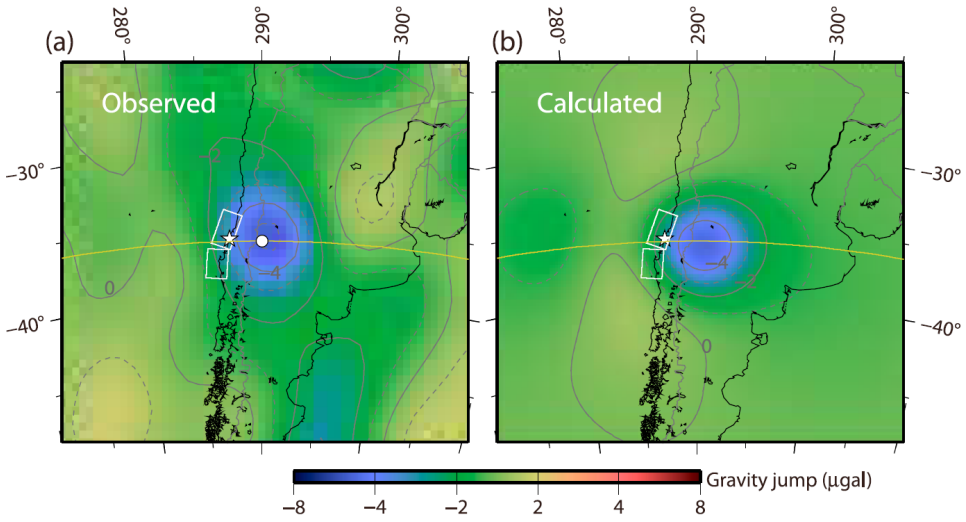

Figure 4.43: *Result from Heki and Matsuo (2010a)*

In mode 2, the change is mainly in the Patagonia Icefield. It shows the increase of that area. Mode 3s are similar in both graphs. And when it comes to mode 4, after subtracting the hydrology signal, the signal in the east of epicenter becomes more obvious. The pattern is similar to the earthquake signal but it is extremely small.

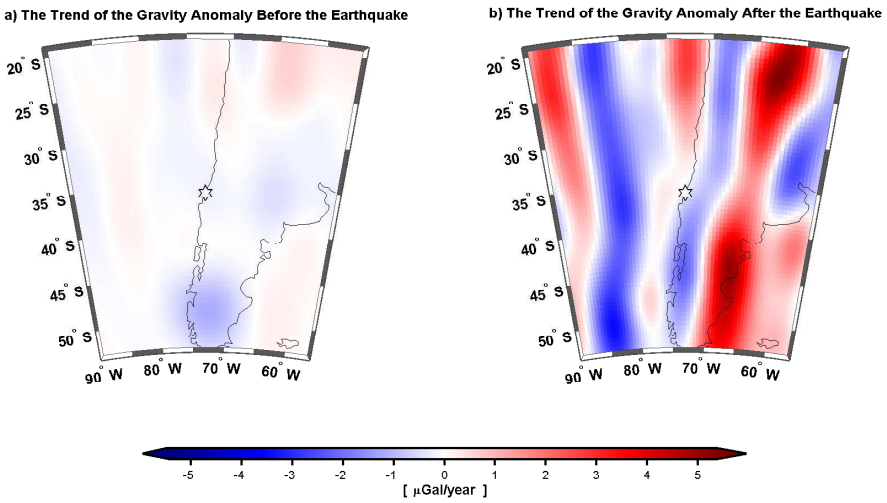

Figure 4.44: *Gravity Trend Before and After Maule Earthquake (Chile) 2010 (GRACE-GLDAS Gauss Filter* 350 km*)*

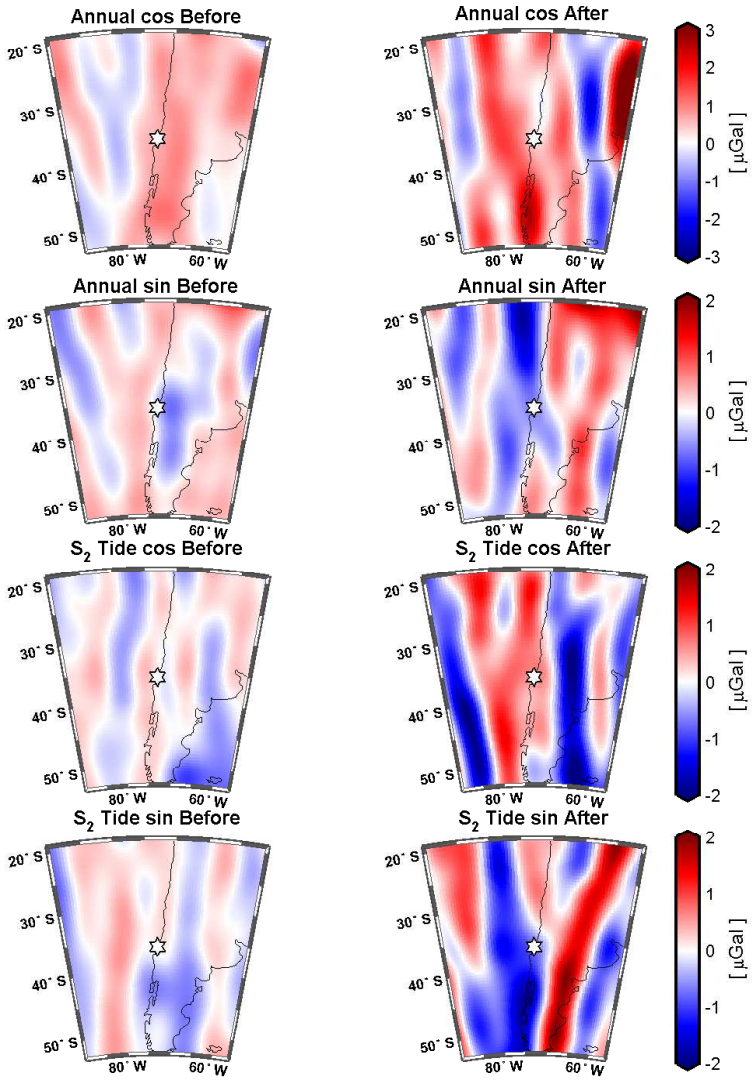

Figure 4.45: *Annual and* S_2 *Tide Waves Before and After Maule Earthquake (Chile) 2010 (GRACE-GLDAS Gauss Filter* 350 km*)*

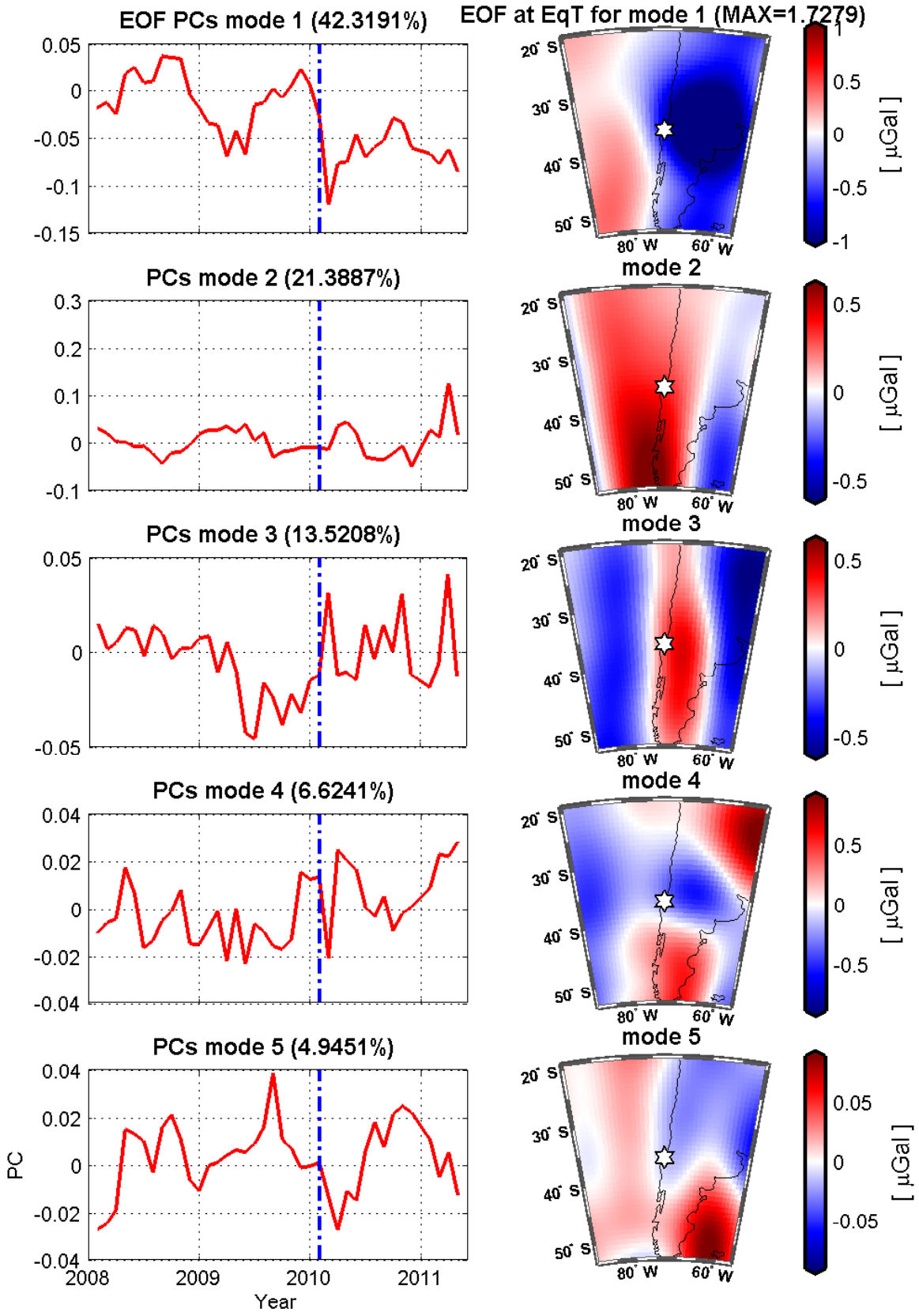

Figure 4.46: *EOF Analysis of Maule Earthquake (Chile) 2010 (GRACE Fan Filter* 350 km*)*

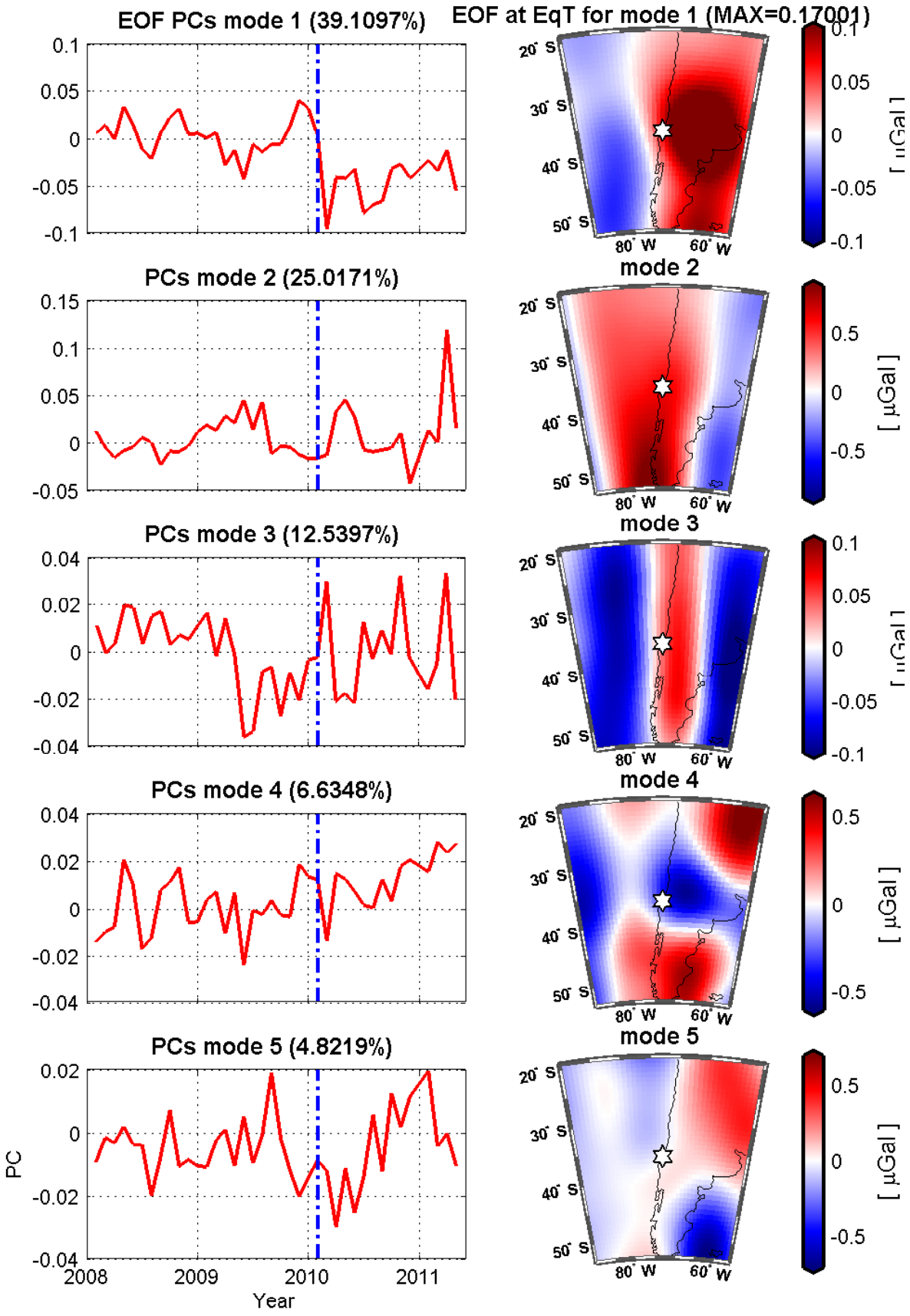

Figure 4.47: *EOF Analysis of Maule Earthquake (Chile) 2010 (GRACE-GLDAS Fan Filter* 350 km*)*

4.5 Tōhoku Earthquake (Japan) 2011

4.5.1 The Geophysical Structure of the Tōhoku Area

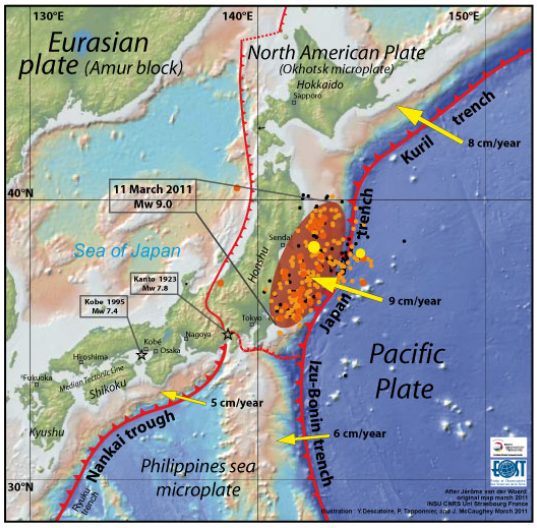

Figure 4.48: *The Tectonic Plate of Tōhoku Earthquake (Japan) 2011 (McCaughey et al., 2011)*

On Mar. 11, 2011, an earthquake with magnitude 9.0 struck at the Japan Trench ruptured the fault as large as 500 km × 200 km (Ammon et al., 2011; Ozawa et al., 2011). The geophysical structure of the area around Japan is very complex. There are four tectonic plates in and near Japan: Eurasian plate, North American plate, Pacific plate and the Philippines sea microplate as it is showed in Fig. 4.48. The orange area is the rupture area of the earthquake and the largest yellow dot is the epicenter (38.297°N, 142.372°E) (from:USGS) where the rupture process began. The earthquake depth is 30 km (from:USGS).

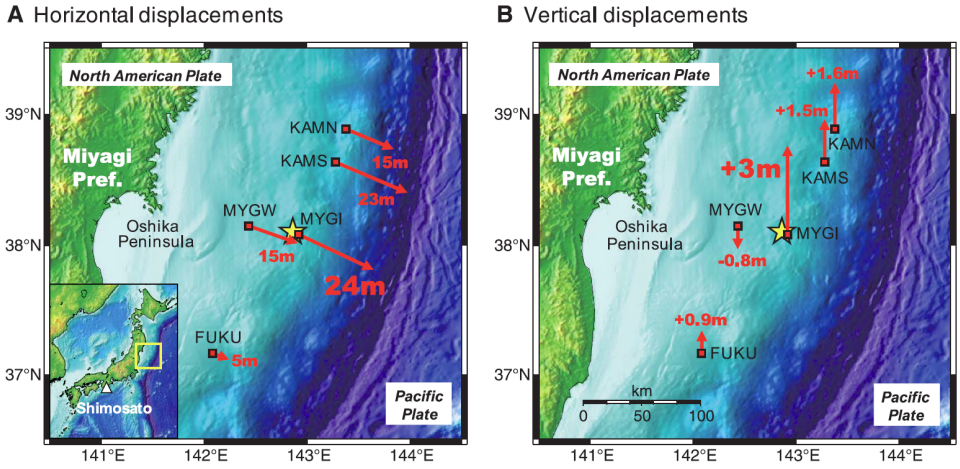

Figure 4.49: *Coseismic Change of Tōhoku Earthquake (Japan) 2011 (Sato et al., 2011)*

The maximum horizontal coseismic change is about 24 m and the corresponding vertical

displacement is about 3 m. Due to the limited data, the analysis of Tōhoku Earthquake is partly done and the further available data can improve the analysis.

4.5.2 Time Series Analysis

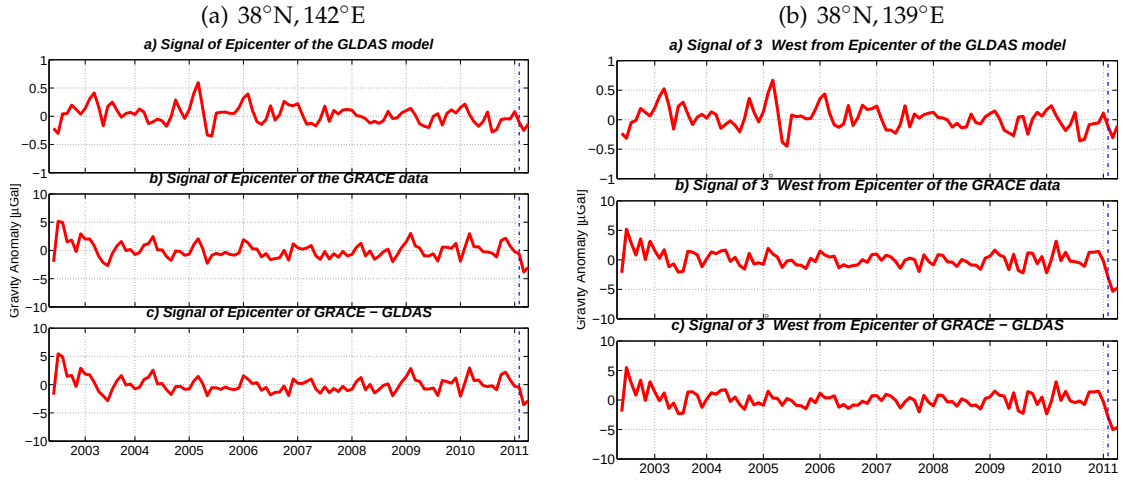

Figure 4.50: *Time Series in Epicenter and* 3° *West of Epicenter (*38°N, 142°E*) Tōhoku Earthquake (Japan) 2011 (Fan Filter* 350 km*)*

There is a significant jump of the signal when the earthquake took place in GRACE data. The situation in Tōhoku Earthquake (Japan) 2011 is similar to that in Sumatra-Andaman Earthquake (Indonesia) 2004 that the epicenter is in the sea where GLDAS model is not available. Therefore GLDAS model in the epicenter is mainly due to the leakage effect. For Fan filter 350 km the coseismic change is about 4 μGal in the epicenter. The largest rupture is in the west of the epicenter which is about 5 μGal and is smaller than the result > 7 μGal of Matsuo and Heki (2011) which used Fan filter 300 km. The result of the Gauss filter can be seen in Fig. D.4 which is larger than the result of the Fan filter.

Fig. 4.51 shows that separate fitting is better than the overall fitting. The rupture is about 4–5 μGal. τ equals 0.1, which is estimated by only two points and is not a good estimation of the postseismic signals. (d) shows the Two Phase test, it seems that the Two Phase test cannot properly detect the jump at the end of the signal.

4.5.3 Rupture Detection

The Two Phase test does not detect any signal jump. But the Ratio method can detect significantly the rupture in the west part of the epicenter. The area is similar to the result of (Matsuo and Heki, 2010).

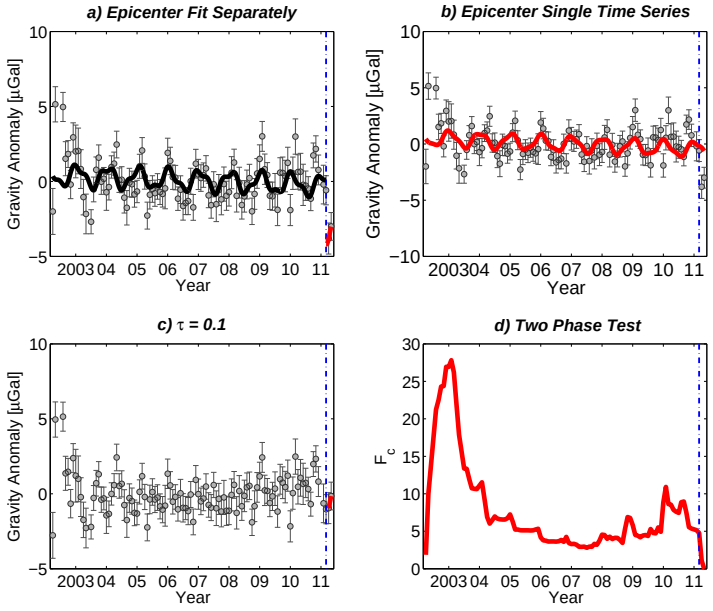

Figure 4.51: *Fit and Changepoint Detection of Time Series in Epicenter* (38°N, 142°E) *of Tōhoku Earthquake (Japan) 2011 (GRACE Fan Filter* 350 km*)*

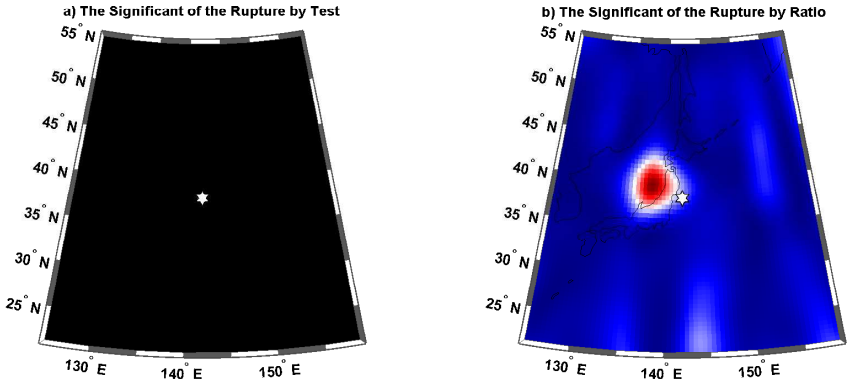

Figure 4.52: *Detection of the Rupture by Test of Tōhoku Earthquake (Japan) 2011 (GRACE Fan Filter* 350 km*)*

4.5.4 Least Squares Adjustment

In Fig. 4.53, by least squares adjustment, the rupture can be clearly seen in the west direction of the epicenter and the rupture value is about the 5–6 μGal. The result of the Gauss filter is larger in Fig. D.5. Similar to the result of Matsuo and Heki (2011) in Fig. 4.54, such signal is interpreted as the crustal dilatation of the landward plate by Matsuo and Heki (2011).

Meanwhile in Fig. 4.55, there is no significant gravity trend before the earthquake. After earthquake, because the data set only contains two months signals after Mar. 2011, the postseismic signal is only the two months' trend. But in the spatial domain, it shows negative trend after the earthquake.

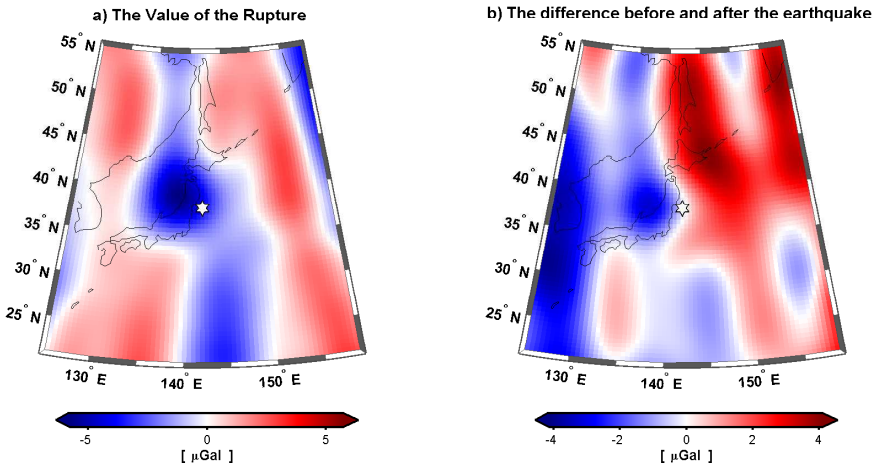

Figure 4.53: *Rupture and Gravity Field Before and After Tōhoku Earthquake (Japan) 2011 (GRACE Fan Filter* 350 km*)*

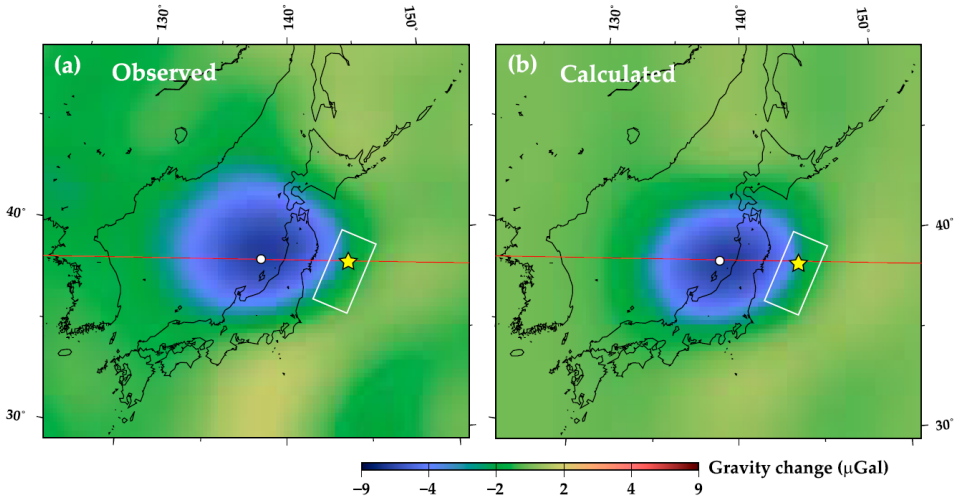

Figure 4.54: *Result from Matsuo and Heki (2011)*

In Fig. 4.56, due to the lack of data after earthquake, the adjustment after earthquake cannot estimate all the parameters thus the results is not displayed. The annual signals are mostly in the land area, but the S_2 signals are both in the land and ocean areas before the earthquake.

4.5.5 Empirical Orthogonal Functions (EOF) Analysis

The mode 1 of EOF analysis shows the big changes at the end of the PC. And in the graph, the changes are just on the two sides of the epicenter. And the peak value is similar to the Fig. 4.53 and 4.55. So the detection of the coseismic signal is successful here mainly because the magnitude of the earthquake is too large. Mode 2 PC shows large signal still in the area west to the epicenter. In the PC, the jump is also significant. In mode 3, no jump in the PC but the EOF field shows large positive signal in the southeast area to the earthquake epicenter. In mode 4

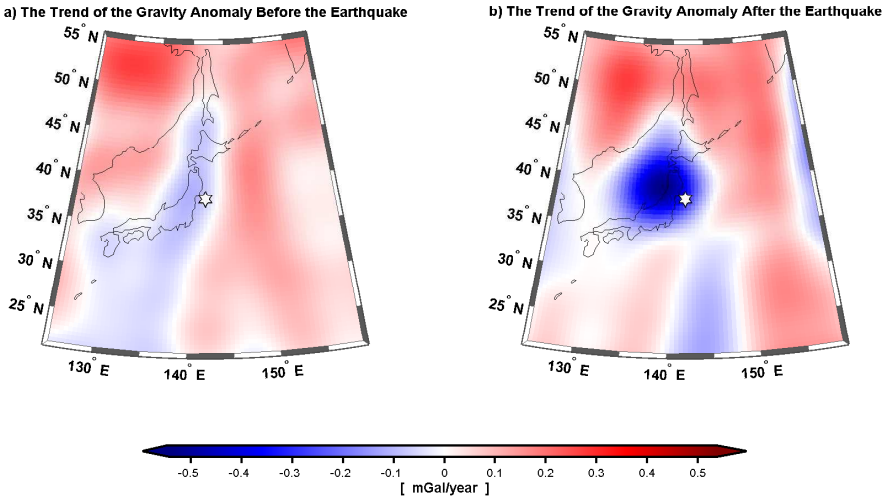

Figure 4.55: *Gravity Trend Before and After Tōhoku Earthquake (Japan) 2011 (GRACE Fan Filter* 350 km*)*

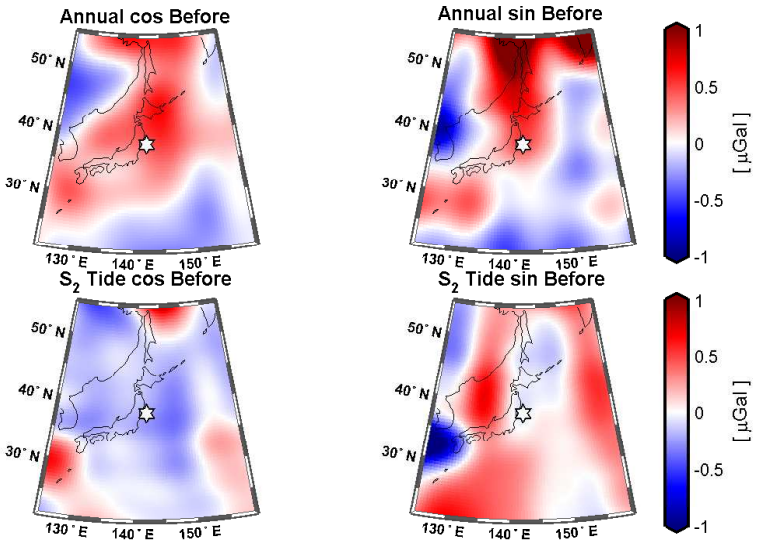

Figure 4.56: *Annual and* S_2 *Tide Waves Before Tōhoku Earthquake (Japan) 2011 (GRACE Fan Filter* 350 km*)*

of EOF there is no big jump at the earthquake time as well. In mode 5, which has the same magnitude with mode 1, the pattern of the signal is very interesting, not only can the coseismic change be seen, but also strong signal in the south of the epicenter. The reason for such signal is unknown. So EOF can detect the changes of Tōhoku Earthquake signal although with the limited data after the earthquake.

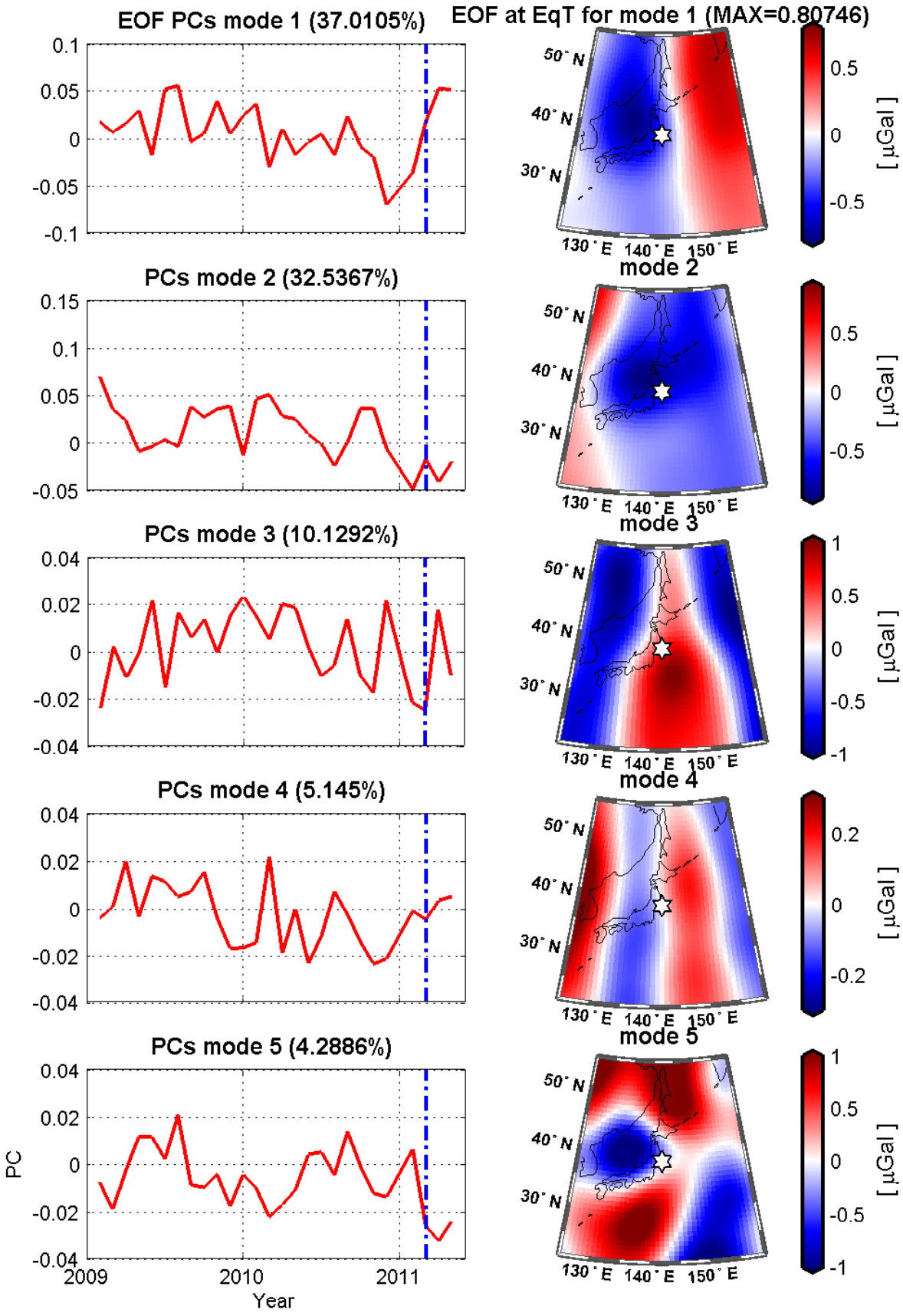

Figure 4.57: *EOF Analysis of Tōhoku Earthquake (Japan) 2011*
(GRACE Fan Filter 350 km*)*

Chapter 5

Conclusion and Recommendation

5.1 Conclusion

The conclusions of the thesis are:

1. GRACE can detect some of the large earthquakes, but it depends on the earthquake type, area and the length of the time-series before and after the earthquake.

2. The rupture of Sumatra-Andaman Earthquake (Indonesia) 2004 can be successfully detected by the Two Phase test and the Ratio test in the area of the Andaman Sea. The maximum rupture of the Sumatra-Andaman Earthquake (Indonesia) 2004 is >6 μGal for the Fan filter 350 km and >10 μGal for the Gauss filter 350 km. Meanwhile the results from Han et al. (2006) is $\sim$15 μGal that Han used his own dataset and Gauss smoothing of 300 km in longitude and 200 km in latitude and from de Linage et al. (2009) is 14 μGal for peak to peak difference by Gauss filter 350 km. The postseismic signal is estimated by both least squares adjustment and the Maxwell Relaxation time. The maximum value of the least squares adjustment of Gauss filter 350 km is $\sim$1 μGal/year which is less than Schmidt et al. (2007) which used only destriping filter. For the Maxwell Relaxation time, it is about 0.5–1.3 year comparing to 0.4–0.8 year by de Linage et al. (2009) using different ways of fitting. The EOF analysis in the mode 1 shows the rupture process clearly and also it can be seen in the PC.

3. Because of the earthquake magnitude and hydrological effect, the time series analysis in the Sichuan Earthquake (China) 2008 cannot show any earthquake signal even with the GLDAS model subtracted. But in the EOF analysis, suspicious earthquake signal detected in the mode 2 with the magnitude less than 1 μGal.

4. The coseismic signal of the Maule Earthquake (Chile) 2010 is successfully detected in the time series by the Two Phase test and the Ratio test. The rupture is approximately 4 μGal less than 5 μGal from Heki and Matsuo (2010*b*) which use the Fan filter 300 km. No significant postseismic changes detected.

5. The coseismic change of the Tōhoku Earthquake (Japan) 2011 is successfully detected in the time series by the Ratio test but the detection fails in the Two Phase test due to the rupture appears at the end of the time series. The rupture is approximately 5–6 μGal similar to Matsuo and Heki (2011). The postseismic data is the result only for two months signals and there is significant change in the west of the epicenter.

6. The gravity change of the Sumatra-Andaman Earthquake (Indonesia) 2004, Maule Earthquake (Chile) 2010 and Tōhoku Earthquake (Japan) 2011 are the same with the other papers despite small differences due to the different filters and datasets.
7. The different filters will affect the magnitude of the gravity change, so the real gravity changes of those four areas are still under debate.
8. Time series analysis shows the different behavior of the different earthquakes. Usually the coseismic signals are not at the epicenter but the vicinity.
9. The absolute value of the Maxwell Relaxation time is not accurate enough because of the regression model and the dataset (the length of the time series and the filtering method). As many unknown parameters have to be estimated and the instability of the estimation of the term $e^{-(t-t_0)/\tau}$ will interfere the estimation of the other parameters, the model for the estimation is not rigorous enough. However, the relative value of Maxwell Relaxation time can reveal the speed of the postseismic recovery. Meanwhile, no test for the significant of τ is done.
10. Sumatra-Andaman Earthquake (Indonesia) 2004 and Maule Earthquake (Chile) 2010 signals are both significant in the spatial and time domain. Due to the limited dataset, the detection of the Tōhoku Earthquake (Japan) 2011 succeeds only in the spatial domain. For Sichuan Earthquake (China) 2008, it is not significant either in time domain nor the spatial domain.
11. EOF can be used for the separation of the earthquake signals. For the huge earthquake, the mode 1 PC can reveal the signals. Such as the Sumatra-Andaman Earthquake (Indonesia) 2004, the earthquake signal on both sides can be seen in mode 1 EOF.
12. Compared to other geodetic technics, the gravity method can detect the underground signals and in the ocean areas, which is very important for the earthquake analysis.

5.2 Recommendation

The research can be improved in many aspects:

1. There are many datasets of GRACE (GFZ, CSR, GSFC, DEOS, ITG, CNES) and they are using different methods to convert the Level 1 data to the spherical harmonics. So different data can have slightly different results and there should be one which can get better results in the analysis of the earthquake signal.
2. The filter methods can be improved. There are many different methods which are suitable for the different applications. Regional filter and the filter can retain the earthquake signal but still getting rid of the north to south stripe is a good way to do further research.
3. The time series analysis of the coseismic jump can be improved. The singular-spectrum analysis (Vautard et al., 1992), the Bayesian time series analysis (Einarsson et al., 2010) can be better than the simple Two Phase and Ratio detection methods, which have obvious limitations.
4. The hydrological model should be improved especially in the Sichuan and Chile areas where it can have huge effects on the analysis of the earthquake signals.

5. The method in analyzing of the earthquake signal can be changed. EOF has its advantages that it has flexible bases. But the EOF base does not have a physical meaning. Different time scales and the spatial scales will also change the results of the EOF bases. Alternatively, Slepian method, Radial basis method and Wavelet method are also capable of analyzing the approximately plain spatial concentrated signals. There are some scientists who had done the research in Slepian analysis of the Sumatra area and detect the jump in Slepian coefficients (Han et al., 2008) and the analysis of the GRACE satellite to satellite tracking data (Han et al., 2010). Meanwhile the Wavelet method is also applied in Sumatra analysis (Panet et al., 2010).
6. The dislocation theorem by Wenke Sun (Sun and Okubo, 1993) can be applied.
7. The combination of the other geodetic methods such as the GPS, Interferometric Synthetic Aperture Radar (InSAR) or ground gradiometry with the satellite gradiometry's data is necessary. Because the satellite gravity data's resolution is so small that the detailed earthquake processes and structures are impossible to be detected.
8. The related geophysical model could be combined with the gravity data such as the ocean contribution (Broerse et al., 2011; Melini et al., 2010) and the earthquake model as well.
9. "Long time series" future gravity missions can also be added into the analysis, e.g Broerse et al. (2011).
10. As there is a very precise GPS network in Japan, the further study of the gravity changes due to the Tōhoku Earthquake (Japan) 2011 can help the scientists understand the post-seismic mechanism.

Bibliography

Abart, C. (2005), Assessment of solution strategies for GRACE gravity field processing, Master's thesis, Institute of Navigation and Satellite Geodesy, Graz University of Technology.

Ammon, C. J., Lay, T., Kanamori, H. and Cleveland, M. (2011), 'A rupture model of the 2011 off the Pacific coast of Tohoku Earthquake', *Earth Planets Space* **63**, 693 – 696.

Balasis, G. and Mandea, M. (2007), 'Can electromagnetic disturbances related to the recent great earthquakesbe detected by satellite magnetometers?', *Tectonophysics* **431**(1-4), 173 – 195.

Bentel, K. (2009), Empirical Orthogonal Function Analysis of GRACE Gravity Data, Master's thesis, Universität Stuttgart.

Bettadpur, S. V. (2007), GRACE UTCSR Level-2 Processing Standards Document For Level-2 Product Release 0004, Technical report, Center for Space Research, University of Texas at Austin.

Broerse, D. B. T., Vermeersen, L. L. A., Riva, R. E. M. and van der Wal, W. (2011), 'Ocean contribution to co-seismic crustal deformation and geoid anomalies: Application to the 2004 December 26 Sumatra-Andaman earthquake', *Earth and Planetary Science Letters* **305**(3-4), 341 – 349.

Broerse, D. B. T., Visser, P., Bouman, J., Fuchs, M., Vermeersen, B. and Schmidt, M. (2011), Modelling and Observing the 8.8 Chile and 9.0 Japan Earthquakes Using GOCE, Vol. ESA SP-696, Proc. of `4th International GOCE User´, Munich, Germany 31 March - 1 April 2011.

Cannelli, V., Melini, D., Piersanti, A. and Boschi, E. (2008), 'Postseismic signature of the 2004 Sumatra earthquake on low-degree gravity harmonics', *Journal of Geophysical Research* **113**, B12414.

Chao, B. F. and Gross, R. S. (1987), 'Changes in the Earth's rotation and low-degree gravitational field induced by earthquakes', *Geophysical Journal. Royal Astronomical Society* **91**, 569 – 596.

Chen, J. L. and Wilson, C. (2008), 'Low-Degree Gravitational Changes from GRACE, Earth Rotation, Climate Models, and Satellite Laser Ranging', *Geophysical Research Letters* **32**, L14405.

Chen, J. L., Wilson, C. R., Famiglietti, J. S. and Rodell, M. (2005), 'Spatial sensitivity of the Gravity Recovery and Climate Experiment (GRACE) time-variable gravity observations', *Journal of Geophysical Research* **110**(9), B08408.

Chen, J. L., Wilson, C. R. and Seo, K. W. (2008), 'S_2 tide aliasing in GRACE time-variable gravity solutions', *Journal of Geodesy* **83**, 679 – 687.

Chen, J. L., Wilson, C. R., Tapley, B. D. and Grand, S. (2007), 'GRACE detects coseismic and postseismic deformation from the Sumatra-Andaman earthquake', *Geophysical Research Letters* **34**(13), L13302.

Chen, J. L., Wilson, C. R., Tapley, B. D., Yang, Z. L. and Niu, G. Y. (2009), '2005 drought event in the Amazon River basin as measured by GRACE and estimated by climate models', *Journal of Geophysical Research* **114**, B05404.

Cheng, M. K. and Tapley, B. D. (2004), 'Variations in the Earth's oblateness during the past 28 years', *Journal of Geophysical Research* **109**(B9), B09402.

Coleman, T. and Li, Y. (1996), ''an interior, trust region approach for nonlinear minimization subject to bounds'', *SIAM Journal on Optimization* **6**, 418 – 445.

Conry, M. (2004), Notes for Mechanical Engineering Students, Technical report, Univerisity College Dublin. Lecture Notes.

de Linage, C., Rivera, L., Hinderer, J., Boy, J. P., Rogister, Y., Lambotte, S. and Biancale, R. (2009), 'Separation of coseismic and postseismic gravity changes for the 2004 Sumatra Andaman earthquake from 4.6 yr of GRACE observations and modelling of the coseismic change by normal-modes summation', *Geophysical Journal International* **176**(176), 659 – 714.

de Viron, O., Panet, I., Mikhailov, V., Van Camp, M. and Diament, M. (2008), 'Retrieving earthquake signature in grace gravity solutions', *Geophysical Journal International* **174**(1), 14 – 20.

DeMets, C., Gordon, R. G., Argus, D. F. and Stein, S. (1994), 'Effect of recent revisions to the geomagnetic reversal time scale on estimates of current plate motions', *Geophysical Research Letters* **21**(20), 2191 – 2194.

Devaraju, B. and Sneeuw, N. (2009), Performance analysis of isotropic spherical harmonic spectral windows. VII Hotine-Marussi Symposium on Theoretical Geodesy, Rome, Italy (6.-10.7.) (Poster).

Drinkwater, M. R., Haagmans, R., Muzi, D., Popescu, A., Floberghagen, R., Kern, M. and Fehringer, M. (2007), The GOCE Gravity Mission: ESA´s First Core Earth Explorer. Proceedings of the 3rd International GOCE User Workshop, 6-8 November, 2006, Frascati, Italy, ESA Special Publication, SP-627, ISBN 92-9092-938-3.

Dunn, C., Bertiger, W., Franklin, G., Harris, I., Kruizinga, G., Meehan, T., Nguyen, D., Nandi, S., Rogstad, T., Thomas, B. and Tien, J. (2002), The Instrument on NASA's GRACE Mission:augmentation of GPS to achieve unprecendentedgravity field measurements, ION GPS, Portland, OR - Sept. 25, presentation.

Dziewonski, A. and Anderson, D. L. (1981), 'Preliminary reference Earth model', *Physics of the Earth and Planetary Interiors* **25**, 297 – 356.

Einarsson, I., Hoechner, A., Wang, R. and Kusche, J. (2010), 'Gravity changes due to the Sumatra-Andaman and Nias earthquakes as detected by the GRACE satellites: a reexamination', *Geophysical Journal International* **183**(2), 733 – 747.

Ellsaesser, H. W. (1966), 'Expansion of Hemispheric Meteorological Data in Antisymmetric Surface Spherical Harmonic (Laplace) Series', *Journal of Applied Meteorology and Climatology* **5**(3), 263 – 276.

Farrel, W. E. (1972), 'Deformation of the Earth by Surface Loads', *Reviews of Geophysics and Spacephysics* **10**(3), 761 – 797.

Flechtner, F. (2007), GRACE GFZ Level-2 Processing Standards Document For Level-2 Product Release 0004, Technical report, GeoForschungszentrum Potsdam, Department 1: Geodesy and Remote Sensing.

Frohlich, C. (2006), *Deep Earthquakes*, Cambridge. ISBN:9780521828697.

Gauss, C. F. (1939), 'Allgemeine Theorie des Erdmagnetismus, in Resultate aus den Beobachtungen des Magnetkchen Vereins im Jahre 1838', **5**, 121 – 193.

Gross, R. S. (2003), CHAMP, mass displacements, and the Earth's rotation in First CHAMP Mission Results for Gravity, Magnetic and Atmospheric Studies, Springer-Verlag, New York., pp. 174–179.

Gross, R. S., Lavallée, D. A., Blewitt, G. and Clarke, P. J. (2008), Consistency of Earth Rotation, Gravity, and Shape Measurements, *in* M. G. Sideris and M. G. Sideris, eds, 'Observing our Changing Earth', Vol. 133 of *International Association of Geodesy Symposia*, Springer Berlin Heidelberg, pp. 463 – 471.

Han, D. and Wahr, J. (1995), 'The viscoelastic relaxation of the realistically stratified earth and a further analysis of postglacial rebound', *Geophysical Journal International* **120**, 287 – 311.

Han, S. C. and Ditmar, P. (2007), 'Localized spectral analysis of global satellite gravity fields for recovering time-variable mass redistributions', *Journal of Geodesy* **82**, 423 – 430.

Han, S. C., Sauber, J. and Luthcke, S. (2010), 'Regional gravity decrease after the 2010 Maule (Chile) earthquake indicates large-scale mass redistribution', *Geophysical Research Letters* **37**(23), L23307.

Han, S. C., Sauber, J., Luthcke, S. B., Ji, C. and Pollitz, F. (2008), 'Implications of postseismic gravity change following the great 2004 Sumatra-Andaman earthquake from the regional harmonic analysis of GRACE intersatellite tracking data', *Journal of Geophysical Research* **113**, B11413.

Han, S. C., Shum, C. K., Bevis, M., Ji, C. and Kuo, C. Y. (2006), 'Crustal Dilatation Observed by GRACE After the 2004 Sumatra-Andaman Earthquake', *Science* **313**(658), 658 – 662.

Han, S. C., Shum, C. K., Jekeli, C., Kuo, C. Y., Wilson, C. and Seo, K. W. (2005), 'Non-isotropic filtering of GRACE temporal gravity for geophysical signal enhancement', *Geophysical Journal International* **163**(1), 18 – 25.

Heki, K. and Matsuo, K. (2010*a*), 'Coseismic gravity changes by the 2010 Chile earthquake: separating hydrological and tectonic signals in GRACE data'. presentation.

Heki, K. and Matsuo, K. (2010*b*), 'Coseismic gravity changes of the 2010 earthquake in central Chile from satellite gravimetry', *Geophysical Research Letters* **37**(24), L24306.

Helmert, F. R. (1880), *Die mathematischen und physikalischen Theorieen der höheren Geodäsie*, Vol. 1, Teubner, Leipzig.

Hoffmann-Wellenhof, B. and Moritz, H. (2005), *Physical Geodesy*, Springer-Verlag, Wien.

Ilk, K. H., Flury, J., Rummel, R., Schwintzer, P., Bosch, W., Haas, C., Schröter, J., Stammer, D., Zahel, W., Miller, H., Dietrich, R., Huybrechts, P., Schmeling, H., Wolf, D., Götze, H. J.,

Riegger, J., Bardossy, A., Güntner, A. and Gruber, T. (2005), Mass Transport and Mass Distribution in the Earth System, Technical report.

Jekeli, C. (1981), Alternative Methods to Smooth the Earth's Gravity Field, Technical report, Ohio State University.

Jekeli, C. (1999), 'The determination of gravitational potential differences from satellite-to-satellite tracking', *Celestial Mechanics and Dynamical Astronomy* **75**.

Jónsson, S., Segall, P., Pendersen, R. and Björnsson, G. (2003), 'Post-earthquake ground movements correlated to pore-pressure transients', *Nature* **424**, 179 –183.

Klees, R., Revtova, E. A., Gunter, B. C., Ditmar, P., Oudman, E., Winsemius, H. C. and Savenije, H. H. G. (2008), 'The design of an optimal filter for monthly GRACE gravity models', *Journal of Geophysics* **175**, 417 – 432.

Knudsen, P. (2003), 'Ocean tides in GRACE monthly averaged gravity fields', *Space Science Reviews* **108**(1 – 2), 261 – 270.

Knudsen, P. and Andersen, O. (2002), 'Correcting GRACE gravity fields for ocean tide effects', *Geophysical Research Letters* **29**(8), 1178.

Kusche, J. (2007), 'Approximate decorrelation and non-isotropic smoothing of time-variable GRACE-type gravity field models', *Journal of Geodesy* **81**, 733 – 749.

Liu, X. (2008), Global gravity field recovery from satellite-to-satellite tracking data with the acceleration approach, PhD thesis, Delft Institute of Earth Observation and Space Systems, Delft University of Technology.

Lorenz, C. (2009), Applying stochastic constraints on time-variable GRACE data, Master's thesis, Universität Stuttgart.

Lund, R. and Reeves, J. (2002), 'Detection of Undocumented Changepoints: A Revision of the Two-Phase Regression Model', *Journal of Climate* **15**, 2547 – 2554.

Lund, R., Wang, X. L., Lu, Q. Q., Reeves, J., Gallagher, C. and Feng, Y. (2007), 'Changepoint Detection in Periodic and Autocorrelated Time Series', *Journal of Climate* **20**, 5178 — 5190.

Manias, E. (2011), MatSE447 Rheology & Processing, Technical report, Polymer Nanostructures Lab, Pennsylvania State University. Lecture Notes.

Matsuo, K. and Heki, K. (2010), 'Time-variable ice loss in Asian high mountains from satellite gravimetry', *Earth and Planetary Science Letters* **290**(1 – 2), 30 – 36.

Matsuo, K. and Heki, K. (2011), 'Coseismic gravity changes of the 2011 Tohoku-Oki earthquake from satellite gravimetry', *Geophysical Research Letters* **38**, L00G12.

Mayer-Gürr, T. (2006), Gravitationsfeldbestimmung aus der Analyse kurzer Bahnbögen am Beispiel der Satellitenmissionen CHAMP und GRACE, PhD thesis, Universität Bonn.

McCaffrey, R. (2009), 'The Tectonic Framework of the Sumatran Subduction Zone', *Annual Review of Earth and Planetary Sciences* **37**(1), 345 – 366.

McCaughey, J., Tapponnier, P., Sieh, K., Descatoire, Y., Sang, L. H. and Tapponnier, P. (2011), The great East Japan (Tohoku) 2011 earthquake: Important lessons from old dirt, Technical report, Earth Observatory of Singapore.

Meissl, P. A. (1971), A study of covariance functions related to the earth's disturbing potential, Technical Report 151, Department of Geodetic Science, The Ohio State Univerisity.

Melini, D., Spada, G. and Piersanti, A. (2010), 'A sea level equation for the seismic perturbations', *Geophysical Journal International* **180**, 88 –100.

MIT (n.d.), 'Earthquake near Wenchuan,West Sichuan, China, 2008 May 12 06:28:01 UTC; Magnitude 7.9'.

Moritz, H. (2010), Classical Physical Geodesy, *in* W. Freeden, M. Z. Nashed and T. Sonar, eds, 'Handbook of Geomathematics', Springer Berlin Heidelberg, pp. 125–158.

Nerem, R. S., Eanes, R. J., Thompson, P. F. and Chen, J. L. (2000), 'Observations of annual variations of the Earth's gravitational field using satellite laser ranging and geophysical models.', *Geophysical Research Letters* **27**(12), 1783 – 1786.

Ogawa, R. and Heki, K. (2007), 'Slow Postseismic Recovery of Geoid Depression formed by the 2004 Sumatra-Andaman Earthquake by Mantle Water Diffusion', *Geophysical Research Letters* **34**, L06313.

Ozawa, S., Nishimura, T., Suito, H., Kobayashi, T., Tobita, M. and Imakiire, T. (2011), 'Coseismic and postseismic slip of the 2011 magnitude-9 Tohoku-Oki earthquake', *Nature* **475**, 373 – 376.

Panet, I., Mikhailov, V., Diament, M., Pollitz, F., King, G., de Viron, O., Holschneider, M., Biancale, R. and Lemoine, J. M. (2007), 'Coseismic and post-seismic signatures of the Sumatra 2004 December and 2005 March earthquakes in GRACE satellite gravity', *Geophysical Journal International* **171**, 177 – 190.

Panet, I., Pollitz, F., Mikhailov, V., Diament, M., Banerjee, P. and Grijalva, K. (2010), 'Upper mantle rheology from GRACE and GPS postseismic deformation after the 2004 Sumatra-Andaman earthquake', *Geochemistry Geophysics Geosystems* **11**(6), Q06008.

Reubelt, T., Austen, G. and Grafarend, E. W. (2003), 'Harmonic analysis of the Earth's gravitational field by means of semi-continuous ephemerides of a low Earth orbiting GPS-tracked satellite. Case study: CHAMP', *Journal of Geodesy* **77**, 257 – 278.

Robert, A., Zhu, J., Vergne, J., Cattin, R., Chan, L. S., Wittlinger, G., Herquel, G., de Sigoyer, J., Pubellier, M. and Zhu, L. D. (2010), 'Crustal structures in the area of the 2008 Sichuan earthquake from seismologic and gravimetric data', *Tectonophysics* **491**, 205 – 210.

Rodell, M., Houser, P. R., Jambor, U., Gottschalck, J., Mitchell, K., Meng, C. J., Arsenault, K., Cosgrove, B., Radakovich, J., Bosilovich, M., Entin, J. K., Walker, J. P., Lohmann, D., and Toll, D. (2004), 'The Global Land Data Assimilation System', *Bulletin of the American Meteorological Society* **85**, 381 – 394.

Rowlands, D. D., Luthcke, S. B., Klosko, S. M., Lemoine, F. G. R., Chinn, D. S., McCarthy, J. J., Cox, C. M., and Anderson, O. B. (2005), 'Resolving mass flux at high spatial and temporal resolution using GRACE intersatellite measurements', *Geophysical Research Letters* **32**, L04310.

Rummel, R. and van Gelderen, M. (1995), 'Meissl scheme - spectral characteristics of physical geodesy', *manuscripta geodaetica* **20**, 379 – 385.

Sato, M., Ishikawa, T., Ujihara, N., Yoshida, S., Fujita, M., Mochizuki, M. and Asada, A. (2011), 'Displacement Above the Hypocenter of the 2011 Tohoku-Oki Earthquake', *Science* **332**(6036), 1395.

Schmidt, R., Wang, R. and Kusche, J. (2007), Detection of the gravity changes induced by the sumatra-andaman earthquake using grace gfz-rl04 data. GSTM+DFG-SPP Symposium, Oct 15-17, 2007, Potsdam/Germany.

Seber, G. A. F. and Wild, C. J. (2003), *Nonlinear Regression*, Hoboken, NJ: Wiley-Interscience.

Shen-Tu, B. and Mahdyiar, M. (2011), Earthquake Risk in Chile after February 2010, Technical report, AIR Worldwide.

Sieh, K., Natawidjaja, D. H., Meltzner, A. J., Shen, C. C., Chen, H., Li, K. S., Suwargadi, B. W., Galetzka, J., Philibosian, B. and Edwards, R. L. (2008), 'Earthquake Supercycles Inferred from Sea-Level Changes Recorded in the Corals of West Sumatra', *Science* **322**(5908), 1674 – 1678.

Sneeuw, N. (1994), 'Global spherical harmonic analysis by least-squares and numerical quadrature methods in historical perspective', *Geophysical Journal International* **118**, 707 – 716.

Sneeuw, N. (1999), Storage formats of SH-coefficients in MATLAB, Technical report, Institut für Astronomische und Physikalische Geodäsie, Technische Universität München.

Sneeuw, N. (2000), A Seimi-Analytical Approach to Gravity Field Analysis for Satellite Observations, PhD thesis, Institut fürAstronomische und Physikalische Geodäsie, Technische Universität München.

Sneeuw, N. (2006), Physical Geodesy, Technical report, Geodätisches Institut, Universität Stuttgart. Lecture Notes.

Sneeuw, N. and Bun, R. (1996), 'Global Spherical Harmonic Computation by two-dimensional Fourier Method', *Journal of Geodesy* **70**, 224 – 232.

Sneeuw, N. and Krumm, F. (2008), Adjustment Theory, Technical report, Geodätisches Institut, Universität Stuttgart. Lecture Notes.

Stein, S. and Wysession, M. (2003), *An Introduction to Seismology, Earthquakes, and Earth Structure*, Blackwell Publishing.

Sun, W. and Okubo, S. (1993), 'Surface potential and gravity changes due to internal dislocations in a spherical earth - I. Theory for a point dislocation', *Geophysical Journal International* **114**(3), 569 – 592.

Sun, W. and Okubo, S. (2004), 'Coseismic deformations detectable by satellite gravity missions: A case study of Alaska (1964, 2002) and Hokkaido (2003) earthquakes in the spectral domain', *Journal of Geophysical Research* **109**, B04405.

Swenson, S. and Wahr, J. (2006), 'Post-processing removal of correlated errors in GRACE data', *Geophysical Research Letters* **33**, L08402.

Tapley, B. D., Bettadpur, S., Ries, J. C., Thompson, P. F. and Watkins, M. M. (2004), 'GRACE Measurements of Mass Variability in the Earth System', *Science* **305**, 503 – 506.

Tarantola, A. (2005), *Inverse Problem Theory And Methods For Model Parameter Estimation*, Society for Industrial and Applied Mathematics.

The Development of the Joint NASA GSFC and NIMA Geopotential Model EGM96 (1998). NASA Goddard Space Flight Center, Greenbelt, Maryland, 20771 USA, July 1998.

Vautard, R., Yiou, P. and Ghil, M. (1992), 'Singular-spectrum analysis: A toolkit for short, noisy chaotic signals', *Physica D: Nonlinear Phenomena* **58**(1 – 4), 95 – 126.

Vigny, C., Socquet, A., Peyrat, S., Ruegg, J. C., Métois, M., Madariaga, R., Morvan, S., Lancieri, M., Lacassin, R., Campos, J., Carrizo, D., Bejar-Pizarro, M., Barrientos, S., Armijo, R., Aranda, C., Valderas-Bermejo, M. C., Ortega, I., Bondoux, F., Baize, S., Lyon-Caen, H., Pavez, A., Vilotte, J. P., Bevis, M., Brooks, B., Smalley, R., Parra, H., Baez, J. C., Blanco, M., Cimbaro, S. and Kendrick, E. (2011), 'The 2010 Mw 8.8 Maule Mega-Thrust Earthquake of Central Chile, Monitored by GPS.', *Science* **1417**(2011), 1417 – 1421.

Visser, P., Sneeuw, N., Reubelt, T., Losch, M. and Dam, T. V. (2010), 'Space-borne gravimetric satellite constellations and ocean tides : aliasing effects', *Geophysical Journal International* **181**(2), 789 – 805.

Wahr, J. (1996), Geodesy and Gravity, Technical report, Department of Physics, University of Colorado. Lecture Notes.

Wahr, J. and Molenaar, M. (1998), 'Time Variability of the Earth's Gravity Field: Hydrological and Oceanic Effects and Their Possible Detection Using GRACE', *Journal of Geophysical Research* **103**(B12), 30205 – 30229.

Wahr, J., Swenson, S. and Velicogna, I. (2006), 'Accuracy of GRACE mass estimates', *Geophysical Research Letters* **33**, L06401.

Wang, W., Sun, W. and Jiang, Z. (2010), 'Comparison of fault models of the 2008 Wenchuan earthquake (Ms8.0) and spatial distributions of co-seismic deformations', *Tectonophysics* **491**(1 – 4), 85 – 95.

Warren, C. R. and Sudgen, D. E. (1993), 'The Patagonia Icefields: A glaciological review', *Arctic and Alpine Research* **25**(4), 316 – 331.

Watkins, M. M. and Yuan, D. N. (2007), GRACE JPL Level-2 Processing Standards Document For Level-2 Product Release 04, Technical report, JPL.

Wiseman, K., Banerjee, P., Sieh, K., Bürgmann, R. and Natawidjaja, D. H. (2011), 'Aother potential source of destructive earthquakes and tsunami offshore of Sumatra', *Geophysical Research Letters* **38**, L10311.

Wouters, B. and Schrama, E. J. O. (2007), 'Improved accuracy of GRACE gravity solutions through empirical orthogonal function filtering of spherical harmonics', *Geophysical Research Letters* **34**, L23711.

Zakharenkova, I., Shagimuratov, I., Tepenitzina, N. and Krankowski, A. (2008), 'Anomalous modification of the ionospheric total electron content prior to the 26 September 2005 Peru earthquake', *Journal of Atmospheric and Solar-Terrestrial Physics* **70**(15), 1919 – 1928.

Zhang, P. Z., Wen, X. Z., Shen, Z. K. and Chen, J. H. (2010), 'Oblique, High-Angle, Listric-Reverse Faulting and Associated Development of Strain: The Wenchuan Earthquake of May 12, 2008, Sichuan, China', *Annual Review of Earth and Planetary Sciences* **38**(1), 353 – 382.

Zhang, Z. Z., Chao, B. F., Lu, Y. and Hsu, H. T. (2009), 'An effective filtering for GRACE time-variable gravity: Fan filter', *Geophysical Research Letters* **36**, L17311.

Appendix A

Spherical Harmonics

A.1 Solve Laplace Equation

We begin without proving that the gravity potential outside the earth is the solution of the Laplace's equation which is the Eq. (3.1) in Chapter 3. And we begin to solve the Laplace's equation in the spherical coordinate and for the solution in the Cartesian coordinate please see (Hoffmann-Wellenhof and Moritz, 2005; Sneeuw, 2006).

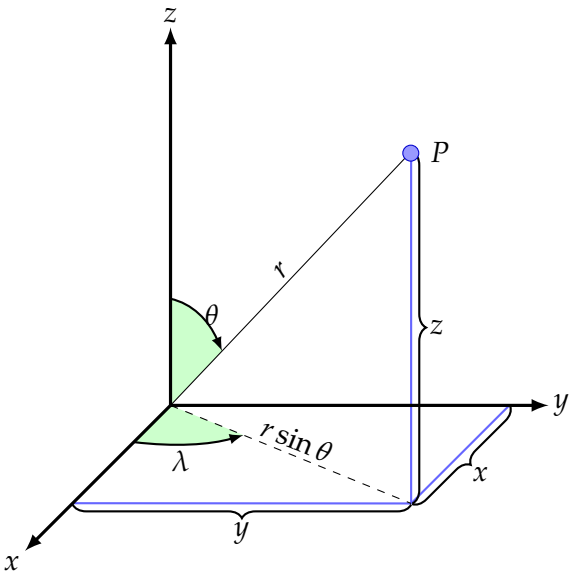

Figure A.1: *Spherical and Rectangular Coordinates*

where the x, y, z are the coordinates in the Cartesian coordinate and r (radius), λ (longitude), θ (co-latitude) and the relationship between this two coordinate system is

$$\begin{aligned} x &= r\sin\theta\cos\lambda, \\ y &= r\sin\theta\sin\lambda, \\ z &= r\cos\theta. \end{aligned} \tag{A.1}$$

The gradient in the spherical coordinate is:

$$\nabla = \frac{\partial}{\partial r}\mathbf{e_r} + \frac{1}{r}\frac{\partial}{\partial\theta}\mathbf{e_\theta} + \frac{1}{r\sin\theta}\frac{\partial}{\partial\lambda}\mathbf{e_\lambda} \tag{A.2}$$

As for an arbitrary vector field $\mathbf{v} = A\mathbf{e_r} + B\mathbf{e_\theta} + C\mathbf{e_\lambda}$, the divergence of $\mathbf{v}$ in spherical coordinate is:

$$\nabla \cdot \mathbf{v}(r,\theta,\lambda) = \frac{1}{r^2}\left(r^2 A\right)_r + \frac{1}{r\sin\theta}\left(\sin\theta B\right)_\theta + \frac{1}{r\sin\theta}C_\lambda \tag{A.3}$$

Combining Eq. (A.2) and (A.3):

$$\begin{aligned}\Delta V &= \nabla \cdot \nabla V \\ &= \frac{\partial^2 V}{\partial r^2} + \frac{2}{r}\frac{\partial V}{\partial r} + \frac{1}{r^2}\frac{\partial^2 V}{\partial \theta^2} + \frac{\cot\theta}{r^2}\frac{\partial V}{\partial \theta} + \frac{1}{r^2\sin^2\theta}\frac{\partial^2 V}{\partial \lambda^2}\end{aligned} \tag{A.4}$$

using the Eq. (3.1)

$$r^2\frac{\partial^2 V}{\partial r^2} + 2r\frac{\partial V}{\partial r} + \frac{\partial^2 V}{\partial \theta^2} + \cot\theta\frac{\partial V}{\partial \theta} + \frac{1}{\sin^2\theta}\frac{\partial^2 V}{\partial \lambda^2} = 0 \tag{A.5}$$

Then solve the equation by the method of separation of variables.

Step 1: separate r, let

$$V(r,\theta,\lambda) = f(r)\,Y(\theta,\lambda) \tag{A.6}$$

insert Eq. (A.6) into (A.5) and divided by fY

$$\frac{1}{f}\left(r^2 f'' + 2rf'\right) = -\frac{1}{Y}\Delta_S Y \tag{A.7}$$

where

$$\Delta_S Y = \frac{\partial^2 Y}{\partial \theta^2} + \cot\frac{\partial Y}{\partial \theta} + \frac{1}{\sin^2\theta}\frac{\partial^2 Y}{\partial \lambda^2} \tag{A.8}$$

is the surface Laplace operator or Beltrami operator.

As in the Eq. (A.7), the left-hand side depends only on r and the right-hand side depends only on θ and λ, both sides must be constant. And the guess by the mathematicians is $l(l+1)$ and l must be integer number (0,1,...). Then we have the differential equation:

$$r^2 f'' + 2rf' - l(l+1)f = 0 \tag{A.9}$$

and the solution is

$$f_1(r) = r^{-(l+1)} \quad \text{and} \quad f_2(r) = r^l \tag{A.10}$$

and assume that the solution of the Eq. (A.7) on the right-hand side is $Y_l(\theta,\lambda)$ so the solution is

$$V_1(r) = r^{-(l+1)}Y_l(\theta,\lambda) \quad \text{and} \quad V_1(r) = r^l Y_l(\theta,\lambda) \tag{A.11}$$

and the functions are called *solid spherical harmonics* and the function $Y_l(\theta,\lambda)$ are *surfaces spherical harmonics*.

Step 2 is to separate θ and λ.

$$Y_l(\theta,\lambda) = g(\theta)\,h(\lambda) \tag{A.12}$$

insert the Eq. (A.12) into (A.7) $= l(l+1)$

$$\frac{\sin\theta}{g}\left(\sin\theta g'' + \cos\theta g' + l(l+1)\sin\theta g\right) = -\frac{h''}{h} \tag{A.13}$$

it is the same with Eq. (A.7) that the left-hand side depends only on θ and the right-hand side depends only on λ, both sides must be constant again. And the guess by the mathematician is m^2. On the right the differential equation is

$$h''(\lambda) + m^2 h(\lambda) = 0 \tag{A.14}$$

and the solution is

$$h_1(\lambda) = \cos m\lambda \quad \text{and} \quad h_2(\lambda) = \sin m\lambda \tag{A.15}$$

and on the left of Eq. (A.13) is

$$\sin\theta g''(\theta) + \cos\theta g'(\theta) + \left(l(l+1)\sin\theta - \frac{m^2}{\sin\theta}\right) g(\theta) = 0 \tag{A.16}$$

the property of the Eq. (A.16) cannot be seen directly, we expressed it in a different way:

$$\left(1-\cos^2\theta\right) g''(\cos\theta) - 2\cos\theta g'(\cos\theta) + \left(l(l+1) - \frac{m^2}{1-\cos^2\theta}\right) g(\cos\theta) = 0 \tag{A.17}$$

and from the advanced mathematics we known that the Eq. (A.17) is the general form of the *associated Legendre differential equation* with unknown $\cos\theta$. We can solve the equation by the means of series expansion. And the solution is

$$g_1(\theta) = P_{lm}(\cos\theta) \quad \text{and} \quad g_2(\theta) = Q_{lm}(\cos\theta) \tag{A.18}$$

P_{lm} is the associated Legendre function of the 1^{st} kind and Q_{lm} is the 2^{nd} kind. Then the Y_{lm} can be expressed

$$Y_{lm}(\theta,\lambda) = P_{lm}(\cos\theta) \left\{ \begin{array}{c} \cos m\lambda \\ \sin m\lambda \end{array} \right\} \tag{A.19}$$

which is the similar with the Eq. (3.36) which is normalized form.

The general solution of the Eq. (A.5) can be expressed by combining the Eq. (A.10), (A.15) and (A.18):

$$\left\{ \begin{array}{c} r^{-l(l+1)} \\ r^l \end{array} \right\} P_{lm}(\cos\theta) \left\{ \begin{array}{c} \cos m\lambda \\ \sin m\lambda \end{array} \right\} \tag{A.20}$$

Note that Q_{lm} are infinite at the poles and it is the reason to discard it right away. Considering the boundary conditions, the first is the regularity condition:

$$\lim_{r\to\infty} V(r,\theta,\lambda) = 0 \tag{A.21}$$

the term r^l vanishes. And for the Dirichlet boundary condition by assuming the value on the surface ($r = R$) is know:

$$V(r,\theta,\lambda) = \sum_{l=0}^{\infty} \left(\frac{R}{r}\right)^{l+1} \sum_{m=0}^{l} P_{lm}(\cos\theta)\left(C_{lm}\cos m\lambda + S_{lm}\sin m\lambda\right) \tag{A.22}$$

which is the general solution of the Laplace equation on the sphere without dimension.

Similar to the Fourier transform that any function can be expressed to the combination of the coss and sins, the Legendre transform which is the expansion by the spherical harmonics means any function on the sphere can be expressed to the combination of the Y_{lm}s which are P_{lm} coss and P_{lm} sins.

A.2 Important Properties of the Base Function

And the Y_{lm} is the base function and it is necessary to know the properties of this function which can be found in (Wahr, 1996).

Parity

$$Y_{lm}(\pi - \theta, \lambda + \pi) = (-1)^l Y_{lm}(\theta, \lambda) \tag{A.23}$$

Recursion Relations of the P_{lm}

$$(2l+1)\, xP_{lm}(x) = (l+1-m)\, P_{(L+1)m}(x) + (l+m)\, P_{(l-1)m}(x) \tag{A.24}$$

and

$$\left(1-x^2\right) \partial P_{lm} = -lxP_{lm} + (l+m)\, P_{(l-1)m} \tag{A.25}$$

Orthogonality

$$\int_0^{2\pi} \int_0^{\pi} Y_{lm}(\theta, \lambda)\, Y^*_{l'm'}(\theta, \lambda) \sin\theta \, \mathrm{d}\theta \, \mathrm{d}\lambda = \delta_{ll'}\delta_{mm'} \tag{A.26}$$

where δ is the delta function that only if $l = l'$ $\delta_{ll'} = 1$ otherwise $\delta_{ll} = 0$.

Completeness the property of completeness can be seen in the Eq. (3.7).

Appendix B

Empirical Orthogonal Functions (EOF) Example

To better understand the meaning of EOF, a very simple example for which the eigenvalues can be easily computed will help demonstrate the EOF process:

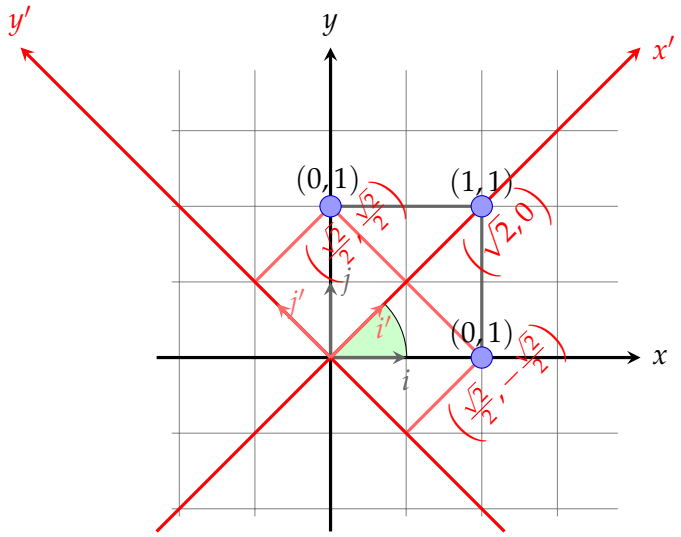

Figure B.1: *Simple Example of EOF Analysis*

See from Fig. B.1 three points are for EOF analysis:$(1,1)$, $(1,0)$, $(0,1)$ and write in the matrix form:

$$K = \begin{pmatrix} 1 & 1 \\ 1 & 0 \\ 0 & 1 \end{pmatrix}$$

by using SVD which will be discussed later, we get the square root of eigenvalues and normalized eigenvectors of $K^T K = \begin{pmatrix} 2 & 1 \\ 1 & 2 \end{pmatrix}$:

$$\Sigma = \begin{pmatrix} \sqrt{3} & 0 \\ 0 & 1 \\ 0 & 0 \end{pmatrix}, D = \begin{pmatrix} \frac{\sqrt{2}}{2} & \frac{\sqrt{2}}{2} \\ \frac{\sqrt{2}}{2} & -\frac{\sqrt{2}}{2} \end{pmatrix}$$

and the eigenvalues of KK^T are identical to those of K^TK but with one more which is 0 due to the rank deficiency and corresponding normalized eigenvectors are:

$$Z = \begin{pmatrix} \frac{\sqrt{6}}{3} & 0 & -\frac{\sqrt{3}}{3} \\ \frac{\sqrt{6}}{6} & \frac{\sqrt{2}}{2} & \frac{\sqrt{3}}{3} \\ \frac{\sqrt{6}}{6} & -\frac{\sqrt{2}}{2} & \frac{\sqrt{3}}{3} \end{pmatrix}$$

So the SVD decomposition is:

$$\begin{pmatrix} 1 & 1 \\ 1 & 0 \\ 0 & 1 \end{pmatrix} = \begin{pmatrix} \frac{\sqrt{6}}{3} & 0 & -\frac{\sqrt{1}}{3} \\ \frac{\sqrt{6}}{6} & \frac{\sqrt{2}}{2} & \frac{\sqrt{1}}{3} \\ \frac{\sqrt{6}}{6} & -\frac{\sqrt{2}}{2} & \frac{\sqrt{1}}{3} \end{pmatrix} \begin{pmatrix} \sqrt{3} & 0 \\ 0 & 1 \\ 0 & 0 \end{pmatrix} \begin{pmatrix} \frac{\sqrt{2}}{2} & \frac{\sqrt{2}}{2} \\ \frac{\sqrt{2}}{2} & -\frac{\sqrt{2}}{2} \end{pmatrix}$$

We get a new base function from matrix D which is $\mathbf{i}_n = \begin{pmatrix} \frac{\sqrt{2}}{2} \\ \frac{\sqrt{2}}{2} \end{pmatrix}$ and $\mathbf{j}_n = \begin{pmatrix} \frac{\sqrt{2}}{2} \\ -\frac{\sqrt{2}}{2} \end{pmatrix}$ and the corresponding coefficients of the new bases are got from $K \times d_i$ and d_i is the ith column of D and expressed in matrix form:

$$\begin{pmatrix} 1 & 1 \\ 1 & 0 \\ 0 & 1 \end{pmatrix} = \begin{pmatrix} \sqrt{2} \\ \frac{\sqrt{2}}{2} \\ \frac{\sqrt{2}}{2} \end{pmatrix} \mathbf{i}_n^T + \begin{pmatrix} 0 \\ -\frac{\sqrt{2}}{2} \\ \frac{\sqrt{2}}{2} \end{pmatrix} \mathbf{j}_n^T = \begin{pmatrix} 1 \\ 1 \\ 0 \end{pmatrix} \begin{pmatrix} 1 \\ 0 \end{pmatrix}^T + \begin{pmatrix} 1 \\ 0 \\ 1 \end{pmatrix} \begin{pmatrix} 0 \\ 1 \end{pmatrix}^T$$

One question should be raised: what are the advantages of the new bases? In the former coordinate the position of the points are $\begin{pmatrix} 1 & 1 \\ 1 & 0 \\ 0 & 1 \end{pmatrix}$ and in the new one are $\begin{pmatrix} \sqrt{2} & 0 \\ \frac{\sqrt{2}}{2} & -\frac{\sqrt{2}}{2} \\ \frac{\sqrt{2}}{2} & \frac{\sqrt{2}}{2} \end{pmatrix}$ the correlation is defined as

$$c_{X,Y} = \operatorname{corr}(X, Y) = \frac{\operatorname{cov}(X, Y)}{\sigma_X \sigma_Y} = \frac{\mathbf{E}\left[(X - \mathbf{E}X)\left(Y - \mathbf{E}Y\right)\right]}{\sigma_X \sigma_Y} \tag{B.1}$$

and $\mathbf{E}X = \frac{1}{n} \sum_{i=1}^{n} X_i$.

First, $\sigma_{X_o} = 2$ and $\sigma_{Y_o} = 2$ and $\sigma_{X_n} = 3$ and $\sigma_{Y_n} = 1$ as the trace of the same matrix is the same all the time, so the new bases move the biggest variance to the first axis compared to the old axes.

Second, $\operatorname{cov}_o = \frac{1}{9}$ and $\operatorname{cov}_n = 0$ and the corresponding $c_o \neq 0$ and $c_n = 0$ which is another property of the EOF analysis that the correlation of the coefficients vanished. In the $2D$ case, it is easy to visualize but in the higher dimension only the theoretical discussion is possible.

Appendix C

Storage and Computational Format of Spherical Harmonics

To process the data in Matlab© the convention of the spherical harmonics coefficient is defined in (Sneeuw, 1999).

C.1 CS Format

The CS format is the storage format, the size of the matrix is $(L+1)^2$ where L is the maximum degree. And the reason for the name CS is the C_{lm}s are stored at the lower left corner and the S_{lm}s are at the upper right corner. Here is a figure to illustrate the CS format.

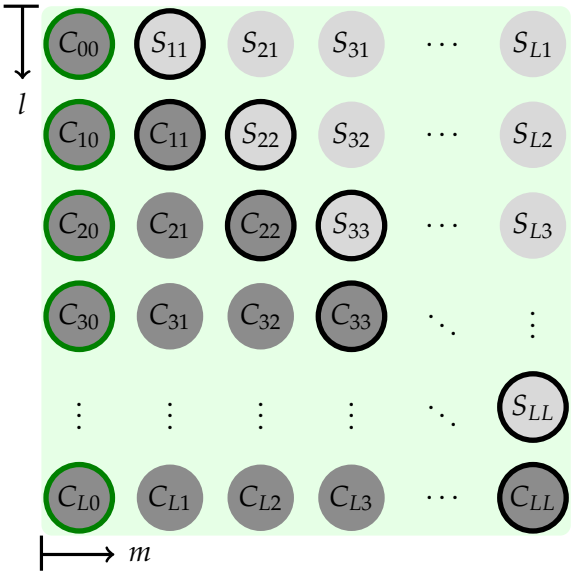

Figure C.1: *CS Format*

C.2 SC Format

Compare to the CS format, the SC format needs more space for the storage but easy to deal with. SC format is a $(L+1) \times (2L+1)$. The upper left corners and right corners are filled with ϵ instead of 0 for a practical consideration, for example when compute the SNR. ϵ is a small number such as 10^{-20}. The name for the SC format is that the S_{lm}s are on the left hand side and the C_{lm}s are on the right hand side.

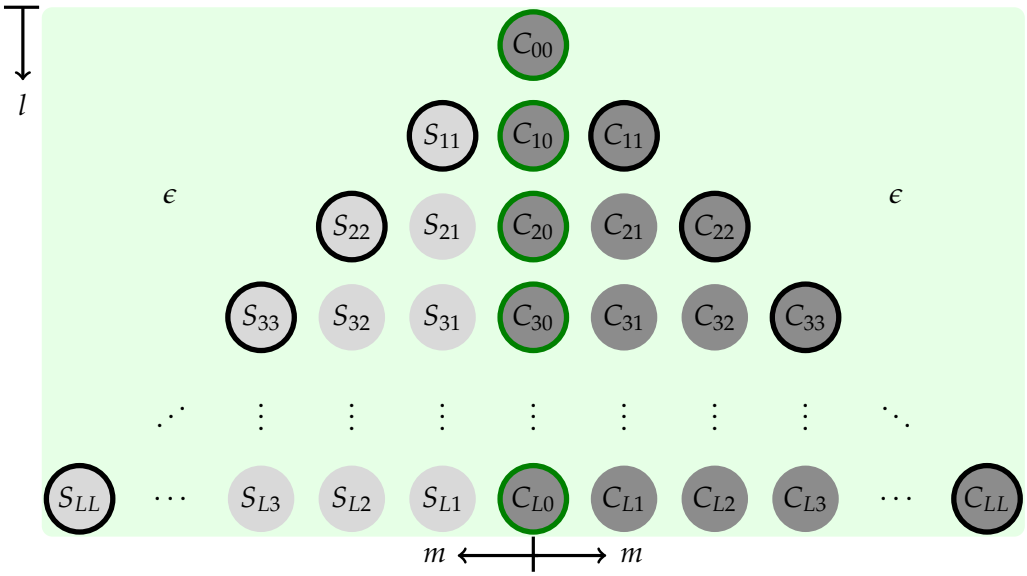

Figure C.2: *SC Format*

The Matlab© code for converting between the SC and CS format can be found in (Sneeuw, 1999).

C.3 Degree Ordering

Comparing to the CS and SC format, the degree ordering is not so "visible". In some case, such as the error analysis of the GRACE (Section. 3.6), the degree ordering is needed. The relationship between the degree ordering and the SC format is shown in the Fig. C.3.

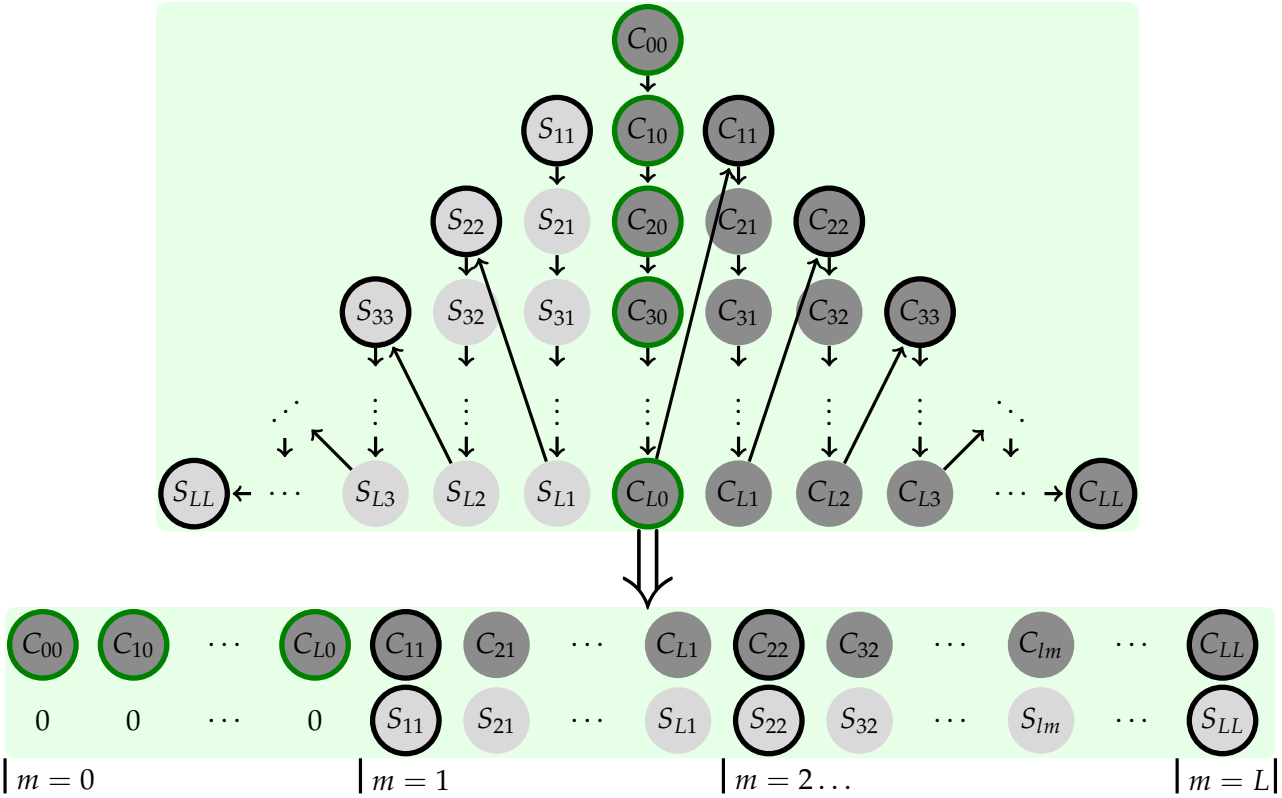

Figure C.3: *Degree Ordering*

The function for the converting from the SC format to the degree ordering without considering about the computing time is below:

```
function DegOrd=sc2DegOrd(field)
% sc2DegOrd(FIELD) converts the rectangular (L+1)x(2L+1) matrix FIELD, containing
%                  spherical harmonics coefficients in /S|C\ storage format into
%                                  a 2x(L+1)(L+2)/2 matrix.
%
% Zhou CAO, Stuttgart, 2011
    [rows,cols] = size(field);
    lmax = rows -1;
    if cols ~= 2*lmax+1, error ('Matrix dimensions must be (L+1)x(2L+1).'), end

    c=field(:,lmax+1)';% m=0 Cl0
    for m=1:lmax % m>0
        c(((2*lmax+3-m)/2*m+1):((2*lmax+3-m)/2*m+1+lmax-m)) = field(m+1:end,lmax+1+m)';%Clm
        s(((2*lmax+3-m)/2*m+1):((2*lmax+3-m)/2*m+1+lmax-m)) = field(m+1:end,lmax+1-m)';%Slm
    end
    DegOrd=[c;s];
end
```

However, properly divide the degree ordering matrix into small pieces can save the computing time.

Appendix D

Additional Figures

D.1 Sumatra-Andaman Earthquake (Indonesia) 2004

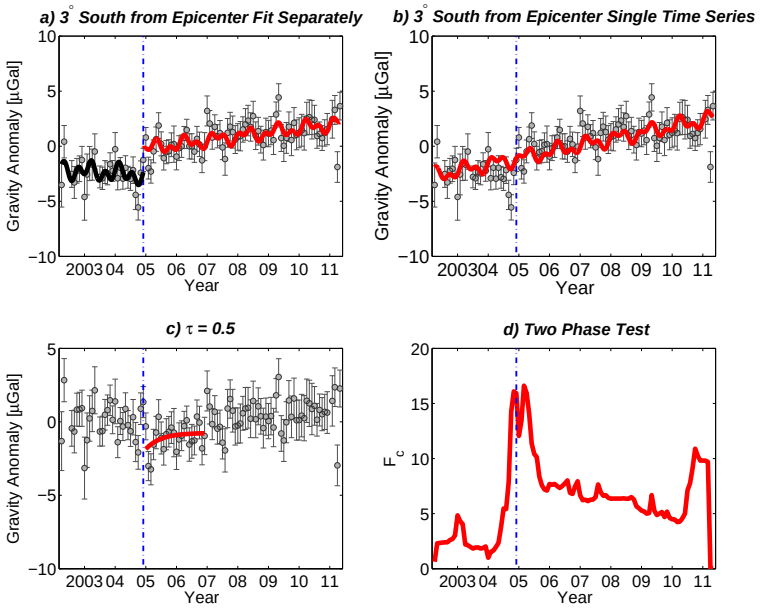

Figure D.1: *Fit and Changepoint Detection of Time Series in* 3° *South of Epicenter (*8°N, 96°E*) of Sumatra-Andaman Earthquake (GRACE Fan Filter* 350 km*)*

The second peak is the month when the Nias earthquake (Mar. 28, 2005) took place.

D.2 Maule Earthquake (Chile) 2010

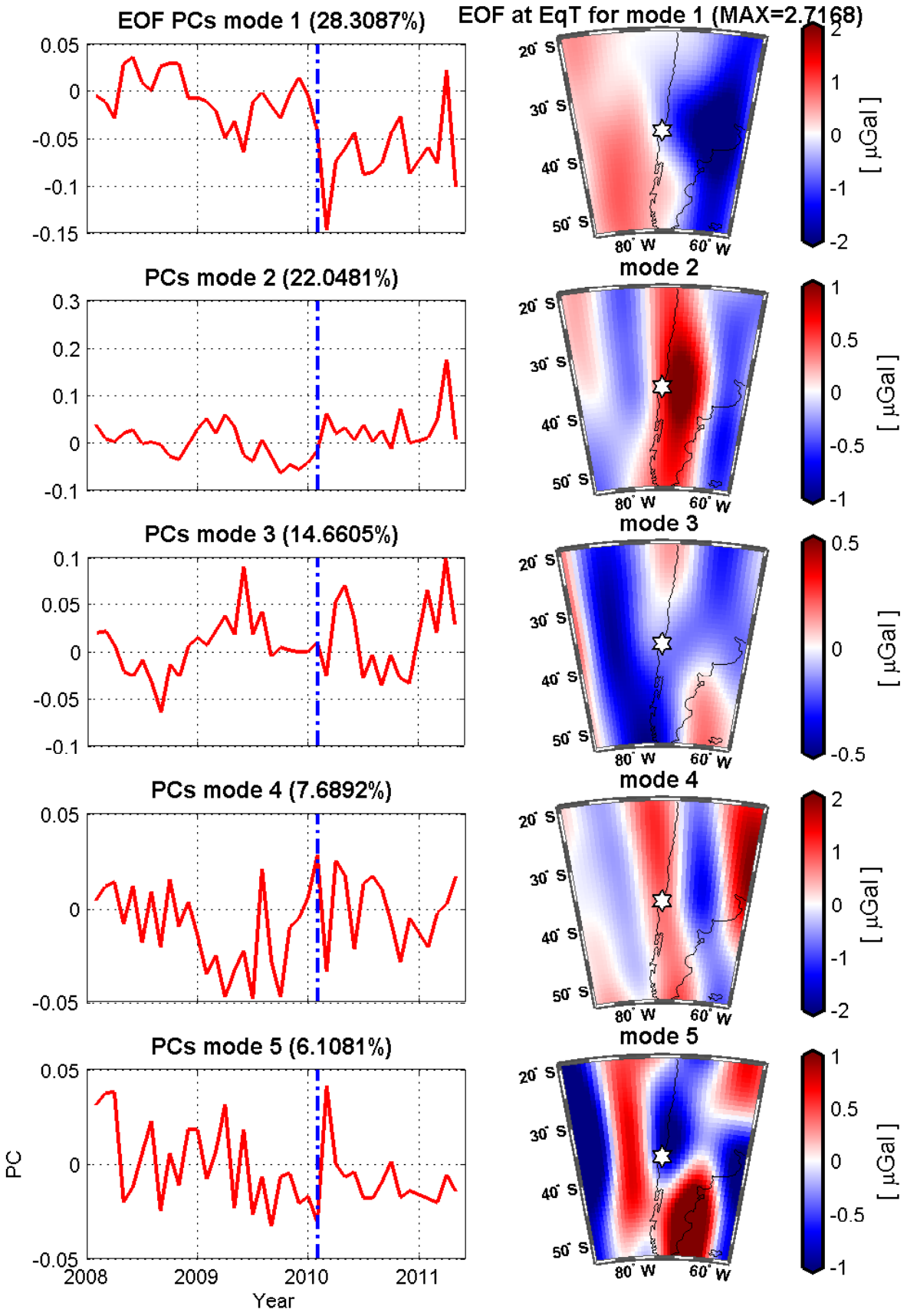

Figure D.2: *EOF Analysis of Maule Earthquake (Chile) 2010 (GRACE Gauss Filter* 350 m*)*

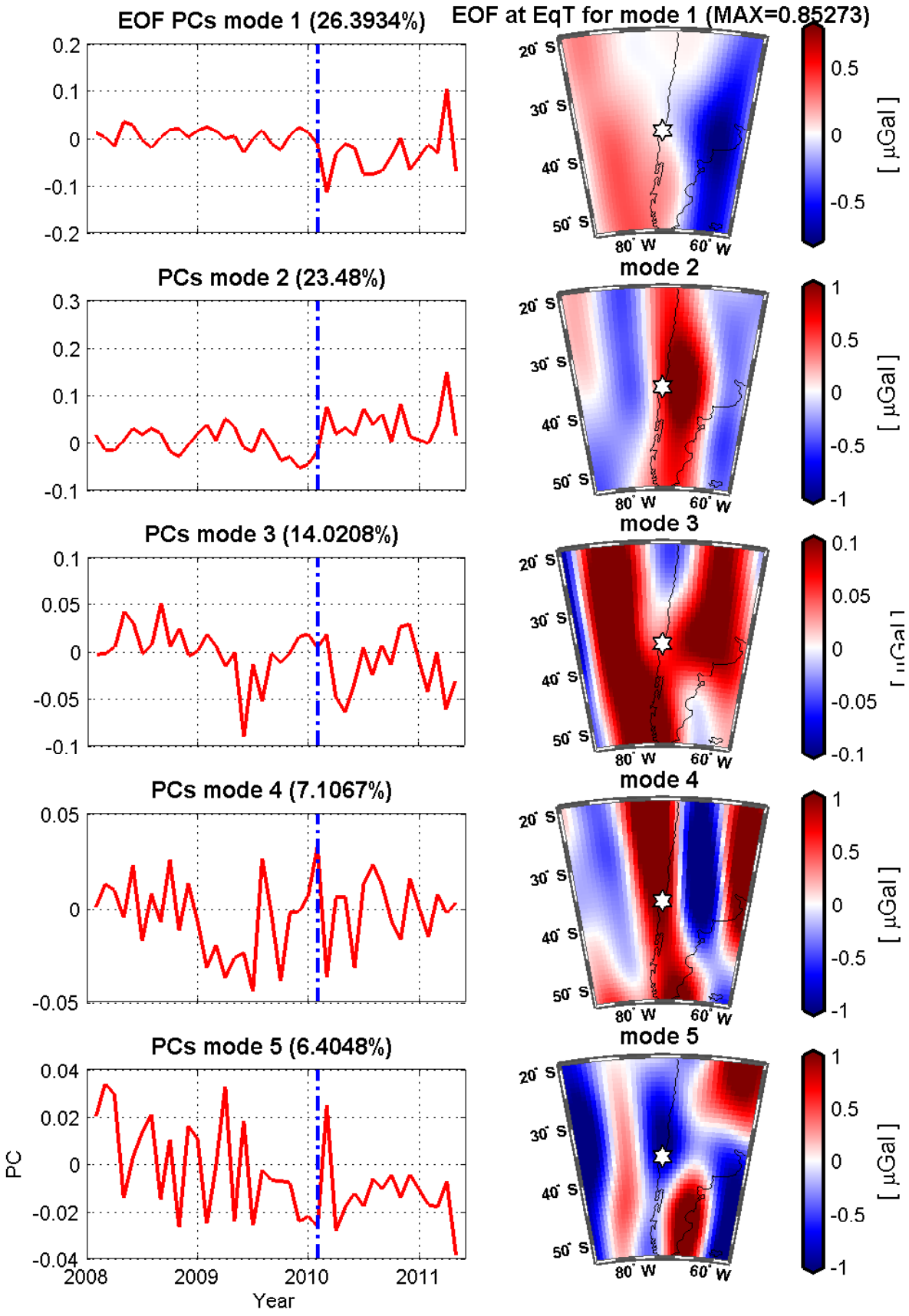

Figure D.3: *EOF Analysis of Maule Earthquake (Chile) 2010*
(GRACE-GLDAS Gauss Filter 350 m*)*

D.3 Tōhoku Earthquake (Japan) 2011

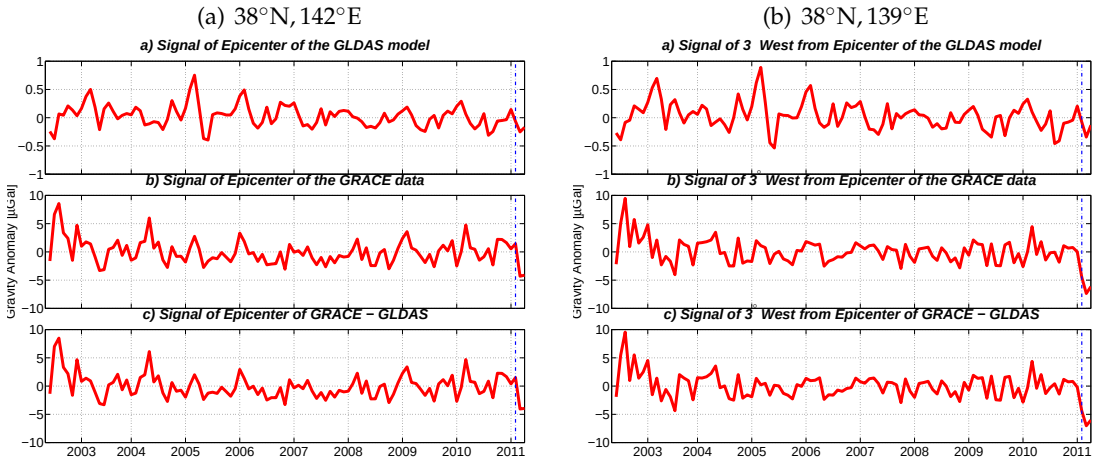

Figure D.4: *Time Series in Epicenter and* 3° *West of Epicenter* (38°N, 142°E) *Tōhoku Earthquake (Japan) 2011 (GRACE Gauss Filter* 350 m)

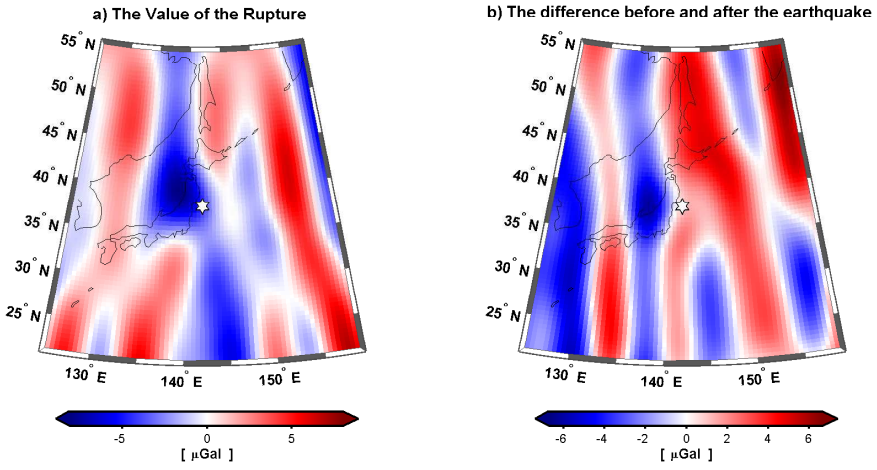

Figure D.5: *Rupture and Gravity Field Before and After Tōhoku Earthquake (Japan) 2011 (GRACE Gauss Filter* 350 m)

Appendix E

CD Contents

E.1 Matlab© Programs

Not all programs are listed in Fig. E.1, for more details of each program, please see the remark at the beginning of the m-files in CD.

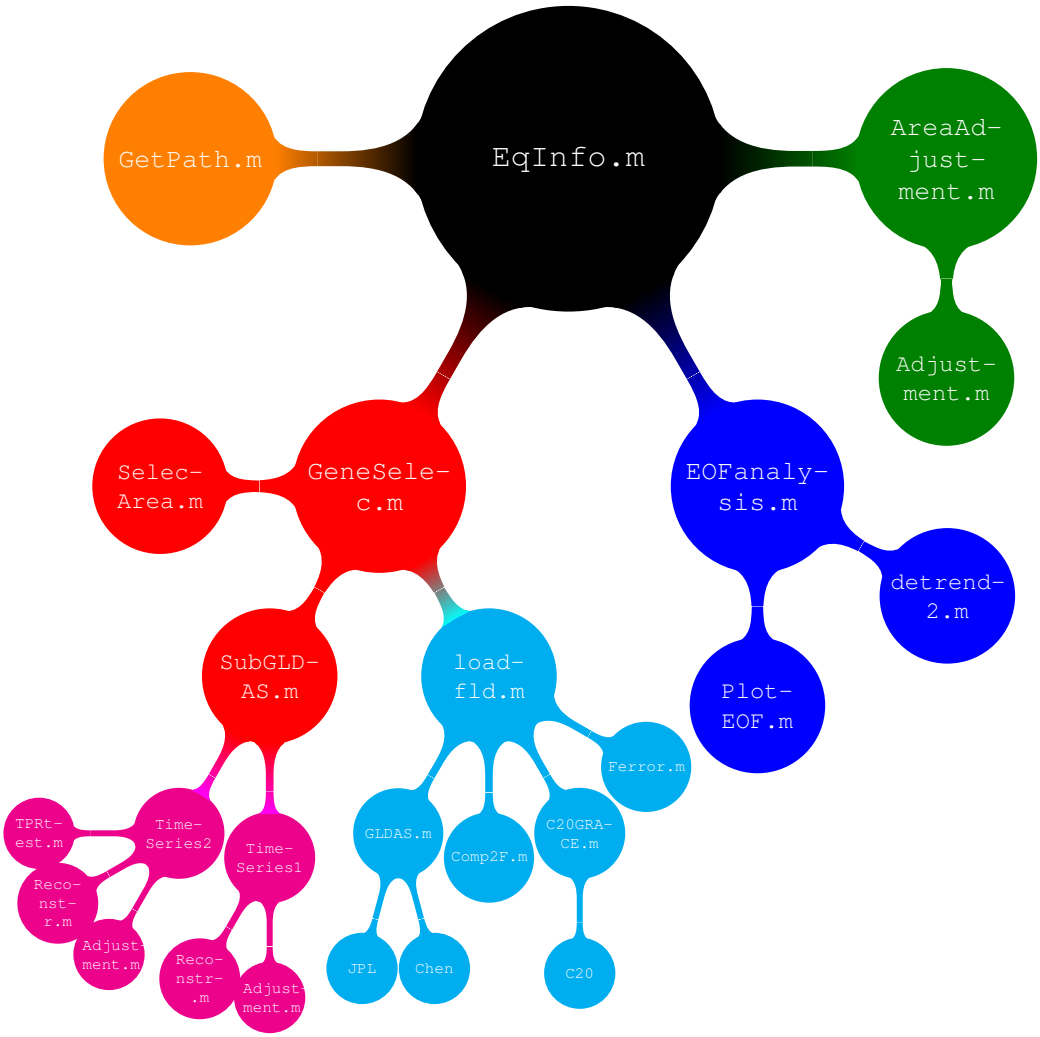

Figure E.1: *Matlab© Programs Topological Graph*

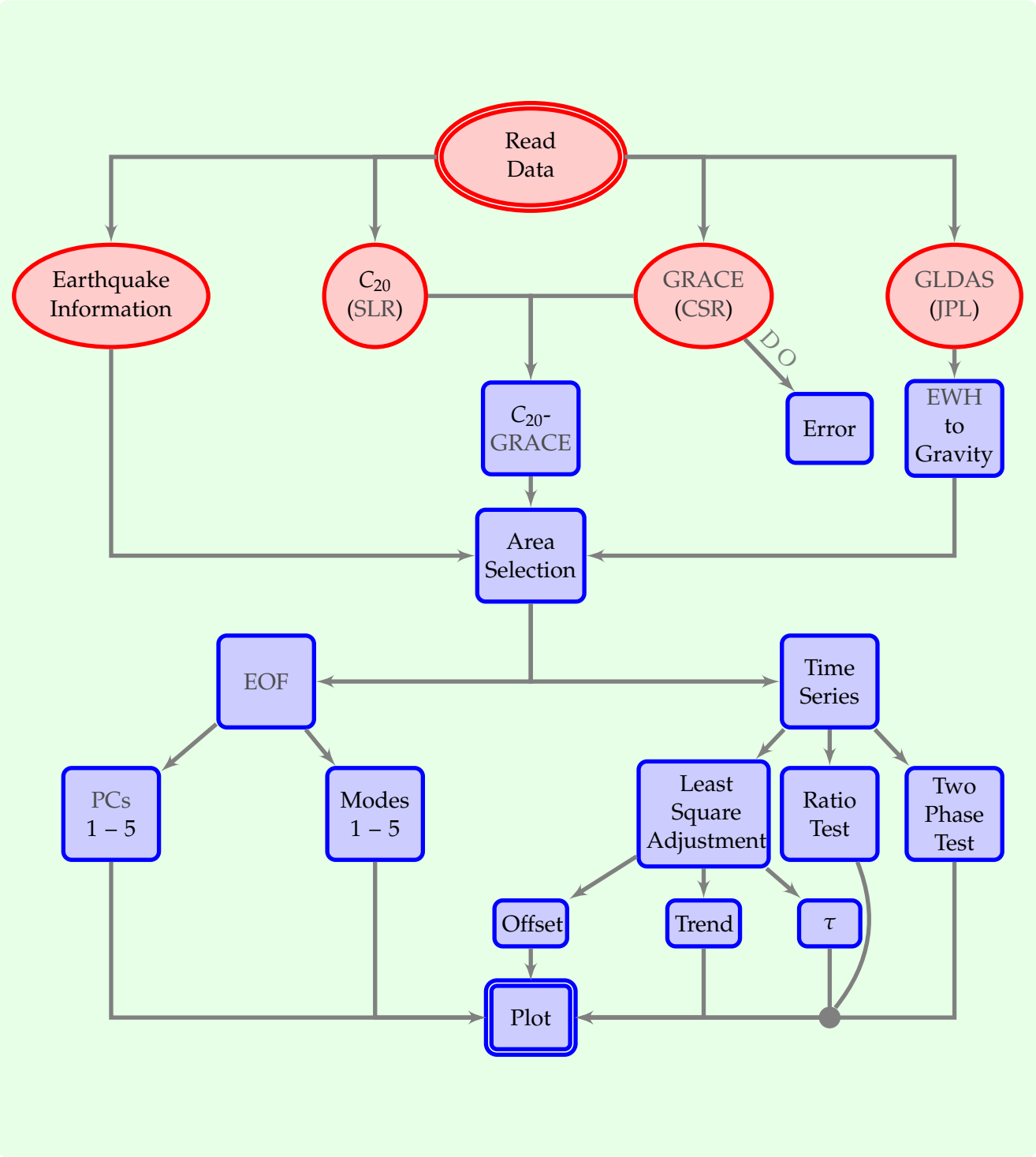

Figure E.2: *Simplified Program Flow Chart*

E.2 LaTeX Related Files

Except the default usepackages of the template from Mr. Matthias Roth, the listed usepackages are used.

Name	Short Description
`bm`	Bold math symbols
`caption`	Put the Caption in a proper position
`booktabs`	Provide nice footnote
`glossaries`	Generate the list of abbreviations and list of symbols
`hyperref`	For all the hyperlinks
`IEEEtrantools`	For large equation array
`makecell`	Use of tabular cells inside text
`mathdots`	Special math dots
`mcode`	Generate the Matlab© style text
`multirow`	Combine the columns in table
`subfigure`	For the subfigures
`textcomp`	For some special symbols
`tikz`	Some of the graphs generated by this package
`url`	For adding URLs
New Environment:	
`fancyquotes`	Nice quotes

Table E.1: *Usepackages Description*

Due to the `glossaries` usepackage, the installation of the Perl© is needed and the compile commands are:

```
pdflatex extras\titelseite
pdflatex arbeit
makeglossaries arbeit
bibtex arbeit
pdflatex arbeit
makeglossaries arbeit
pdflatex arbeit
pdflatex arbeit
```

Master Thesis 2011
GEOENGINE
Fakultät 6: Luft- und Raumfahrttechnik und Geodäsie
Stuttgart Universität
Geschwister-Scholl-Str. 24D
D-70174 Stuttgart

Thesis online through university library:
http://www.uni-stuttgart.de/gi/education/MSC/master_theses.en.html
http://www.geoengine.uni-stuttgart.de/forum/master/zhou_cao/index.html